

2018

# Vibrational sum-frequency generation spectroscopy as a molecular-level probe for aqueous, polymer, and solid interfaces

---

<https://hdl.handle.net/2144/33232>

*"Downloaded from OpenBU. Boston University's institutional repository."*

BOSTON UNIVERSITY  
GRADUATE SCHOOL OF ARTS AND SCIENCES

Dissertation

**VIBRATIONAL SUM-FREQUENCY GENERATION SPECTROSCOPY AS A  
MOLECULAR-LEVEL PROBE FOR AQUEOUS, POLYMER, AND SOLID  
INTERFACES**

by

**RICHARD ANDINO**

B.S., Florida International University, 2012  
M.A., Boston University, 2015

Submitted in partial fulfillment of the  
requirements for the degree of  
Doctor of Philosophy

2018



Approved by

First Reader

---

Lawrence D. Ziegler, Ph.D.  
Professor of Chemistry and Department Head

Second Reader

---

Shyamsunder Erramilli, Ph.D.  
Professor of Physics

## **DEDICATION**

To Sophia Faye Andino

## ACKNOWLEDGMENTS

I'd like to thank everyone that has helped make my experience at Boston University (and in Boston) truly unforgettable.

To my advisors Larry Ziegler and Shyam Erramilli: none of this would have been possible without you. I want to thank both of you for the effort you gave in assisting me throughout my studies. I felt lost when my original advisor had to leave the university, but the two of you were there to accept me into your research group and keep me motivated in my studies. It is refreshing to see others care about my research the way you two have, and I've learned so much working with both of you. The impact you have both made on my academic career here is invaluable and I appreciate everything you have done for me.

I would also like to thank my dissertation committee, Bjoern Reinhard, Xi Ling, and Masha Kamenetska. I met Bjoern in my first year of graduate school and got to know his lab very well, since I worked right next door. I would especially like to express my thanks to him for all of his generosity by allowing me access to his lab space and the use of all resources that were available to his students. I'd like to thank Xi and Masha for agreeing to be on my committee with short notice. I appreciate all of your feedback and I hope that learning about SFG can inspire future collaborations between our labs.

There are a couple other people that I would like to thank in the department as well. Kaitlin Valli has been such a tremendous help in the process of thesis writing and graduation. Thank you for your assistance. I've had the pleasure of teaching with Dr. Binyomin Abrams during most of time here at BU. It was a rewarding experience to

teach with someone that is as passionate as Dr. Abrams is, and I'd like to thank him for everything he has taught me in the process.

I'd like to thank the former Chen lab, Dr. Jian Liu and Christina Miller. I credit Jian with teaching me everything I know about SFG; he truly was a guru when it came to this. Jian was always patient when working with me and has helped shape me into the scientist that I am today. Outside of lab, Jian has introduced me to so many different types of food. I've eaten some of the best lunches I've ever had with him and will not forget that. Jian is one of the nicest and most caring individuals I've worked with, and I'm glad that our friendship remains to this day. Christina Miller has been my friend since the first day of graduate school. She is probably the most organized person I've ever met. Whenever she saw me unorganized she got stressed out, so she began to organize everything for me. I can't express how helpful that was. You're the one person that knows exactly how difficult it was to experience an advisor leave during graduate school, and I'm so happy that you were able to overcome that with me and find a career that you were passionate about. Even though you left BU years ago you still motivated me to finish, so thank you for all of your support. I hope that Owen and Sophia can become as great friends as us!

I also want to thank the Ziegler/Erramilli group: Matt Rotondaro, Greg Ng Pack, Parth Shah, Mina Nazari, Sean Foster, and Shane Devlin. Mina and Sean, I enjoyed teaching you two about my laser system and I have learned so much in that process. Shane joined the lab as an undergraduate student, and I had the pleasure of mentoring his studies. I honestly couldn't have asked for a better student to work with than Shane. He

was determined, self-motivated, smart, and a very fast learner. I couldn't have done this without your help. Thank you so much! Shane and I were forced to relocate our lab to the basement, where we got the opportunity to work closer to Matt, Greg, and Parth. At the time I was upset we needed to move the lab, but this turned out to be one of the best things that happened. Thank you all for helping in my preparation of this thesis and presentation. Also, I will never forget our nights of drinking while watching Shane beat Matt in literally every sport.

I've met some of my closest friends during graduate school. Sarah Lerch entered graduate school with me and worked in the lab next door to me. We ate lunch together pretty much every single day, and I enjoyed our talks about movies, TV shows, sports, and occasionally science. You became one of my best friends, and I'm so proud that I get to call you Dr. Lerch now. You've been a true inspiration to me and a huge motivation. I am sad that you left Boston, but I'm excited (and a little jealous) that you are working in Sweden now. I can't wait until we see each other again; I'm sure we will!

Chris Wong, my roommate and brother that I met at BU in my first days in Boston back in 2012. You've been one of my biggest supports throughout graduate school and life in general. I'm glad we were able to become such great friends, and I'm even more happy that baby Sophia is going to be lucky enough to have the dad joke master as an uncle! Jesse Guillet, it is so great to have a friend like you. I thought I was a big Fast and Furious fan until I met you. I can't wait until you move back to Boston so we can have a proper toast, "Salud mi familia!" Michelle and Andrew Evangelista, I want to thank you two for making me feel at home whenever I was with you guys. I felt that I

could always count on you two for anything. My best memories of Boston will always be the times I got to grill, play games, and hang out drinking with you guys, Chris and Jesse. Family is family.

I'd also like to thank Joey Campos. I didn't start hanging out with you until later on, but you quickly became a close friend. Thanks for being a great gym buddy and always being down to play basketball with me. To my roommate Kaleb Batten, thanks for teaching me to "git gud." Stefan Khuns, it was always a great time drinking with you and learning a bunch of random trivia. I hope we get to hang again when you're back from Sweden. Ivan Perez (a.k.a. Hurricane Ivan), thanks for some of the craziest nights at the local bars. You were an awesome roommate and I'm glad you still find the time to visit Boston to hang.

I would like to give a special thank you to Alie Zwart. You have been extremely understanding during the final push of this thesis. I'm so lucky to have a girlfriend as amazing as you, and I cherish all of the moments that we have had together and will have together. You are giving me the greatest gift in our daughter Sophia, and I love you both more than you will ever know! None of this would have been possible without your unconditional love and support.

Finally, I'd like to thank my family: all of my crazy uncles, aunts and cousins who have supported me. Thank you to my mom and dad for raising me and showing me the value of hard work and dedication. The values you've instilled in me have allowed me to come this far and I'm lucky to have parents that love me as much as you do. To my brothers, Steve Weintraub and Luis Jimenez, thank you for being my best friends

growing up and always pushing me to do better in school. Allison Andino, my sister and my best friend. I missed you as soon as I stepped foot on that plane from Florida to Boston. Thank you for being the best little sister that any big brother could ask for. I'm so proud of everything that you have accomplished and am amazed at how fast you grew up. I love you so much!

**VIBRATIONAL SUM-FREQUENCY GENERATION SPECTROSCOPY AS A  
MOLECULAR-LEVEL PROBE FOR AQUEOUS, POLYMER, AND SOLID  
INTERFACES**

**RICHARD ANDINO**

Boston University Graduate School of Arts and Sciences, 2018

Major Professor: Lawrence D. Ziegler, Professor of Chemistry and Departmental Head

**ABSTRACT**

Interfaces play a crucial role in a variety of physical, chemical, and biological phenomena. Due to the unique local environment, chemical and physical properties observed at the interface are different than in bulk media. This work exploits the highly selective surface layer sensitivity of the second-order phenomenon vibrational sum-frequency generation (SFG) spectroscopy to learn about interfacial chemistry and structure.

The surface  $pK_a$  of substituted benzoic acids and short-chain carboxylic acids are found by SFG spectroscopy and surface tension measurements. Measured surface  $pK_a$  values are greater than bulk solution values and are attributed to increased surface proton concentrations. Stronger van der Waals interactions are also found to increase  $pK_a$ . Anomalously large carbonyl stretching SFG intensities are found in a narrow pH range and provide evidence for a cooperative surface adsorption effect between *p*-methyl benzoic acid and its conjugate base.

In SFG studies of poly(*N*-isopropylacrylamide) (pNIPAM), Hofmeister anion effects are observed for the amide I band. Furthermore, SFG spectra reveal two distinct

pNIPAM amide I bands. One peak is centered at  $1625\text{ cm}^{-1}$ , consistent with bulk FTIR studies, and a second peak is observed at  $1665\text{ cm}^{-1}$ , blue shifted by  $40\text{ cm}^{-1}$ . The “bulk-like” peak ( $1625\text{ cm}^{-1}$ ) arises from fully solvated pNIPAM molecules located just below the interfacial layer and is enhanced in the presence of chaotropic anions. The blue shifted peak is attributed to decreased water solvation of pNIPAM molecules at the uppermost surface layer.

An odd-even effect is observed in the SFG spectra of *n*-alkanethiolate self-assembled monolayers (SAMs) on Au and Ag surfaces depending on surface roughness. Odd-even oscillations in SFG signal amplitudes and linewidths were observed for spectra derived from alkyl thiols with either odd or even numbers of carbons for SAMs on flat surfaces (RMS roughness =  $0.40\text{ nm}$ ), but not on rougher surfaces (RMS roughness =  $2.38\text{ nm}$ ). This effect is attributed to differences in terminal methyl group orientation for odd or even *n*.

This work demonstrates the capability of SFG spectroscopy to be an effective tool for determining surface number density, equilibrium constants, and molecular orientation for molecules at the interface.

## TABLE OF CONTENTS

DEDICATION .....	iv
ACKNOWLEDGMENTS .....	v
ABSTRACT .....	x
TABLE OF CONTENTS.....	xii
LIST OF TABLES.....	xv
LIST OF FIGURES .....	xvi
LIST OF ABBREVIATIONS.....	xviii
Chapter 1. Introduction.....	1
Chapter 2. Anomalous pH Dependent Enhancement of <i>p</i> -Methyl Benzoic Acid Sum- Frequency Intensities: Cooperative Surface Adsorption Effects .....	8
2.1 Introduction.....	8
2.1.1 <i>Theory Background</i> .....	12
2.2 Experimental.....	16
2.3 Results.....	18
2.3.1 <i>Titration of p-Methyl Benzoic Acid in Bulk Solution and via Surface Tension Measurements</i> .....	18
2.3.2 <i>Titration of p-Methyl Benzoic Acid via SFG</i> .....	21
2.3.3 <i>Orientation Analysis of p-Methyl Benzoic Acid and its Conjugate Base at the Air-Water Interface</i> .....	25

2.4 Discussion .....	32
2.4.1 Anomalous Surface Adsorption Indicates Cooperativity .....	32
2.4.2 Thermodynamic Analysis of Population and Non-ideal Activity in Acid-Base Mixtures .....	34
2.5 Conclusion .....	38
2.6 Supporting Information .....	40
2.6.1 Fitting of SFG spectra .....	40
2.6.2 Orientation determination of <i>p</i> -methyl benzoic acid and <i>p</i> -methyl benzoate ..	42
2.6.3 SFG spectra of CH <sub>3</sub> ( <i>ss</i> and <i>as</i> ) of <i>p</i> -methyl benzoic acid in <i>ssp</i> and <i>ppp</i> polarization configuration .....	44
2.6.4 Cooperative interactions and the Virial expansion .....	47
Chapter 3. Determination of Short-Chain Carboxylic Acid Surface pK <sub>a</sub> via Surface Tension and Vibrational Sum-Frequency Generation Spectroscopy .....	
3.1 Introduction .....	50
3.2 Experimental .....	53
3.3 Results and Discussion .....	55
3.3.1 Surface Tension Titration of Aliphatic Acids .....	55
3.3.2 Sum-Frequency Titration of Aliphatic Acids .....	59
3.4 Conclusion .....	65
3.5 Supporting Information .....	66
3.5.1 Surface Activity Model .....	66
3.5.2 Henderson-Hasselbalch Fitting Model for SFG Amplitudes .....	67

Chapter 4. Ion Effects on poly( <i>N</i> -isopropylacrylamide) at the Air-Water Interface Revealed by Vibrational Sum-Frequency Generation Spectroscopy.....	69
4.1 Introduction.....	69
4.2 Experimental.....	71
4.3 Results and Discussion .....	72
4.4 Conclusion .....	80
Chapter 5. Spectroscopic Evidence for the Origin of Odd-Even Effects in Self-Assemble Monolayers and Effects of Substrate Roughness.....	82
5.1 Introduction.....	82
5.2 Experimental.....	86
5.3 Results and Discussion .....	88
5.3.1 <i>SFG signal intensity and the odd–even effect</i> .....	92
5.3.2 <i>Asymmetry in the odd–even effect</i> .....	93
5.3.3 <i>Transition to a more ordered (crystalline) phase</i> .....	94
5.3.4 <i>Fe and Cu doped Au substrates</i> .....	97
5.3.5 <i>Ag substrates</i> .....	100
5.4 Conclusions.....	102
5.5 Supporting Information.....	105
5.5.1 <i>Fittings of SFG spectra</i> .....	105
5.5.2 <i>Calculations for the dependence of SFG intensity on the tilting angle</i> .....	109
REFERENCES .....	113
CURRICULUM VITAE.....	126

## LIST OF TABLES

<b>Table 2.1:Relative SFG peak intensity <i>ppp</i>/<i>ssp</i> ratio .....</b>	<b>29</b>
<b>Table S2.1:Gaussian calculated hyperpolarizability values.....</b>	<b>44</b>
<b>Table 3.1:Surface <math>pK_a</math> of aliphatic acids measured by surface tension and SFG .....</b>	<b>58</b>

## LIST OF FIGURES

Figure 1.1:Energy level diagram and SFG geometry .....	3
Figure 1.2:SFG optical table setup .....	7
Figure 2.1: <i>p</i> -methyl benzoic acid and <i>p</i> -methyl benzoate .....	11
Figure 2.2: <i>p</i> -methyl benzoic acid surface tension v. pH .....	19
Figure 2.3:Summary of SFG spectroscopic data for <i>p</i> MBA .....	24
Figure 2.4:Polarization dependent SFG spectra for <i>p</i> MBA at 1610cm <sup>-1</sup> .....	27
Figure 2.5:Orientation of <i>p</i> -methyl benzoic acid and <i>p</i> -methyl benzoate .....	30
Figure 2.6:Calculated sum-frequency susceptibility plots and <i>ppp</i> / <i>ssp</i> ratio plot.....	31
Figure S2.1:Water bending contribution fits for SFG carbonyl stretching mode ....	41
Figure S2.2:SFG spectra of CH <sub>3</sub> ( <i>as</i> and <i>ss</i> ) of <i>p</i> -methyl benzoic acid .....	45
Figure S2.3:SFG spectra of COO <sup>-</sup> ( <i>ss</i> ) of <i>p</i> -methyl benzoate in <i>ssp</i> and <i>ppp</i> .....	46
Figure S2.4:Bulk titration of 1 mM <i>p</i> MBA with 5 mM NaOH.....	47
Figure 3.1:Surface tension of aliphatic acids as a function of pH .....	55
Figure 3.2:Δγ plots of aliphatic acids as a function of pH .....	58
Figure 3.3:SFG spectra of aliphatic acids in C=O and COO <sup>-</sup> ( <i>ss</i> ) region.....	60
Figure 3.4:Plot of normalized peak amplitude for aliphatic acids .....	63
Figure 3.5:Summarized values of literature surface pK <sub>a</sub> values .....	64
Figure 4.1:ATR-FTIR spectrum of 0.6 mg/mL pNIPAM in D <sub>2</sub> O .....	73
Figure 4.2:SFG spectra of pNIPAM amide I band in H <sub>2</sub> O and D <sub>2</sub> O .....	74
Figure 4.3:SFG spectra of pNIPAM amide I in presence of Hofmeister anions.....	75
Figure 4.4:Depiction of pNIPAM structure at the air-water interface.....	77

<b>Figure 4.5:pNIPAM SFG amide I peak amplitude vs. Hofmeister anion.....</b>	<b>78</b>
<b>Figure 5.1:Manifestion of odd-even effect in self-assembled monolayers .....</b>	<b>83</b>
<b>Figure 5.2:Characterization of AuTS and AuAD substrates by AFM .....</b>	<b>89</b>
<b>Figure 5.3:Summary of SFG data for SAMs on AuTS and AuAD substrates .....</b>	<b>91</b>
<b>Figure 5.4:Summary of SFG data for SAMs on AuFe, AuTS, and AuCu surfaces..</b>	<b>98</b>
<b>Figure 5.5:Odd-even oscillation in CH<sub>3</sub> asymmetric-symmetric stretching ratio.....</b>	<b>99</b>
<b>Figure 5.6:Depiction of SAMs on Ag substrates .....</b>	<b>100</b>
<b>Figure 5.7:SFG spectra of CH stretching region for SAMs on AgTS and AgCu ...</b>	<b>101</b>
<b>Figure S5.1:Fitting curves for SFG spectra of C<sub>15</sub> and C<sub>16</sub> on AuTS.....</b>	<b>107</b>
<b>Figure S5.2:Fitting curve for SFG spectra of C<sub>15</sub> on AuAD .....</b>	<b>108</b>
<b>Figure S5.3:AFM image showing grains and grain boundaries of AuTS surface ..</b>	<b>109</b>
<b>Figure S5.4:Dependence of CH<sub>3</sub> (<i>as</i> and <i>ss</i>) SFG intensities on tilt angle .....</b>	<b>112</b>

## LIST OF ABBREVIATIONS

2D.....	Two-dimensional
3D.....	Three-dimensional
A <sup>-</sup> .....	Deprotonated ionized form
AFM.....	Atomic force microscopy
Ag.....	Silver
Ag <sup>Cu</sup> .....	Copper-doped silver substrate
Ag <sup>TS</sup> .....	Template stripped silver substrate
<i>as</i> .....	Asymmetric stretching
ATR.....	Attenuated total reflection
Au.....	Gold
Au <sup>AD</sup> .....	As deposited gold substrate
Au <sup>Cu</sup> .....	Copper-doped gold substrate
Au <sup>Fe</sup> .....	Iron-doped gold substrate
Au <sup>TS</sup> .....	Template stripped gold substrate
C=O.....	Carbonyl
CCD.....	Charge-coupled device
C <sub>n</sub> .....	<i>n</i> -numbered carbon chain
COO <sup>-</sup> .....	Carboxylate
DFT.....	Density functional theory
Et al.....	Et alia
Eq.....	Equation

Fig.	.....	Figure
FWHM	.....	Full-width at half maximum
FTIR	.....	Fourier-transform infrared
GaAs	.....	Gallium arsenide
HA	.....	Protonated acid
HCl	.....	Hydrochloric acid
HH	.....	Henderson Hasselbalch
IR	.....	Infrared
IRRAS	.....	Infrared reflection-absorption spectroscopy
LB	.....	Langmuir-Blodgett
LCST	.....	Lower critical solution temperature
Na <sup>+</sup>	.....	Sodium ion
NaCl	.....	Sodium chloride
NaOH	.....	Sodium hydroxide
Nd:YLF	.....	Neodymium-doped yttrium lithium fluoride
NEXAFS	.....	Near edge X-ray absorption fine structure
OA	.....	Optical adhesive
<i>p</i> MBA	.....	<i>p</i> -methyl benzoic acid
<i>p</i> MBA <sup>-</sup>	.....	<i>p</i> -methyl benzoate
pNIPAM	.....	poly( <i>N</i> -isopropylacrylamide)
Pt	.....	Platinum
RMS	.....	Root mean square

SAM ..... Self-assemble monolayer  
SAM<sup>E</sup> ..... Even-numbered self-assemble monolayer  
SAM<sup>O</sup> ..... Odd-numbered self-assemble monolayer  
SF ..... Sum-frequency  
SFG ..... Sum-frequency generation  
SFGIM ..... Sum-frequency generation imaging microscopy  
*ss* ..... Symmetric stretching  
STM ..... Scanning tunneling microscopy  
Ti:sapphire ..... Titanium-sapphire  
UPS ..... Ultra-violet photoelectron spectroscopy  
UV ..... Ultra-violet  
*vis* ..... Visible

## CHAPTER 1. Introduction

Interfaces are ubiquitous in nature. They are present in biological systems,<sup>1-3</sup> such as the aqueous interface in the alveoli of lungs<sup>4</sup> that allow for the rapid absorption of small molecules by diffusion through the plasma membrane.<sup>5-6</sup> Environmental interfaces are responsible for the growth of atmospheric aerosols,<sup>7-8</sup> which contribute to global climate forcing through the backscatter of short-wavelength (~370-430 nm) solar radiation.<sup>9-10</sup> Therefore, understanding the composition, reactivity and structure of aqueous interfaces is crucial to environmental atmospheric chemistry and global climate modeling. Interfacial studies of aqueous solutions containing simple inorganic ions,<sup>11-14</sup> solutes,<sup>15-18</sup> and lipids,<sup>19-23</sup> have been of particular interest, since they can influence aerosol structure, growth and reactivity. Due to the unique chemical environment of the interface, chemical and physical properties such as the surface density, equilibrium constants, molecular orientation, hydrogen bonding, and other intermolecular interaction forces are usually very different from those in the bulk phase.<sup>24</sup>

Probing aqueous interfaces is difficult because the experimental measurement is ideally surface specific only when applied to liquid the interface. Techniques such as scanning tunneling microscopy (STM) and atomic force microscopy (AFM) are very surface selective and can be applied to the study of liquid thin films on solid substrates, but suffer when there is molecular movement at the interface.<sup>25-27</sup> X-ray spectroscopy and neutron reflectivity can be very useful tools for learning about some interfaces,<sup>28-32</sup> but probe a surface layer  $\geq 1$  nm in depth and are not easily applied to buried liquid interfaces. Attenuated total reflection (ATR) infrared spectroscopy can be applicable to

buried interfaces. However the probe depth is  $\geq 100$  nm and is therefore not very surface specific.<sup>33</sup> The advancement of vibrational sum-frequency generation (SFG) spectroscopy, since the late 1980's,<sup>34</sup> has made surface selective probing of liquid interfaces possible, and has become a preferred technique to do so.<sup>11, 33, 35-36</sup> The principles governing SFG spectroscopy, along with the experimental layout of our system, is outlined in this introductory chapter.

Vibrational sum-frequency generation spectroscopy is a second order, non-linear optical phenomenon that requires two photons to interact simultaneously with a molecule or material interface. When a visible laser beam pulse and a tunable IR beam pulse are spatially and temporally overlapped at the interface of a sample a sum-frequency signal is generated. The generated signal pulse will have a frequency equal to the sum of the frequencies of the two incident beams (**Fig. 1.1**). Since second order optical processes are symmetrically forbidden in media possessing inversion symmetry, a bulk solution does not generate an SFG signal field. Thus, the SFG signal contains contributions only from media lacking centrosymmetry, which is naturally broken at interfaces, making SFG a surface selective technique that is perfectly suited for studying molecular level details within the first  $\sim$ nm or less of the interface.<sup>37-38</sup> SFG spectroscopy provides the vibrational spectrum of interfacial molecules when the IR pulse frequency is resonant with a molecular vibration transition resulting in a large increase in the SFG signal (**Figure 1.1a**). This allows the study of interfacial chemistry with molecular level detail. As illustrated in **Fig. 1.1a**, only modes that are both Raman and IR active will appear in SFG spectra.

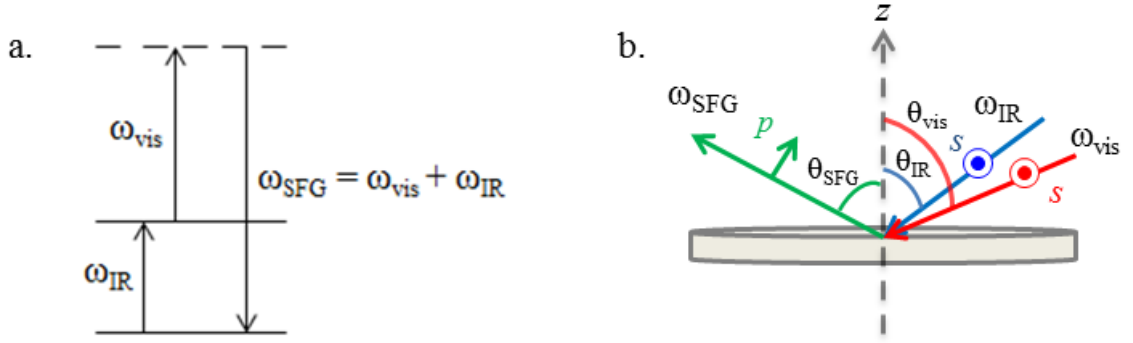


**Figure 1.1:** (a) Energy level diagram of the vibrationally resonant sum-frequency process. The solid lines indicate real states, while the dashed line indicates a virtual excited state. (b) Reflection geometry of the SFG process in *ssp* polarization configuration. *s* polarization is depicted as a circle, perpendicular to the *xz* plane, while *p* polarization is depicted as an arrow in the *xz* plane.

The intensity of the sum-frequency generation (SFG) homodyne signal,  $I_{\text{SFG}}$ , polarized along the  $i^{\text{th}}$  direction is proportional to the square of the effective second order susceptibility,  $\chi_{\text{eff}}^{(2)}$ , and the two incident laser intensities as given by<sup>37</sup>

$$I_{\text{SFG}i} \propto \left| \chi_{\text{eff}}^{(2)} \cdot E_j^{800} \cdot E_k^{\text{IR}} \right|^2 \propto \left| \chi_{\text{eff}}^{(2)} \right|^2 I_{800} I_{\text{IR}} \quad (1.1)$$

where  $I_{800}$  and  $I_{\text{IR}}$  are the intensities of the incident 800 nm and IR beams polarized along the  $j$  and  $k$  lab fixed frame directions, respectively. The effective second order susceptibility,  $\chi_{\text{eff}}^{(2)}$ , is a linear combination of the macroscopic second order susceptibility tensors,  $\chi_{ijk}^{(2)}$ , where  $i, j, k$  are laboratory coordinates ( $x, y, z$ ). We define the  $xy$  plane in the laboratory coordinates as the plane of the interface, with the  $z$  axis as the surface normal. All beams propagate in the  $xz$  plane, and  $p$  denotes polarization of the optical field in the  $xz$  plane, whereas  $s$  denotes polarization perpendicular to the  $xz$  plane. For a rotationally isotropic achiral interface with  $C_{\infty V}$  symmetry, only seven of the

possible 27 macroscopic second order susceptibility tensors,  $\chi_{ijk}^{(2)}$ , are non-zero:<sup>38-39</sup>

$$\chi_{xxz}^{(2)} = \chi_{yyz}^{(2)}, \chi_{xzx}^{(2)} = \chi_{zyy}^{(2)}, \chi_{zxx}^{(2)} = \chi_{zzy}^{(2)}, \text{ and } \chi_{zzz}^{(2)}.$$

The non-zero macroscopic second order susceptibility elements can be used to express the effective second order susceptibility as follows:<sup>37</sup>

$$\begin{aligned} \chi_{eff}^{(2)} = & \sin \Omega_{\text{SFG}} \sin \Omega_{\text{vis}} \cos \Omega_{\text{IR}} L_{yy}(\omega_{\text{SFG}}) L_{yy}(\omega_{\text{vis}}) L_{zz}(\omega_{\text{IR}}) \sin \theta_{\text{IR}} \chi_{yyz}^{(2)} \\ & + \sin \Omega_{\text{SFG}} \cos \Omega_{\text{vis}} \sin \Omega_{\text{IR}} L_{yy}(\omega_{\text{SFG}}) L_{zz}(\omega_{\text{vis}}) L_{yy}(\omega_{\text{IR}}) \sin \theta_{\text{vis}} \chi_{zyy}^{(2)} \\ & + \cos \Omega_{\text{SFG}} \sin \Omega_{\text{vis}} \sin \Omega_{\text{IR}} L_{zz}(\omega_{\text{SFG}}) L_{yy}(\omega_{\text{vis}}) L_{yy}(\omega_{\text{IR}}) \sin \theta_{\text{SFG}} \chi_{zyy}^{(2)} \\ & - \cos \Omega_{\text{SFG}} \cos \Omega_{\text{vis}} \cos \Omega_{\text{IR}} L_{xx}(\omega_{\text{SFG}}) L_{xx}(\omega_{\text{vis}}) L_{zz}(\omega_{\text{IR}}) \cos \theta_{\text{SFG}} \cos \theta_{\text{vis}} \sin \theta_{\text{IR}} \chi_{xxz}^{(2)} \\ & - \cos \Omega_{\text{SFG}} \cos \Omega_{\text{vis}} \cos \Omega_{\text{IR}} L_{xx}(\omega_{\text{SFG}}) L_{zz}(\omega_{\text{vis}}) L_{xx}(\omega_{\text{IR}}) \cos \theta_{\text{SFG}} \sin \theta_{\text{vis}} \cos \theta_{\text{IR}} \chi_{xxz}^{(2)} \\ & + \cos \Omega_{\text{SFG}} \cos \Omega_{\text{vis}} \cos \Omega_{\text{IR}} L_{zz}(\omega_{\text{SFG}}) L_{xx}(\omega_{\text{vis}}) L_{xx}(\omega_{\text{IR}}) \sin \theta_{\text{SFG}} \cos \theta_{\text{vis}} \cos \theta_{\text{IR}} \chi_{zxx}^{(2)} \\ & + \cos \Omega_{\text{SFG}} \cos \Omega_{\text{vis}} \cos \Omega_{\text{IR}} L_{zz}(\omega_{\text{SFG}}) L_{zz}(\omega_{\text{vis}}) L_{zz}(\omega_{\text{IR}}) \sin \theta_{\text{SFG}} \sin \theta_{\text{vis}} \sin \theta_{\text{IR}} \chi_{zzz}^{(2)}. \end{aligned} \quad (1.2)$$

$\Omega_{\text{SFG}}$ ,  $\Omega_{\text{vis}}$ , and  $\Omega_{\text{IR}}$  are the polarization angles of the SFG, visible, and IR beams, respectively, relative to the  $xz$  plane. The angles  $\theta_{\text{SFG}}$ ,  $\theta_{\text{vis}}$ , and  $\theta_{\text{IR}}$  are the reflected angle of the SFG signal and the incident angles of the visible and IR beams relative to the surface normal. The reflection geometry is depicted in Figure 1.1b.  $L_{ii}(\omega)$  is the diagonal element of the Fresnel factor at frequency  $\omega$  (where  $\omega = \omega_{\text{SFG}}$ ,  $\omega_{\text{vis}}$ , or  $\omega_{\text{IR}}$ ) defined by<sup>37-38</sup>

$$\begin{aligned} L_{xx}(\omega) &= \frac{2n_1(\omega) \cos \gamma}{n_1(\omega) \cos \gamma + n_2(\omega) \cos \theta} \\ L_{yy}(\omega) &= \frac{2n_1(\omega) \cos \theta}{n_1(\omega) \cos \theta + n_2(\omega) \cos \gamma} \\ L_{zz}(\omega) &= \frac{2n_1(\omega) \cos \theta}{n_1(\omega) \cos \gamma + n_2(\omega) \cos \theta} \left( \frac{n_1(\omega)}{n'(\omega)} \right)^2 \end{aligned} \quad (1.3)$$

where  $n_1(\omega)$ ,  $n_2(\omega)$ , and  $n'(\omega)$  are the refractive index of air, water, and the interface (the average of  $n_1$  and  $n_2$ ), respectively, at frequency  $\omega$ , and  $\gamma$  is the refracted angle for each beam. Therefore, the effective second order susceptibility,  $\chi_{eff}^{(2)}$ , is dependent on the experimental configuration geometry and incident laser and signal polarization directions. In this work, two experimental polarization combinations were used: *ssp* (*s*-polarized SFG, *s*-polarized visible, and *p*-polarized IR, respectively) and *ppp* (*p*-polarized SFG, visible, and IR), reducing the expression for  $\chi_{eff}^{(2)}$  to:

$$\chi_{eff,ssp}^{(2)} = L_{yy}(\omega_{SFG})L_{yy}(\omega_{vis})L_{zz}(\omega_{IR}) \sin \theta_{IR} \chi_{yyz}^{(2)} \quad (1.4)$$

$$\begin{aligned} \chi_{ppp}^{(2),eff} = & -L_{xx}(\omega_{SFG})L_{xx}(\omega_{vis})L_{zz}(\omega_{IR}) \cos \theta_{SFG} \cos \theta_{vis} \sin \theta_{IR} \chi_{xxz}^{(2)} \\ & -L_{xx}(\omega_{SFG})L_{zz}(\omega_{vis})L_{xx}(\omega_{IR}) \cos \theta_{SFG} \sin \theta_{vis} \cos \theta_{IR} \chi_{xxz}^{(2)} \\ & +L_{zz}(\omega_{SFG})L_{xx}(\omega_{vis})L_{xx}(\omega_{IR}) \sin \theta_{SFG} \cos \theta_{vis} \cos \theta_{IR} \chi_{zzx}^{(2)} \\ & +L_{zz}(\omega_{SFG})L_{zz}(\omega_{vis})L_{zz}(\omega_{IR}) \sin \theta_{SFG} \sin \theta_{vis} \sin \theta_{IR} \chi_{zzz}^{(2)}. \end{aligned} \quad (1.5)$$

The macroscopic second order susceptibility,  $\chi_{ijk}^{(2)}$ , is dependent on the surface number density,  $\rho_s = N_s/A_s$ , where  $N_s$  is the total number of molecules on the surface of area  $A_s$ , and the molecular orientation of the vibrator at the interface.<sup>37-38</sup>

$$\chi_{ijk}^{(2)} = \rho_s \sum_{i'j'k'} \langle R_{ii'}R_{jj'}R_{kk'} \rangle \beta_{i'j'k'}^{(2)} \quad (1.6)$$

$\beta_{i'j'k'}^{(2)}$  represents the microscopic hyperpolarizability elements in the molecular fixed ( $i'j'k'$ ) frame, and  $R_{\lambda\lambda'}$  are the elements of the Euler rotational transformation matrix to the space fixed ( $ijk$ ) frame.<sup>40</sup> The microscopic polarizability consists of a complex non-resonant term,  $\beta_{NR}^{(2)}$ , and a sum of vibrational resonant terms,  $A_q$ , which can be expressed as a Lorentzian contribution as shown below,<sup>37, 41</sup>

$$\beta^{(2)} = \beta_{NR}^{(2)} + \sum_q \frac{A_q}{\omega_{IR} - \omega_q + i\Gamma_q} \quad (1.7)$$

where  $\omega_{IR}$  is the frequency of the incident IR beam.  $A_q$ ,  $\omega_q$ , and  $\Gamma_q$  are the amplitude, the frequency and the line width of  $q^{\text{th}}$  the vibrational transition. As noted above, the amplitude is nonzero only if both the Raman and IR transitions are allowed (see **Fig. 1.1a**), therefore the resonant term dominates the intensity of the SFG signal when  $\omega_{IR}$  is resonant with a vibrational mode where this selection rule is obeyed. The observed SFG spectra are fit to Eq. 1.7 in order to quantitatively determine the fitting parameters,  $A_q$ ,  $\omega_q$ , and  $\Gamma_q$ .

The optical setup of our spectrometer is outlined in Figure 1.2. The primary light source of the system is a 4 W regenerative Ti:sapphire amplifier (Libra-F-1k-HE-110, Coherent, CA), pumped by a 527 nm Nd:YLF laser (Evolution-30, Coherent, CA), which produces 100 fs pulses centered at 800 nm with a 1 kHz repetition rate. Half of the regenerative amplifier output is converted into a broad bandwidth ( $\sim 100$  fs,  $\sim 185$   $\text{cm}^{-1}$ ) IR beam, which is tunable from 500 to 4000  $\text{cm}^{-1}$ , using an optical parametric amplifier (TOPAS-C, Light Conversion, Lithuania) and a non-collinear difference frequency generator (NDFG, Light Conversion, Lithuania). The other half of the 800 nm regenerative amplifier output is used to produce a narrow bandwidth (1.5 ps,  $\sim 10$   $\text{cm}^{-1}$ ) beam by passing this pulse through a simple lens and slit combination pulse shaper (**Fig. 1.2**). By adjusting an optical delay line, the narrow bandwidth 800 nm beam is temporally and spatially overlapped with the broad bandwidth IR beam on the sample surface in a region of  $\sim 100 \mu\text{m}^2$ . The incident angles are  $68^\circ$  ( $\theta_{\text{vis}}$ ) and  $55^\circ$  ( $\theta_{\text{IR}}$ ) from the surface normal for the two beams, respectively. The generated SFG signal in the reflected

direction is spectrally dispersed using a 500 mm monochromator (Acton SP2500, Princeton Instruments, NJ) and detected by a liquid-nitrogen-cooled CCD (PyLoN:1340x400B, Princeton Instruments, NJ). The reflection angle ( $\theta_{\text{SFG}}$ ) of the generated SFG signal varies with the frequency of the IR beam and is determined by Eq. 1.8, which is derived from the conservation of momentum in the  $x$  direction.<sup>42</sup> The experimental reflection geometry is depicted in Figure 1.1.

$$\omega_{\text{SFG}} \sin \theta_{\text{SFG}} = \omega_{\text{vis}} \sin \theta_{\text{vis}} + \omega_{\text{IR}} \sin \theta_{\text{IR}}. \quad (1.8)$$

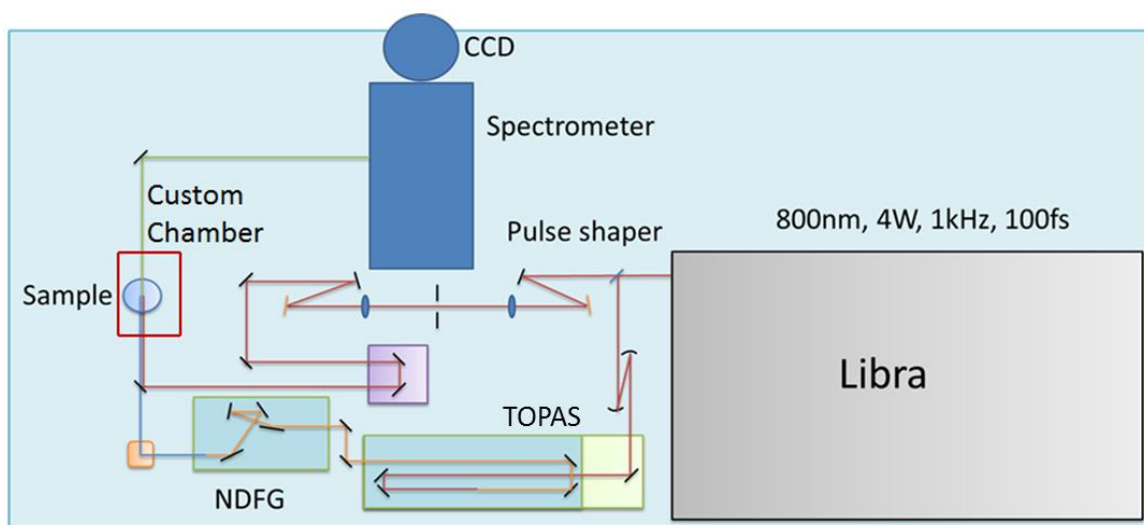


**Figure 1.2: Schematic of optical table for vibrational sum-frequency generation spectroscopy.**

All SFG spectra recorded with a broad-band vibrational sum-frequency spectrometer described above<sup>43-44</sup> are normalized relative to the non-vibrational SFG response from a GaAs crystal. The bandwidths (FWHM) of the overlapping visible (800 nm) and IR beams were  $\sim 10 \text{ cm}^{-1}$  and  $\sim 185 \text{ cm}^{-1}$ , respectively. Relative incident laser polarizations were determined by half-wave/polarizer elements, and the selected signal polarization component was defined by a polarizer in the signal beam path.

## CHAPTER 2. Anomalous pH Dependent Enhancement of *p*-Methyl Benzoic Acid

### Sum-Frequency Intensities: Cooperative Surface Adsorption Effects

#### 2.1 Introduction

Aqueous surfaces play an important role in a variety of physical, chemical, and biological processes.<sup>11</sup> Due to the low dielectric permittivity, anisotropic solvation, and reduced dimensionality of interfacial species, molecules behave differently at the gas-liquid interface than in bulk solution.<sup>45</sup> The fundamental differences between materials properties in 2D and 3D have long been a subject of intense study, with qualitatively different behavior observed in low-dimensional systems. At the molecular level, the differences in the local solvation environment can have a profound effect on the acidity of molecules, their cooperative interactions, and the appearance of novel phases. For example, the ranking of increasing acidities of some simple alcohols in bulk aqueous solution as given by  $pK_a$  is: MeOH (15.21) > EtOH (15.85) > *i*-PrOH (16.48) > *t*-BuOH (16.54).<sup>46</sup> However, in the gas phase, this relative ranking of acidity strengths, as determined by mass spectrometry, is reversed.<sup>47</sup> Similarly, a given acid may exhibit different properties at a 2D interface than in bulk solution. The change in  $pK_a$  values reported for acids at air-water interfaces are one example of the special solvation effects that may arise in reduced liquid dimensional environments. Understanding local solvation effects at the surface and their impact on  $pK_a$ 's are especially important, in part due to the key role that acidic and basic aqueous solutions play in environmental and atmospheric chemistry.<sup>7, 48-51</sup> Additionally, surface  $pK_a$  impacts interfacial biochemical phenomena,

such as protein folding and unfolding arising from the pH dependence of amino acid protonation/deprotonation.<sup>52</sup>

A variety of techniques have been previously used to study acids at interfaces.<sup>53-60</sup> Many studies of the air-water interface have focused on the water structure in the presence of small inorganic acids.<sup>13-14, 61-64</sup> For example, the addition of nitric acid to aqueous solutions perturbs the first layer of water molecules by forming an electric double layer favoring more polarizable anions to be located near the surface than cations. This results in a realignment of the surface water molecules relative to the surface normal, as they respond to the excess negative charge at the surface by increasing the alignment of water molecules at the surface.<sup>61</sup> Sum-frequency generation (SFG) spectroscopy is an ideal technique to study acids at surfaces.<sup>17-18, 63, 65-66</sup> Since this second order, non-linear optical phenomenon is forbidden in media with inversion symmetry, SFG spectroscopy is highly surface specific and selectively probes molecules at the air-water interface. The quadratic number dependence of homodyne detected SFG signals provides enhanced sensitivity to sample number density changes at the interface as a function of system variables. Of particular relevance to the spectra reported here, SFG studies of aqueous interfaces have expanded from probes of the water structure in the presence of small inorganic acids to the effects of cations and pH on the ionization state of long-chain fatty acids<sup>65</sup> and in characterizing the interfacial population and organization of surfactants.<sup>67</sup> The properties of long-chain fatty acids at interfaces are of particular interest because of the role they play in surface adsorption of lung surfactant in the alveoli and their potential mechanistic impact for controlling therapeutic effects in

lungs and related tissues.<sup>4, 68</sup> Previous SFG studies have found that long-chain acids exhibit an increase in  $pK_a$  at the surface relative to bulk solution  $pK_a$  values, attributed to a higher surface proton concentration—relative to the bulk—induced by the surface electric field.<sup>19, 69-70</sup> An alternative explanation is that as chain length increases, van der Waals interactions between the chains bring the molecules closer together, packing the carboxylic acid head-groups and shielding the acidic hydrogen atom. As the shielding of the hydrogen atom increases, the  $pK_a$  increases.<sup>55, 71</sup>

More recently, surface tension titrations were used to measure the surface  $pK_a$  of octanoic, nonanoic, and decanoic fatty acids at the air-water interface.<sup>72</sup> The trend of increasing  $pK_a$  with increasing carbon chain length agrees with previous literature.<sup>71, 73-74</sup> However, a noticeable dip in the surface tension relative to water was also observed near the surface  $pK_a$  and attributed to the formation of more surface active acid-soap complexes between the protonated and deprotonated form of the fatty acids.<sup>72</sup> The observed cooperativity in the form of van der Waals interactions among the carbon chains, accompanied by interactions between the polar head groups, resulted in a decreased intermolecular distance and an increase in the surface  $pK_a$ .<sup>75</sup>

An infrared reflection-absorption spectroscopy (IRRAS) study of the pH dependence of L-phenylalanine at the air-water interface was reported by Vaida et al.<sup>76</sup> In contrast, this measurement revealed that the  $pK_a$  of the carboxylic acid group of this amino acid decreased at the interface relative to its value in the bulk. This experimental approach differs somewhat from SFG spectroscopy because the probe depth of IRRAS can be as large as 1–2  $\mu\text{m}$ , or even more depending on the frequency, in contrast to the

~1 nm (or less) surface depth typically probed by SFG.<sup>77</sup> Consequently, the layer probed by IRRAS may include a hydroxide rich subsurface that exists in the electric double layer to maintain charge-neutrality with the hydronium rich surface layer,<sup>78</sup> leading to a decreased surface  $pK_a$ .

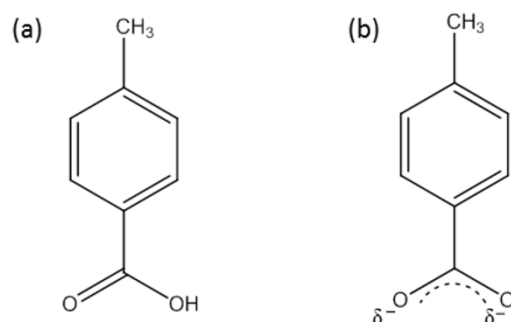


**Figure 2.1:** *p*-methyl benzoic acid (a) and its conjugate base, *p*-methyl benzoate (b).

Here we report sum-frequency generation spectra of a small organic acid, *p*-methyl benzoic acid (*p*MBA), pictured in **Figure 2.1**, in aqueous solution as a function of bulk solution pH, and spectral evidence of the formation of an acid-soap complex between *p*MBA and its conjugate base, *p*-methyl benzoate (*p*MBA<sup>-</sup>). Traditional Langmuir-Blodgett surface pressure experiments<sup>79-80</sup> are performed on amphiphilic molecules layered on an aqueous sub-phase under conditions in which there is a constant number of molecules  $N$  on the surface. Such systems are not formally in equilibrium, as the exchange of molecules with the aqueous sub-phase is neglected and experiments are performed under quasi-equilibrium conditions at best. For our SFG and surface pressure studies performed over a wide range of pH, the assumption of constant  $N$  breaks down since the solubility of the molecules of interest varies over many orders of magnitude. Our approach is to perform all experiments at the solubility limit, where the molecules

are always in equilibrium with the solid phase of the acid. The chemical potential of the dissolved molecules is then fixed in equilibrium at a particular temperature to a standard state set by the solid phase. The effective pH at the interface (set by the  $\text{H}_3\text{O}^+$  concentration at the interface) may be different from the bulk aqueous phase measured value.<sup>78, 81</sup> As the aqueous phase pH is varied at constant temperature and surface area, the solubility changes and the concentration of *p*MBA molecules in the bulk aqueous phase changes over two orders of magnitude, from  $\sim 300$  mM at the highest pH to  $\sim 3$  mM at the lowest pH. Nevertheless, the chemical potential of the acid molecules in the surface layer is still equal to their chemical potential in the solid crystalline state. Formal equilibrium is maintained over the entire pH range facilitating analysis.

For the  $\text{HA} \rightleftharpoons \text{A}^- + \text{H}^+$  acid-base reaction, the equilibrium condition on the corresponding chemical potentials is  $\mu_{\text{HA}} = \mu_{\text{A}^-} + \mu_{\text{H}^+}$ . (For notational convenience, we use  $\text{H}^+$  to indicate  $\text{H}_3\text{O}^+$ .) At the solubility limit at a given temperature,  $\mu_{\text{HA}}$  is set by the standard solid state and is a constant for all pH values. With the notional definition of pH,  $\mu_{\text{H}^+} = \mu_{\text{OH}^-} + k_B T \ln(10^{-\text{pH}})$  the chemical potential of the acid is therefore a strict linear function of pH with  $\mu_{\text{A}^-} = \mu_{\text{HA}} - \mu_{\text{OH}^-} + k_B T \ln(10^{\text{pH}})$ . The linear relationship between the bulk aqueous phase pH and  $\mu_{\text{A}^-}$  follows from chemical equilibrium and holds even for nonideal solutions when the activity coefficient is not 1, and in the case of non-ideal mixtures discussed below.

### **2.1.1 Theory Background**

In principle, a calculation of  $\mu_{\text{A}^-}$  and  $\mu_{\text{HA}}$  should be made using a molecular level model, along the lines of a recent theoretical calculation of the surface free energy using

the grand canonical ensemble to find the corresponding Landau potential.<sup>82</sup> A simpler phenomenological thermodynamic analysis is used here that assumes the existence of a cooperative interaction at the interface between the protonated and deprotonated forms of the organic acid. Our data suggest that the protonated and deprotonated form a *non-ideal* mixture represented by a negative value of the excess Landau Free energy. Analysis of such non-ideal mixtures takes a mean field approach common to the van der Waals continuum model and the random Bragg-Williams lattice gas, in the early work of Guggenheim<sup>83</sup> and Satchard<sup>84</sup> on non-electrolyte mixtures, in the even earlier activity models of Margules and van Laar<sup>85</sup>. The mean field approach also leads to the classic Redlich-Kister<sup>86</sup> algebraic representation models of thermodynamic potentials that are widely used by the experimental applied thermodynamics community. At the molecular level the deviation from ideal mixing arise from the microscopic interactions between *pMBA* and *pMBA*<sup>-</sup>. Viewing this most simply as a charge-dipole interaction in a dilute system, the dipole is aligned by the Coulomb field of the deprotonated acid, and suggests intuitively that the interaction should be attractive in the dilute limit. Such a cooperative interaction would be especially effective in a narrow range when the system is either not too acidic or not too basic, away from extremes of the pH scale. Attractive interactions can arise from van der Waals forces<sup>55, 71, 75</sup> or possibly from  $\pi$ -stacking interactions between aromatic rings. The proposed cooperativity is also in the spirit of traditional analysis of acidity and basicity in organic chemistry. A shortcoming of Mean Field Theory is that it cannot uniquely provide insights into the molecular level interactions, nor provide a good description of the role of fluctuations. One goal of our paper is to

report experimental observations that can motivate a more fundamental statistical mechanical analysis of the observed anomalous enhancement based on a microscopic model.

The proposed cooperative interaction that results in a negative value of the excess free energy has several consequences that can be investigated experimentally: (i) the total number of molecules at the interface can increase; (ii) the fraction of protonated vs deprotonated forms can change from the ideal values; (iii) there can be orientational changes as well phase changes from complex large-scale reorganization of the molecules in domains at the interface and changes in water structure as a function of pH. All of the SFG experiments reported here are performed at a constant value of the chemical potential referenced to the standard state of solid benzoic acid at room temperature of  $293\pm 1$  K, facilitating comparison and analysis of novel phenomena.

SFG measurements of the carbonyl and carboxylate stretching modes and the aromatic ring stretching modes of *p*MBA and its conjugate base, *p*MBA<sup>-</sup>, over the pH range from 2 to 12 are reported here. The SFG intensities of the carbonyl and carboxylate stretching modes provide a surface-selective titration of ionized and non-ionized (protonated) forms. The benzene derived ring mode,  $\nu_{8a}$ , yields orientation information independently of ionization state at the interface because the frequency of this mode is independent of the state of ionization. However, as shown below, an anomalously large SFG intensity was observed in a narrow pH range for both the ionized and unionized methyl benzoic acid, about two pH units higher than the bulk solution *p*MBA  $pK_a$ ,

suggesting a strong, cooperative adsorption between *p*-methyl benzoic acid and its conjugate base at this very specific air-aqueous interface solvation condition.

The experiments reported here are of interest to the broader class of phenomena and phase behavior<sup>87</sup> in systems with reduced spatial dimensions. In a Langmuir-Blodgett experiment, the behavior of molecules in a  $\sim 1$ -2 nm thick layer at the surface may be considered to be two-dimensional. The behavior of molecular systems confined to 2D interfaces is qualitatively different from what is observed in 3D. Following a suggestion by deGennes, Andelman et al<sup>88</sup> analyzed the effect of long range electrostatic interactions on phase behavior in Langmuir-Blodgett monolayers by adapting the Flory-Huggins theory<sup>89</sup> more traditionally used to describe polymer solutions. When the molecules are moved to the air-water interface, the reduced dielectric constant leads to long-range forces. In bulk water, dipolar electrostatic interactions are strongly screened by the large dielectric constant  $\epsilon \sim 80$ , and the interaction energy is reduced by  $(1/\epsilon)^2$ . In the bulk aqueous phase, electrostatic interactions can therefore be safely neglected in the dilute limit. The effective value of the dielectric constant  $\epsilon_{surf}$  close to the interface is not known precisely, but is much smaller than  $\sim 80$ . In continuum models of the interface  $\epsilon_{surf}$  can range from 4-8 and simply translating dipole to the surface results in a  $\sim 100$ -fold increase in interaction energy. The energy appears in the Boltzmann factor exponents. Thus weak electrostatic interactions that are negligible in the bulk aqueous phase become significant on the surface, and the resulting phase behavior of molecules at interfaces can be dramatically different. The theoretical studies by Andelman et al.<sup>90</sup> explored the effect of long-range repulsive forces, and the emergence of new modulated thermodynamic phases

at the air-water interface. The experiments show that attractive interactions can also lead to novel cooperative phenomena that are manifest only at the air-water interface.

## 2.2 Experimental

*Sample Preparation.* *p*-methyl benzoic acid was purchased from Fisher Scientific. Standardized 1M NaOH and 1M HCl were purchased from Sigma Aldrich. All solutions were prepared in Millipore water (18.2 M $\Omega$ ·cm). A stock solution of 300 mM, pH 12 *p*-methyl benzoate was used to make the lower pH samples. 1M HCl was added to the stock solution until the desired pH was reached. The solubility of *p*MBA is pH dependent, so a white precipitate of solid *p*MBA formed upon addition of 1M HCl. This ensured that all of the samples were prepared at constant chemical potential. The solid *p*MBA precipitate was filtered (Fisherbrand 25 mm syringe filter, 0.2  $\mu$ m pore size) prior to measuring the surface pressure and sum-frequency generation (SFG) spectra. The pH of all solutions were recorded prior to filtering and directly after data acquisition using an Accumet Basic 15+ pH meter to insure no pH changes occurred due to atmospheric exposure.

*Surface Tension Measurements.* Surface tension was measured using a Langmuir-Blodgett (LB) trough and a Pt Wilhelmy plate (KSV NIMA). For surface tension measurements, the Pt plate and sample dish were plasma cleaned (Harrick Plasma, Model PDC-001) and rinsed with ethanol. Millipore water was used for the final rinse, and N<sub>2</sub> (g) was used to dry the Pt Wilhelmy plate prior to each measurement. *p*-methyl benzoic acid solutions were placed in the dish, and the Wilhelmy plate was placed on the balance that came equipped with the LB trough and dipped into solution. The system was allowed

to come to a steady state before the surface pressure was recorded (approximately 10-20 minutes).

*Sum-Frequency Generation (SFG) Spectroscopy.* All SFG spectra were recorded with a broad-band<sup>44</sup> vibrational sum-frequency spectrometer as previously described<sup>43</sup> and normalized relative to the non-vibrational SFG response from a GaAs crystal. The bandwidths (FWHM) of the overlapping visible (800 nm) and IR beams were  $\sim 7 \text{ cm}^{-1}$  and  $160 \text{ cm}^{-1}$ , respectively. Relative incident laser polarizations were determined by half-wave/polarizer elements, and the selected signal polarization component was defined by a polarizer in the signal beam path. SFG spectra in the *p*MBA carbonyl region were corrected for ambient water absorption.

The intensity of the sum-frequency generation (SFG) signal,  $I_{\text{SFG}}$ , polarized along the  $i^{\text{th}}$  direction is proportional to the square of the second order susceptibility,  $\chi_{ijk}^{(2)}$  as given by:

$$I_{\text{SFG}i} \propto \left| \chi_{ijk}^{(2)} \cdot E_j^{800} \cdot E_k^{\text{IR}} \right|^2 \propto \left| \chi_{ijk}^{(2)} \right|^2 I_{800} I_{\text{IR}} \quad (2.1)$$

where  $I_{800}$  and  $I_{\text{IR}}$  are the intensities of the incident 800 nm and IR beams polarized along the  $j$  and  $k$  lab fixed frame directions, respectively. The second order susceptibility,  $\chi_{ijk}^{(2)}$ , is dependent on the surface number density,  $\rho_s = N_s/A_s$ , where  $N_s$  is the total number of molecules on the surface of area  $A_s$ , and the molecular orientation of the vibrator at the interface:

$$\chi_{ijk}^{(2)} = \rho_s \sum_{i'j'k'} \langle R_{ii'} R_{jj'} R_{kk'} \rangle \beta_{i'j'k'}^{(2)} \quad (2.2)$$

$\beta_{i'j'k'}^{(2)}$  represents the microscopic hyperpolarizability elements in the molecular fixed ( $i'j'k'$ ) frame, and  $R_{\lambda\lambda'}$  are the elements of the Euler rotational transformation matrix to the space fixed ( $ijk$ ) frame.<sup>40</sup> Since the homodyne SFG signal depends quadratically on the vibrator's surface number density and molecular orientation (Eqs. 2.1 and 2.2), changes in both of these properties may contribute in general to observed changes in SFG spectra as a function of pH. In experiments reported here SFG signals are collected from molecules in the intersection region of the overlapped focal spots of the 800 nm and IR beams on the surface, corresponding to an overlap region area of  $\sim 100 \mu\text{m}^2$ .

#### *Spectroscopic Calculations*

Calculations of the IR and Raman spectra and transition moment directions of *p*MBA were performed with Gaussian 09 using B3LYP/6-311+G level density functional theory (DFT). The hyperpolarizability elements,  $\beta_{i'j'k'}^{(2)}$ , for the  $\nu_{8a}$  ring stretching mode of *p*MBA were calculated by using the Gaussian 09 Polar method. The resulting calculated hyperpolarizability element values are listed in the Supporting Information.

## **2.3 Results**

### ***2.3.1 Titration of *p*-Methyl Benzoic Acid in Bulk Solution and via Surface Tension Measurements***

Traditional measures of surface tension<sup>79-80</sup> were carried out for *p*MBA solutions in the 2 to 12 pH range in order to initially monitor the pH dependence of the surface adsorption of this acid (**Fig. 2.2**) via this classical technique.

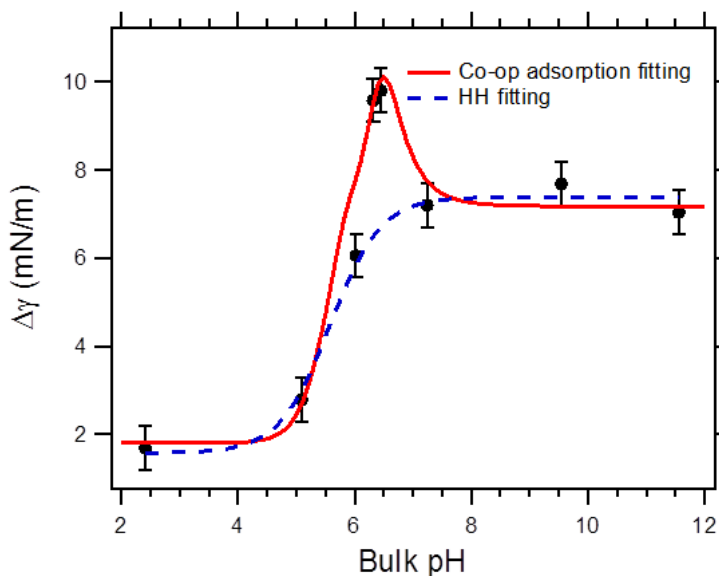


**Figure 2.2:** The surface tension of *p*-methyl benzoic acid (*p*MBA) solution is plotted as a function of bulk solution pH relative to bulk water ( $\gamma_{\text{water}} - \gamma_{\text{soln}}$ ).  $\Delta\gamma$  increases significantly at pH 6.3, indicative of more species present at the interface at this pH. The dashed line is a fit to the Henderson-Hasselbalch form with different areas per molecule for the acid and base. The red line is a fit using a model that includes cooperative interactions described in the paper.

Since the *p*MBA solubility in the bulk is pH dependent, all of the solutions were prepared at saturated conditions. Thus, all of the SFG experiments reported here are performed at a constant value of the chemical potential referenced to the standard state of solid benzoic acid at room temperature of  $293 \pm 1$  K, facilitating comparison and analysis of the observed effects. The results show that the surface pressure of *p*-methyl benzoic changes non-monotonically as pH increases. At low pH, the surface pressure is about  $1.6 \text{ mN m}^{-1}$  relative to pure water. A significant change in surface pressure was observed at  $\text{pH } 6.3 \pm 0.2$ , followed by lower surface pressure changes at higher pH that asymptotes to about  $7 \text{ mN m}^{-1}$  (**Fig. 2.2**). The anomalous pressure increase occurs over a narrow pH range of less than 1 pH unit roughly between pH 6 and pH 7. Several additional observations can be immediately made from **Figure 2.2**: (i) The observed changes are not due to the pH-

dependence of the surface tension of pure water. It has long been known that the surface tension of water is known to be almost insensitive to pH, with changes of  $< 0.5 \text{ mN m}^{-1}$  throughout the pH range 2-14, including a small feature characteristic pK near 4.5 due to the Jones-Ray effect attributed variously to adsorption of ions or to field-induced water-water correlations.<sup>91</sup> Even in the presence of 1 M salt still results in changes of  $< 1 \text{ mN m}^{-1}$ .<sup>82</sup> The changes observed in our experiments under salt-free conditions in **Figure 2.2** are larger than these upper limits appear to be entirely due to the presence of the acid ( $p\text{MBA}$ ) and its conjugate base ( $p\text{MBA}^-$ ) at the air-water interface. (ii) The observed changes arise from non-ideal mixing. At low pH, where the molecules are all protonated, the observed asymptote of about  $1.6 \text{ mN m}^{-1}$  the ideal gas estimate of the surface density gives  $\Delta\pi/k_{\text{B}}T \sim 4 \times 10^{17} \text{ molecule/m}^2$  with an area per molecule of  $\sim 2.5 \text{ nm}^2$ . In an ideal gas deprotonation does not change the number density and the surface pressure would be expected to be independent of pH, indicated by the dotted red line in **Figure 2.2**. The observed increase at high pH must arise from non-ideal behavior. At extremely high pH, when nearly all the molecules are deprotonated and are negatively charged, the asymptotic excess surface pressure of  $\sim 7 \text{ mN m}^{-1}$  arises from repulsive interactions that modify ideal gas behavior as discussed later. The dashed blue line is based on the Henderson-Hasselbalch (HH) model, with different areas per molecule for  $p\text{MBA}$  and  $p\text{MBA}^-$  where the molecules do not interact directly with each other. Data in the narrow range near pH 6.3 (**Fig. 2.2**) deviates strongly from the HH model, which we attribute to cooperative interactions between the acid-soap complexes. The red solid line is a fit which incorporates a simple phenomenological model for the cooperative interaction

described later in the discussion section. **Figure 2.2** shows that surface pressure measurements alone are not sufficient to disentangle the contributions of density changes, interaction effects, and orientation effects at the molecular level. This provides strong motivation for spectroscopic studies and the sum-frequency generation experiments described next.

### 2.3.2 Titration of *p*-Methyl Benzoic Acid via SFG

To gain a better molecular level understanding of the anomalous observed enhanced surface adsorption of *p*MBA near pH 6.3 (**Fig. 2.2**), measurements of the SFG intensities of the carbonyl and carboxylate vibrations of *p*-methyl benzoic acid and *p*-methyl benzoate, respectively, were carried out as a function of pH. The pH-dependent SFG signals, in *ssp* polarization (*s*-polarized SFG, *s*-polarized visible, and *p*-polarized IR), due to resonance with the protonated *p*-methyl benzoic acid carbonyl stretch at  $1700\text{ cm}^{-1}$ , are shown in **Figure 2.3a**. The vibrational mode at  $1700\text{ cm}^{-1}$  is also a reporter of the state of ionization of the -COOH group, while the ionized carboxylate group ( $\text{COO}^-$ ) symmetric stretch (*ss*) vibration of *p*-methyl benzoate (*p*MBA<sup>-</sup>), the deprotonated conjugate base of *p*-methyl benzoic acid, has a peak transition frequency of  $1395\text{ cm}^{-1}$ . As pH increases from 2 to 12, one would expect that the carbonyl mode ( $1700\text{ cm}^{-1}$ ) would exhibit monotonically decreasing SFG intensity, as fewer protonated *p*MBA molecules are present in solution. However, in analogy to the observed surface pressure pH dependence (**Fig. 2.2**), a non-monotonic SFG intensity pH dependence is observed for this  $1700\text{ cm}^{-1}$  band as shown in **Figure 2.3a**. More specifically, the SFG intensity abruptly increases between pH 6.0 and 6.5 and then decreases at pH  $\sim 7$  and above (**Fig.**

**2.3b).** To more clearly illustrate the pH dependence of the observed SFG signal, the homodyne signal region (1625 – 1800 cm<sup>-1</sup>) is fit with a function form for vibrational mode that includes a non-resonant baseline ( $\chi_{NR}^{(2)}$ ) and Lorentzian vibrational resonant contribution:

$$I_q \propto \left| \chi_{NR}^{(2)} + \frac{A_q}{\omega_{IR} - \omega_q + i\Gamma_q} \right|^2 \quad (2.3)$$

where  $A_q$ ,  $\omega_q$ , and  $\Gamma_q$  are the amplitude, the frequency and the line width of the  $q$  vibrational transition. Contributions from the overlapping SFG water bending mode<sup>92-93</sup> were taken into consideration during the fitting analysis in the carbonyl stretching region. Good fits to the observed  $p$ MBA SFG spectral features are obtained with this procedure (see Supporting Information). The SFG peak amplitude of the  $q$  vibrational resonance is linearly proportional to the molecular number density of contributing vibrators at the surface (**Fig. 2.3b**). Hence the peak amplitude of the  $p$ MBA carbonyl stretch resulting from this SFG fitting procedure is plotted as a function of pH in **Figure 2.3b**. The frequency of this vibrational mode, which is dominated by C=O vibrational character, remains essentially unchanged across this pH range. The inset in **Figure 2.3b** shows a plot of the anomalous increase of the 1700 cm<sup>-1</sup> carbonyl stretch peak amplitude in the titration curve of the protonated acid at higher pH resolution. The width of this SFG intensity anomaly (**Fig. 2.3b**) is > 1 pH unit. Such non-monotonic SFG dependence has not been previously observed for acid-base titrations at an interface.

In addition to the carbonyl vibration of  $p$ MBA, the SFG intensity of the carboxylate (COO<sup>-</sup>) symmetric stretch vibration of  $p$ -methyl benzoate ( $p$ MBA<sup>-</sup>), the

deprotonated conjugate base of *p*-methyl benzoic acid, at  $1395\text{ cm}^{-1}$  was also measured as a function of pH. Observed SFG spectra in the  $1300 - 1500\text{ cm}^{-1}$  region acquired with the same *ssp* polarization configuration are shown in **Figure 2.3c**. As the pH increases from 2 to 12, the SFG intensity of the carboxylate band increases as one would expect due to the increase in solution proton accepting strength. However, as seen for the carbonyl stretching feature (**Fig. 2.3a**), the carboxylate SFG intensity increase is also not monotonic and exhibits a maximum at pH 6.5. This anomalous pH dependence is summarized in a plot of the  $\text{COO}^-$  (*ss*) amplitude vs. pH, shown in **Figure 2.3d**. Between pH  $\sim 7$  and 12 the peak amplitude of this band in the SFG spectrum remains nearly constant at a value  $\sim 16\%$  lower than at the pH 6.5 maximum.

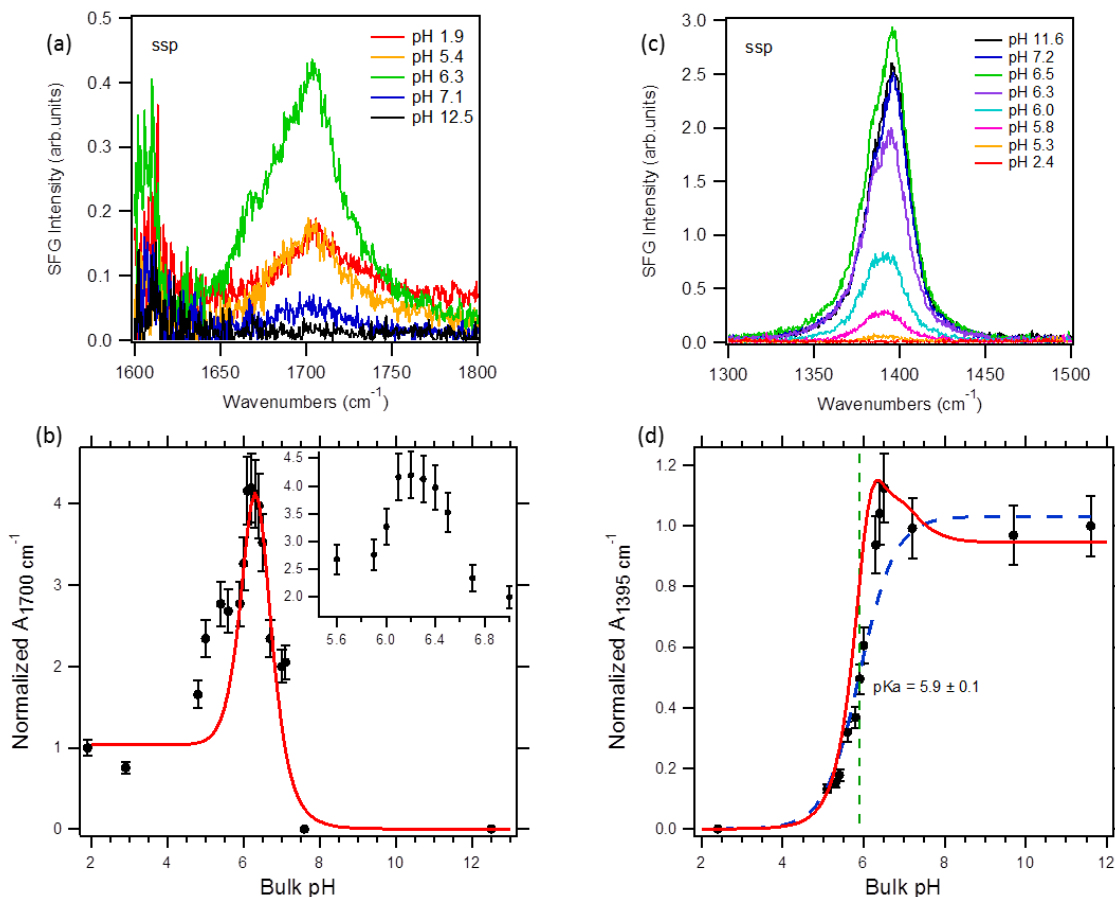


**Figure 2.3:** (a) SFG spectra of C=O carbonyl stretch of *p*-methyl benzoic acid (*p*MBA) in the protonated form. The peak intensity unexpectedly increases at pH 6.3. Note the small shoulder on the pH 6.3 spectrum is an artifact of the water absorption correction. (b) A plot of normalized (to the amplitude of the lowest pH solution) SFG peak amplitude from fittings for the carbonyl stretch centered 1700 cm<sup>-1</sup> as a function of bulk pH. The red line is a fit that includes cooperative interactions. (c) SFG spectra of COO<sup>-</sup> carboxylate (*ss*) of deprotonated *p*-methyl benzoate (*p*MBA<sup>-</sup>). (d) Plot of the normalized (to the amplitude of the highest pH solution) SFG peak amplitude from fittings for the carboxylate stretch centered at ~1395 cm<sup>-1</sup>. The red line is a fit that includes cooperative interactions.

The anomalous SFG intensity maximum in the titration curves of both *p*-methyl benzoic acid and its conjugate base occur in nearly the same narrow pH range (~6.3-6.5) could result from a simultaneous increase in *p*MBA and *p*MBA<sup>-</sup> number densities, in this narrow pH range. The SFG signal enhancement mechanism will be discussed in greater

detail below. Alternatively, since  $\chi_{ijk}^{(2)}$  is also dependent on the orientation of the transition dipole with respect to the electric vectors of the incident signal fields (Eq. 2.2), a significant change in molecular orientation of *p*MBA and *p*MBA<sup>-</sup> molecules at the air-water interface at this pH could be responsible for these non-monotonic pH dependent SFG intensity effects. Relative polarization SFG measurements are required to more fully characterize the origin of this anomalous SFG intensity effect.

### ***2.3.3 Orientation Analysis of p-Methyl Benzoic Acid and its Conjugate Base at the Air-Water Interface***

In order to disentangle the relative importance of orientation and number density contributions to the enhancement of the observed SFG intensity, a polarization analysis of *p*MBA and *p*MBA<sup>-</sup> SFG signals was performed as a function of pH at the aqueous interface. The SFG intensities of the benzene-like ring stretching mode ( $\nu_{8a}$ )<sup>94</sup> of *p*MBA and *p*MBA<sup>-</sup> for two different experimental polarization conditions, *ssp* and *ppp*, were measured for this purpose. For the *ssp* polarization configuration the SFG signal field (*s*) is polarized along the same direction as the visible field (*s*) and perpendicular to the IR field (*p*). In the *ppp* configuration, all incident and signal electric vectors are parallel to one another, but the SFG signal is polarized perpendicular to the *ssp* signal direction. Ratios of these SFG polarization configuration specific intensities cancel SFG intensity effects attributable to interfacial number density changes, allowing separation of the contributions due to orientation effects only, at least within the constraints of the SFG intensity modeling analysis outlined below.

The benzene-like ring stretching mode ( $\nu_{8a}$ ) at 1610 cm<sup>-1</sup> (**Fig. 2.4**) was chosen for the polarization analysis instead of the previously described carbonyl stretch portion of

the SFG spectrum (**Fig. 2.3**) because the IR transition dipole of this ring stretching mode is more closely aligned with the orientation of the (near)  $C_{2v}$  molecular axis of these molecules. Further, since the frequency of this ring stretching mode,  $1610\text{ cm}^{-1}$ , is essentially independent of the state of  $-\text{COOH}$  ionization, and the SFG signal observed for this band will be due to both  $p\text{MBA}$  and  $p\text{MBA}^-$  surface populations. As shown in **Figure 2.4a**, the observed intensity of this SFG band in *ssp* polarization is nearly the same at all solution pH's except for the anomalous region at  $\sim\text{pH } 6.3$ , where the intensity is approximately four times greater than at all other pHs. Furthermore, a slight red peak shift of  $\sim 3\text{ cm}^{-1}$  is observed in the SFG spectra for this ring stretching band (**Fig. 2.4a**). This small peak shift could be due to the formation of the acid-soap complex at the air-water interface, owing to Van der Waals forces between the benzene rings in the form of  $\pi$ -stacking interactions between  $p\text{MBA}$  and  $p\text{MBA}^-$  molecules. The SFG spectra of the benzene ring stretch region as a function of pH resulting from *ppp* polarization configuration is shown in **Figure 2.4b**. The *ppp* SFG intensity of this mode also dramatically increases at pH 6.3 relative to pH values  $< 6$ , but maintains this large signal magnitude for all higher pH solutions. A change in the *ppp/ssp* peak intensity ratio of the benzene-like ring stretching mode at  $1610\text{ cm}^{-1}$  as a function of pH is indicative of a change in the relative orientation of  $p\text{MBA}$  and  $p\text{MBA}^-$  at the interface.<sup>40, 95</sup> Similar observations were found for the  $\text{COO}^-$  carboxylate symmetric stretching mode at  $1395\text{ cm}^{-1}$  in *ssp* and *ppp* polarizations (see Supporting Information). Furthermore, the SFG signal due to resonance with the methyl  $\text{CH}_3$  asymmetric stretching (*as*) mode also displayed similar polarization characteristics (Supporting Information). However, the low

signal-to-noise ratio due to interference from the tail of the water OH stretch and the hydronium O-H band did not allow a quantitative polarization analysis to be carried out for this *as* CH<sub>3</sub> mode as discussed here for the  $\nu_{8a}$  benzene-like ring stretching mode.

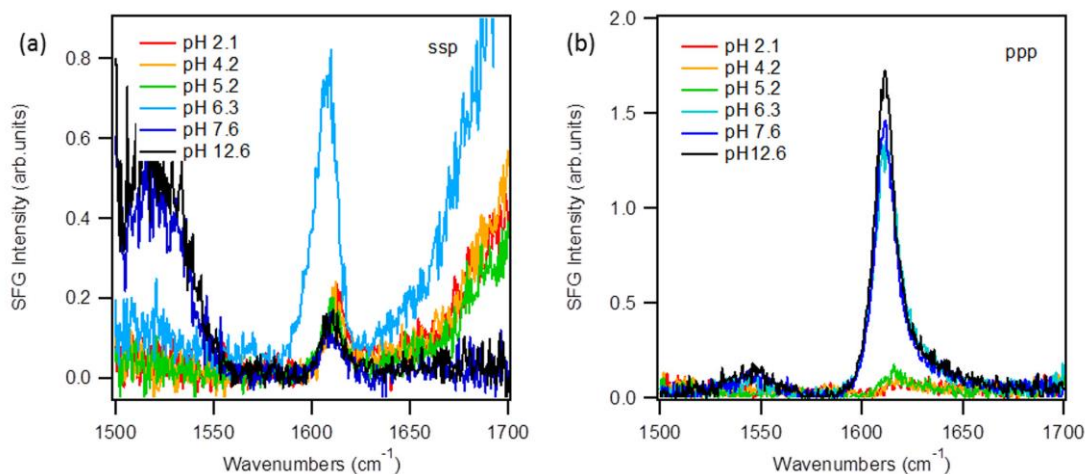


**Figure 2.4:** (a) SFG spectra of the 8a ring stretching mode for *p*MBA and *p*MBA<sup>-</sup> in *ssp* polarization. The peak intensity is significantly higher at pH 6.3 as observed in the carbonyl stretching region at 1705cm<sup>-1</sup>. (b) SFG spectra of the 8a ring stretching mode for *p*-methyl benzoic acid in *ppp* polarization. The intensity increases significantly at pH 6.3 and above. These spectra are indicative of a change in orientation, as the *ppp/ssp* ratio changes with pH.

In order to determine the orientation of *p*-methyl benzoic acid and its conjugate base at the air-water interface, SFG spectra of the benzene-like stretching mode of *p*MBA were obtained in two different polarization conditions, *ssp* and *ppp*, as shown in **Figure 2.4**. The SFG intensities at 1610 cm<sup>-1</sup> for both polarization configurations and their ratios as a function of pH are summarized in Table 1.

The SFG signal intensity is proportional to the square of the second order susceptibility,  $\chi_{ijk}^{(2)}$ , which is proportional to the vibrator number density, orientational configuration of the molecule, and the sum frequency molecular hyperpolarizability,  $\beta_{i'j'k'}^{(2)}$  (Eq. 2.2) with respect to the molecular frame defined by  $i'$ ,  $j'$ ,  $k'$ . A B3LYP

density functional theory (DFT) calculation was used to determine  $\beta_{i'j'k'}^{(2)}$  for the  $\nu_{8a}$  stretching mode of *p*-methyl benzoic acid. Using the calculated molecular fixed frame hyperpolarizabilities, the polarization specific effective sum frequency susceptibilities,  $\chi_{ssp}^{(2),eff}$  and  $\chi_{ppp}^{(2),eff}$ , were calculated following a previously published procedure,<sup>40, 96</sup> as a function of angular orientation of the IR transition dipole moment at the interface relative to the surface normal. See Supporting Information for details of the calculation. The effective sum frequency susceptibilities,  $\chi_{ssp}^{(2),eff}$  and  $\chi_{ppp}^{(2),eff}$ , differ from the second order susceptibility,  $\chi_{ijk}^{(2)}$ , in that they account for the experimental geometry, interfacial refractive indices, and the reflection of *s* and *p*-polarized beams.<sup>38-39, 97-98</sup> Tilt ( $\theta$ ) and twist angles ( $\psi$ ), depicted in **Figure 2.5**, are needed to fully define the orientation of a  $C_{2v}$  molecule at the surface.<sup>96</sup>  $\theta$  is the angle between the IR transition dipole moment and the surface normal, and  $\psi$  is the angular rotation of the benzene ring plane around the vibrational transition moment, effectively the symmetry axis, out of the plane formed by the surface normal and the transition moment, as shown in **Figure 2.5**. The *calculated* SFG dependence of the  $1610\text{ cm}^{-1}$  ring stretching mode as a function of tilt angle ( $\theta$ ) corresponding to twist angles ( $\psi$ ) of  $0^\circ$  and  $90^\circ$  for both experimental *ssp* and *ppp* polarization configurations are shown in **Figure 2.6a**. As seen in this figure, the SFG intensities are essentially independent of the twist angle ( $\psi$ ) due to the in-plane stretching character of this mode, and thus only the tilt angle ( $\theta$ ) dependence of the molecular orientation at the surface is significantly relevant to this analysis. **Figure 2.6a** shows that the SFG intensity of this mode is however strongly dependent on  $\theta$ , the tilt orientation of

the transition moment axis relative to the surface normal. For the *ppp* configuration, the SFG intensity is strongest for molecular orientations with the *p*MBA and *p*MBA<sup>-</sup> symmetry axis oriented along the surface normal and results from the favorable transition dipole alignment of the incident electric vectors. In contrast, this ring stretching mode has a minimum in this configuration and is a maximum at an angle of  $\sim 52^\circ$  relative to the surface normal for the corresponding *ssp* configuration, which has perpendicularly polarized incident vectors relative to the allowed transition moment directions.

**Table 2.1. Relative SFG peak intensity *ppp/ssp* ratio at  $1610\text{ cm}^{-1}$  as a function of tilt angle ( $\theta$ )**

<b>pH</b>	<b>2.1</b>	<b>4.2</b>	<b>5.2</b>	<b>6.3</b>	<b>7.6</b>	<b>12.6</b>
<b><i>ssp</i> intensity (peak height)</b>	0.24	0.23	0.20	0.82	0.16	0.16
<b><i>ppp</i> intensity* (peak height)</b>	0.25	0.26	0.35	3.4	3.6	4.3
<b><i>ppp/ssp</i></b>	1.0	1.2	1.7	4.1	22	27
<b>Average Orientation Angle (<math>^\circ</math>)</b>	33.1	32.7	30.7	25.0	7.1	4.3

\**ppp* intensity was multiplied by 2.5 to account for the difference in the collection time

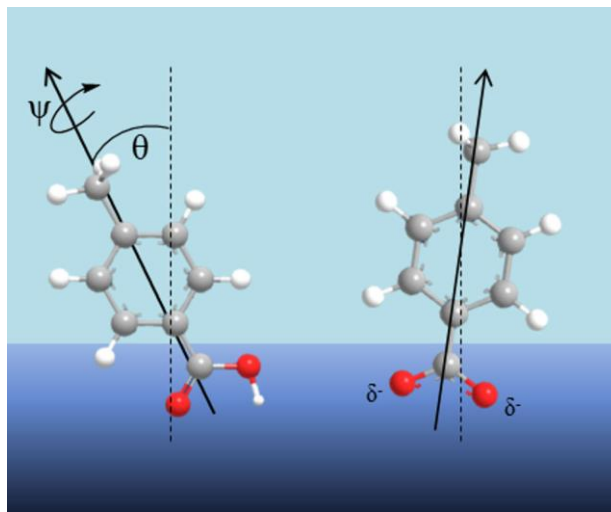


**Figure 2.5:** *p*-methyl benzoic acid (left) and *p*-methyl benzoate (right) on the air water interface.  $\theta$  represents the tilt angle of the transition dipole moment (solid black line) relative to the surface normal (dashed line), and  $\psi$  represents the twist angle. *p*-methyl benzoic acid is tilted approximately  $33^\circ$  relative to the surface normal, whereas *p*-methyl benzoate is orientated more upright, approximately  $4^\circ$  relative to the surface normal.

The ratio of the calculated SFG intensities of the  $1610\text{ cm}^{-1}$  ring stretching mode for the two polarization configurations, *ppp*:*ssp*, are plotted in **Figure 2.6b** as a function of the tilt angle,  $\theta$ . The SFG intensity is strongly favored for the *ppp* relative to the *ssp* configuration for  $\theta$  between  $\sim 0$  and  $\sim 35^\circ$  and the *ppp*:*ssp* ratio monotonically decreases by about an order of magnitude as the tilt angle increases over this range (**Fig. 2.6b**). For larger tilt angles, the *ppp*:*ssp* intensity ratio remains roughly constant at an average value of  $\sim 0.2$ .

The experimentally determined *ppp*:*ssp* SFG intensity ratios (given by peak heights) for the benzene-like ring stretching mode for pH's in the range from 2 to 12 are indicated on the calculated *ppp*:*ssp* SFG curve thus providing a measure of the average tilt angle of the molecules relative to the surface normal as a function of pH (Table 2.1). These experimental ratios display a consistent trend. As pH increases from 2 to 12, the

*ppp*:*ssp* SFG ratio increases, corresponding to smaller  $\theta$  values, i.e. the molecules at the interface are becoming increasingly oriented closer to the surface normal with increasing pH. Furthermore, this orientation effect is predicted to be monotonic as the solution becomes more basic (**Fig. 2.6b**). Assuming the surface populations at pH 2 and pH 12 are 100% protonated *p*-methyl benzoic acid and 100% deprotonated *p*-methyl benzoate, respectively, this polarization analysis predicts that the near  $C_{2v}$  symmetry axis is oriented at a  $33^\circ$  tilt angle for the protonated form and a  $4^\circ$  tilt angle for the deprotonated form.

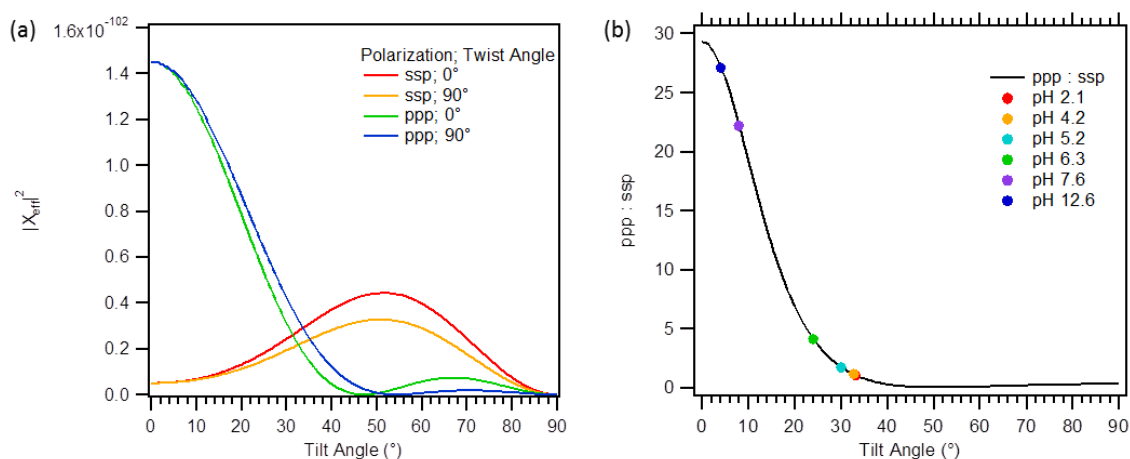


**Figure 2.6:** (a) Square of the effective sum frequency susceptibility (SFG intensity) vs tilt angle ( $\theta$ ) for twist angles of  $\psi = 0$  and  $90^\circ$  in *ssp* and *ppp* polarization configurations for the 8a ring stretching mode of *p*MBA and *p*MBA<sup>-</sup>. (b) Ratio of *ppp*/*ssp* intensity based on the square of the effective sum frequency susceptibility vs tilt angle ( $\theta$ ). The solid markers correspond to the observed ratio in the SFG spectra of the 8a ring stretching mode for *p*-methyl benzoic acid at various pH values. The orientation of *p*-methyl benzoic acid at specified pH values can be determined from where the measured ratio intersects the x-axis.

Thus, although a decreasing tilt angle from  $33^\circ$  at pH 2 to  $4^\circ$  at pH 12 can explain the observed increase in SFG intensity for the  $\nu_{8a}$  mode in *ppp* polarization as a function of increasing pH, it cannot explain the anomalous increased SFG intensity in the *ssp*

polarization (**Fig. 2.4**). Based on these calculations, in order to maximize the SFG intensity in *ssp* polarization, the tilt angle needs to increase to  $\sim 50^\circ$  at pH 6.3 (**Fig. 2.6a**), near the maximum in the tilt angle dependence of  $|\chi_{\text{eff}}|^2$ . However, this is not consistent with the experimentally observed pH dependent *ppp/ssp* polarization ratios (**Fig. 2.6b**). If the tilt angle increased to maximize the SFG intensity observed in *ssp* polarization (tilt angle,  $\theta = 50^\circ$ ) at pH 6.3, the SFG intensity in *ppp* polarization must correspondingly vanish at this pH, in contrast to the observed *ppp*  $v_{\text{sa}}$  SFG intensity increase at pH 6.3. Hence, we attribute the anomalous increase in SFG intensity at pH 6.3 (**Fig. 2.3a**) predominantly arising from an increase in the number of *pMBA* molecules at the interfacial region.

The analysis suggests that due to the cooperative interaction, the presence of *pMBA* can tilt the orientation of *pMBA*<sup>-</sup>, but this effect is only evident in the anomalous region. Inclusion of this effect results in the fit shown in **Figure 2.3** where the SFG signal of the carboxylate signal is reduced compared to what one would expect purely from density increase. Similarly, the presence of *pMBA*<sup>-</sup> can also tilt the orientation of *pMBA* in the anomalous region, leading to an increase in the SFG signal from the carbonyl stretch. The presence of the second species of molecule acts like a mean field that tilts the molecular orientation due to interactions that tend to align the molecular axes closer.

## 2.4 Discussion

### 2.4.1 Anomalous Surface Adsorption Indicates Cooperativity

The measurement of surface tension or surface pressure is a classic technique for investigating surface specific effects. Surface pressure measurements provide a measure

of surface density at the interface, i.e. an increase in surface pressure corresponds to more molecules at the interface. In the surface pressure measurements of aqueous *p*-methyl benzoic acid solutions, an anomalous increase in surface pressure at pH 6.3 was observed (**Fig. 2.2**). Although surface pressure measurements are indicative of a change in the total number of molecules at the interface, it cannot distinguish different molecular species at the interface.

At pH 6.3 both *p*MBA and its conjugate base may be present at the interface in the form of an acid-soap complex, therefore SFG measurements were used to determine whether these species were adsorbed to the air-water interface. When monitoring the carbonyl and carboxylate vibrations of *p*-methyl benzoic acid and *p*-methyl benzoate respectively via SFG spectroscopy, an increase in SFG intensity was observed at this pH. If the narrow range of pH units between 6.0 and 6.5 is ignored, the SFG titration follows a standard Henderson-Hasselbalch curve that one would observe in bulk for a weak acid and strong base. That is, at low and high pH the signal intensity remains relatively constant, and between pH 6 and 7 a rapid change in signal intensity is observed. However, in the narrow range of pH units between 6.0 and 6.5, the carbonyl peak intensity increases (**Fig. 2.3b**), and a maximum in the carboxylate peak intensity is observed (**Fig. 2.3d**). This anomalous feature is intrinsic only to the surface, as it is not observed in bulk solution titrations of *p*MBA (**Fig. S2.3** of the Supporting Information). The surface pressure studies and SFG studies both suggest that the total number of molecules changes as a function of pH. Additionally, fluctuations in the orientation of *p*MBA and its conjugate base may also contribute to the observed deviations from ideal

behavior. We discuss a thermodynamic model of the increase in population first, followed by a discussion of the orientation effects.

#### 2.4.2 Thermodynamic Analysis of Population and Non-ideal Activity in Acid-Base Mixtures

At constant chemical potential, equilibrium is determined by the minimum of the grand canonical Landau potential  $\Omega(T, A_s, \mu_i) = -\pi A_s$ , where  $A_s$  is the surface area. Surface pressure isotherms directly measure changes in this potential. Statistical mechanical models of non-ideal mixtures use the density as the natural parameter for virial expansion of the Helmholtz Free energy  $F = \Omega + \mu_{A^-} N_{A^-} + \mu_{HA} N_{HA} = F_{ideal} + F_{int}$ .  $F_{ideal}$  is the free energy in the absence of interactions. The interaction contribution,  $F_{int}$ , leads to mixing rules in binary fluid mixtures.<sup>99-100</sup> The comprehensive paper by Ben-Amotz and Widom<sup>101</sup> on non-ideal mixtures describes the conversion between the different ensembles. Following their treatment, the interaction contribution  $F_{int}$  is expanded in terms of the number densities of the two species densities  $\rho_{A^-} = N_{A^-}/A_s$  and  $\rho_{HA} = N_{HA}/A_s$  with the total number density  $\rho \equiv \rho_{A^-} + \rho_{HA} = N/A_s$ . The leading term in the interaction energy per unit area may be written

$$\frac{1}{A_s k_B T} F_{int} = \Phi(\rho_{A^-}, \rho_{HA}) = \rho_{A^-}^2 \Psi_{A^-} + \rho_{HA}^2 \Psi_{HA} + 2\rho_{A^-} \rho_{HA} \Psi_{A^- HA} + \dots \quad (2.4)$$

The coefficient terms  $\Psi_{ij}$  are in general functions of the densities and can be readily related to virial coefficients that characterize deviation from ideal behavior and the mixing rules derived by Ben-Amotz and Widom (See Supporting Information, Section D). The expressions for the chemical potentials  $\mu_{A^-} = (\partial F / \partial N_{A^-})_{A_s, N_{HA}, T}$  and  $\mu_{HA} = (\partial F / \partial N_{HA})_{A_s, N_{A^-}, T}$  give coupled nonlinear equations of the form:

$$\mu_{A^-} = k_B T \ln \left( \frac{\rho_{A^-}}{\rho_{0A^-}} \right) + \left( \frac{\partial F_{int}}{\partial N_{A^-}} \right)_{A_s, N_{HA}, T} \Rightarrow \rho_{A^-} = \rho_{0A^-} e^{\beta \mu_{A^-}} \exp \left[ - \left( \frac{\partial \Phi}{\partial \rho_{A^-}} \right)_{\rho_{HA}, T} \right] \quad (2.5a)$$

$$\mu_{HA} = k_B T \ln \left( \frac{\rho_{HA}}{\rho_{0HA}} \right) + \left( \frac{\partial F_{int}}{\partial N_{HA}} \right)_{A_s, N_{A^-}, T} \Rightarrow \rho_{HA} = \rho_{0HA} e^{\beta \mu_{HA}} \exp \left[ - \left( \frac{\partial \Phi}{\partial \rho_{HA}} \right)_{\rho_{A^-}, T} \right] \quad (2.5b)$$

$$\frac{\Delta \pi}{k_B T} = -\beta \left( \frac{\partial F_{int}}{\partial A_s} \right)_{N_{A^-}, N_{HA}, T} = -\Phi + \rho_{A^-} \left( \frac{\partial \Phi}{\partial \rho_{A^-}} \right)_{\rho_{HA}, T} + \rho_{HA} \left( \frac{\partial \Phi}{\partial \rho_{HA}} \right)_{\rho_{A^-}, T} \quad (2.6)$$

$\rho_{0A^-}, \rho_{0HA}$  are density parameters related to the molecular partition functions<sup>101</sup> for a single isolated molecule of each type. Physically, the density parameters are measures of the ideal solubility in the absence of interactions. At low pH, the number density of the unionized molecules  $\rho_{0HA}$  is called the intrinsic solubility under ideal conditions. In absence of interactions, the solubility of weak acids is commonly described using the Henderson-Hasselbalch relation. When cooperative interactions are present, deviations from the ideal HH behavior are expected and the number densities are obtained by solving Eq. 2.5a and 2.5b. For fixed values of the chemical potentials at a particular pH, Eq. 2.5 are coupled nonlinear equations in the unknown densities  $\rho_{A^-}, \rho_{HA}$ , and Eq. 2.6 is the measured excess pressure term arising from interactions in the equation of state of a non-ideal gas mixture. In the absence of the cooperative interaction  $\Phi = 0$ , in the exponential terms, the pre-factors are proportional to the mole fractions obtained in the Henderson-Hasselbalch relations, which leads to the following approximate equations suitable for fitting to the data (Supporting Information),

$$\rho_{A^-} = \frac{1}{1+10^{\text{pK}-\text{pH}}} \rho_{0A^-} e^{-(\partial \Phi / \partial \rho_{A^-})_{\rho_{HA}, T}}, \quad \rho_{HA} = \frac{10^{\text{pK}-\text{pH}}}{1+10^{\text{pK}-\text{pH}}} \rho_{0HA} e^{-(\partial \Phi / \partial \rho_{HA})_{\rho_{A^-}, T}} \quad (2.7)$$

An approximate lower order analysis is used here for fitting the observed data. Details of the full numerical solutions of the coupled nonlinear equations and the existence of

singular points will be presented elsewhere (Narayan and Erramilli, in preparation). Incorporating just a constant second order virial coefficient term  $\Psi_{A-HA}$  adapted from Ben Amotz and Widom does produce the enhanced density in the anomalous region, but the anomalous peak in the observed data is both sharper and narrower, requiring consideration of higher order terms in the virial expansion.

In considering higher order terms, some care must be taken to find a suitable expansion parameter for the following reason. Virial expansions in Eq. 2.4 use the density as the small parameter. In the observed anomalous region with cooperative interactions that enhance number density by a factor of 3 or more, such an expansion in the density is difficult to justify. A clever solution to this problem was first proposed in classic Redlich-Kister<sup>86</sup> (RK) mixing models of non-ideal systems, where the small expansion parameter is the *difference* in the number densities,  $\rho_{A^-} - \rho_{HA}$  which is reasonably expected to be small near pK. A similar expansion using the difference was also exploited by Andelman et al.<sup>88-90</sup>

$$\Psi_{A-HA}(\rho_{A^-}, \rho_{HA}) = \Psi_0 + \Psi_1(\rho_{A^-} - \rho_{HA}) + \Psi_2(\rho_{A^-} - \rho_{HA})^2 + \dots \quad (2.8)$$

At the two extreme pH ranges, when the difference in number densities gets large, the pre-factor  $\rho_{A^-}\rho_{HA}$  in Eq(4) ensures that the excess free energy is negligible, because  $\rho_{A^-}$  is small at low pH, and  $\rho_{HA}$  is small at high pH. *Thus Eq. 2.8 may in fact be used with confidence over the entire pH range in fitting data to a good approximation.* We have adapted Redlich-Kister models of the Gibbs free energy expansion commonly used to describe constant pressure experiments to constant “volume” (i.e. area in 2D systems) ensembles for our surface experiments following the procedures in Ben-Amotz and

Widom.<sup>101</sup> The Redlich-Kister form in Eq. 2.8 is physically intuitive and captures the main aspect of a cooperative interaction describe: this cooperative term is significant only where there are both  $pMBA$  and  $pMBA^-$  present on the surface in significant densities, i.e, when both  $\rho_{A^-}$  and  $\rho_{HA}$  differ significantly from zero. This situation will occur only over a narrow pH range near the putative pK value.

The data in **Figure 2.3b** and **2.3d** when individually fit yielded estimates of the virial coefficients that were consistent with the parameters for surface pressure isotherms. **Figure 2.2**, **Figure 2.3b**, and **Figure 2.3d** all showed enhanced deviations from the HH model consistent with an increase in the number of molecules at the surface near the putative surface  $pK_a$ . To fit the SFG data over the entire pH range in addition to the thermodynamic analysis of the number density, orientational effects also needed to be considered. In principle the mixing free energy can also be determined by calorimetric measurements of the mixing enthalpy. Such calorimetric measurements are exceedingly challenging at 2D interfaces. Surface pressure isotherms (**Fig. 2.2**) which directly measure the changes in the Landau potential may be the best available experimental method for measuring mixing interaction energy as a function of pH.

We also point out some shortcomings of this simplified thermodynamic model of the cooperative interaction applied to analysis of number density on surfaces. The formation of multiple layers at high densities is neglected. The analysis also neglects any significant solvent reorganization energy. Mean Field analysis neglects fluctuations in both the density and molecular orientation. Perhaps the most interesting consequence of the inclusion of higher order terms is that they can lead to qualitatively different *critical*

*behavior*, as pointed out by Andelman et al<sup>88</sup> and Eisenthal and co-workers<sup>102-103</sup> who adopted a Landau-Ginzburg mean field approach to analyze orientational fluctuations and phase behavior in Langmuir-Blodgett films in the canonical ensemble. More sophisticated approaches for modeling the interaction energy lead to predictions of novel phases as well as critical phenomena, but this is beyond the scope of our work.

## 2.5 Conclusion

Both macroscopic measurements of surface pressure and molecular level measurements via SFG spectroscopy reveal that anomalous adsorption of *p*MBA is observed at the air-solution interface. The population of *p*MBA and *p*MBA<sup>-</sup> increases at the liquid-air interface in a narrow pH range of ~0.4 units and appears to be responsible for this phenomenon. Since this anomaly exists near the surface pK<sub>a</sub> of *p*-methyl benzoic acid, both *p*MBA and *p*MBA<sup>-</sup> are present at the interface, allowing cooperative adsorption to take place, possibly in the form of hydrogen bonding between the acid and conjugate base forms. This interaction may be more favorable than hydrogen bonding with water because the deprotonated carboxylate group becomes a better hydrogen bond acceptor for the protonated carbonyl group of *p*MBA in the reduced-dimensional spatial regime of the air-water interface. Enhanced adsorption due to this favorable solvation effect results in higher surface pressure and increased SFG intensity in the carbonyl, carboxylate, CH<sub>3</sub>, and benzene-like ring stretching regions at pH 6.3 as observed here.

While we observed this phenomenon with an acid and its own conjugate base, it is possible that this cooperation could also exist between two different acids at a different bulk pH. For example, if an acid, such as stearic acid, with a higher surface pK<sub>a</sub> than

*p*MBA is present at the interface it could be possible to deprotonate all of the *p*MBA into its conjugate base form while the stearic acid remains in the protonated state. This could result in cooperation between the acidic stearic acid and the deprotonated *p*-methyl benzoate at a pH higher than 6.3, approaching biological pH levels and result in enhanced solute density at the interface.

Proposed extensions of this work would explore whether a linear Hammett relation exists at the air-water interface. Surface SFG-based titration on a series of substituted benzoic acids will be used to determine the surface  $pK_a$  in order to compare them to the bulk and gas phase values and evaluate relative acidities in these three environments. Preliminary results have also shown that different substituent groups on benzoic acid, as well as the position of the substituent for a given group, can alter the pH where the cooperation between the acid and its conjugate base takes place. Being able to manipulate the pH where such enhanced sequestration to an interface results from this proposed surface solvation cooperativity effect could offer some impact on the use of therapeutics, such as inhalant drugs, that are absorbed by alveoli in the lungs by exploiting pH dependent adsorptivity effects at interfaces.

Perhaps the most interesting question is in how the cooperative interaction reported here can modify the phase behavior on the surface. Extension of the cooperative interaction to higher order terms can lead to second order transitions and even a critical point. In addition to the formation of novel phase domains, the existence of a critical point remains to be explored, in which second derivatives of the free energy diverge, and interfacial tension and compressibility goes to zero. A still more exotic open question is

whether the negative excess chemical potential can get large enough to drive the total chemical potential close to zero, resulting in a type of classical condensate. Experiments conducted at a fixed temperature are not sufficient to state definitively where there is an underlying critical point. Experimental signatures of a weak first order transition have been reported in Second Harmonic Generation signal experiments by Eisenthal and co-workers, with observation of enhanced noise attributed to orientational fluctuations<sup>102</sup>. An open question is whether such phenomena can be observed using SFG in acid-base equilibria.

## 2.6 Supporting Information

### 2.6.1 Fitting of SFG spectra

As previously described<sup>43, 104</sup>, the intensity of the sum-frequency generation signal,  $I_{SFG}$ , can be expressed as

$$I_{SFG} \propto \left| \chi_{NR}^{(2)} + \sum_q \chi_q^{(2)} \right|^2 I_{800} I_{IR} \quad (S2.1)$$

where  $I_{800}$  and  $I_{IR}$  are the intensities of the incident 800 nm and IR beams.  $\chi_{NR}^{(2)}$  and  $\chi_q^{(2)}$  are the complex second order susceptibilities of the non-resonant background and the vibrationally resonant sum-frequency term, respectively. The resonant term,  $\chi_q^{(2)}$ , can be expressed as<sup>105</sup>

$$\chi_q^{(2)} \propto \frac{A_q}{\omega_{IR} - \omega_q + i\Gamma_q} \quad (S2.2)$$

where  $\omega_{IR}$  is the frequency of the incident IR beam.  $A_q$ ,  $\omega_q$ , and  $\Gamma_q$  are the amplitude, the frequency and the line width of the vibrational transition. The amplitude,  $A_q$ , is nonzero only if both the Raman and IR transitions are allowed. Therefore, the resonant term

dominates the intensity of the SFG signal when  $\omega_{IR}$  is resonant with a vibrational mode that is both Raman and IR active. SFG spectra are fitted with Eq. S2.1 to obtain all the parameters, and we have plotted the amplitude,  $A_q$ , for the carbonyl and carboxylate ( $ss$ ) modes. This represents the oscillator strength of the band and is proportional to the number density at the air-water interface.

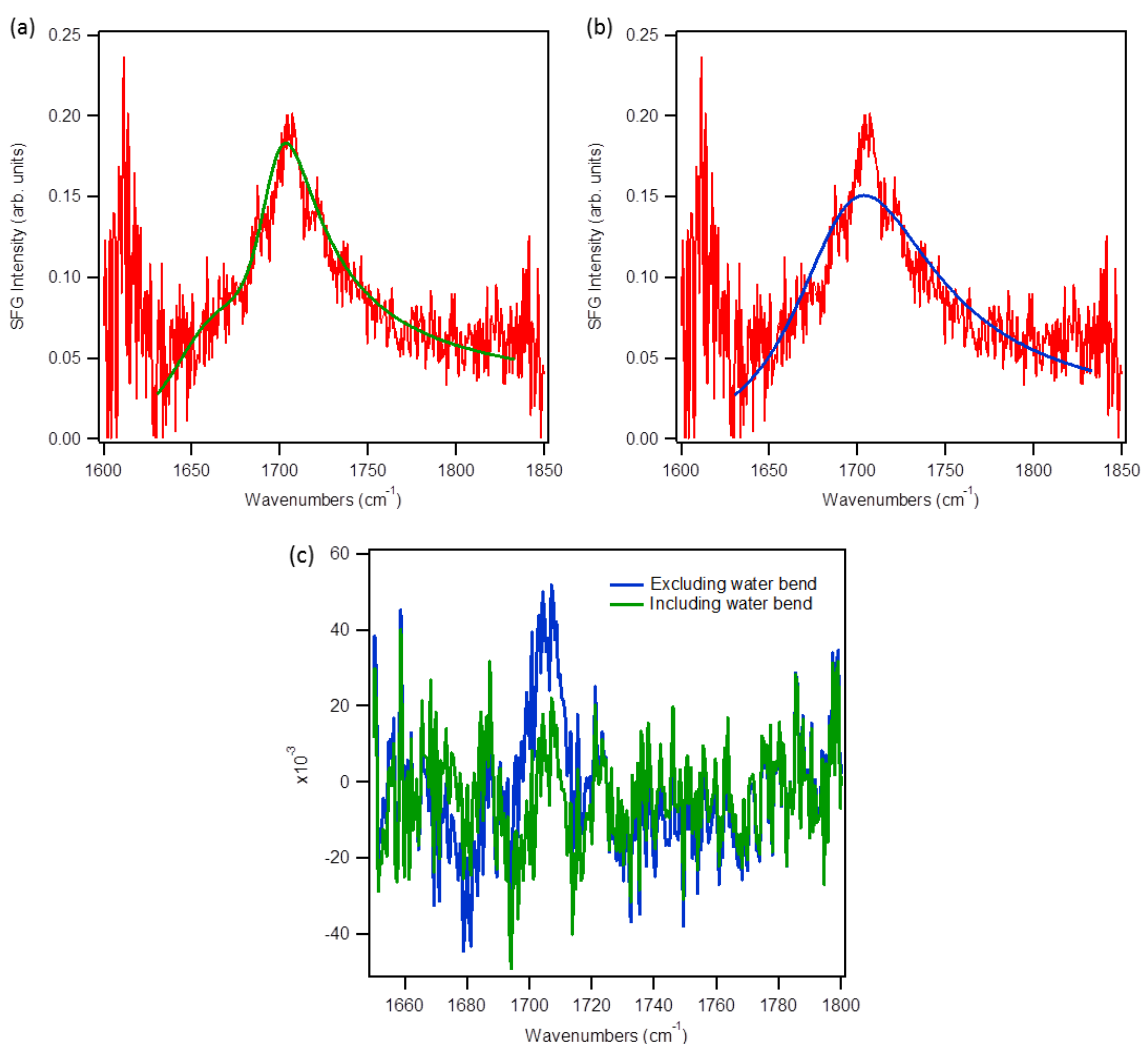


**Figure S2.1: Fitting of pH 1.9 *p*MBA SFG spectrum in the carbonyl stretching region. The fitting in (a) includes the contribution from the water bending mode (solid green line), while the fitting in (b) does not account for resonant contributions from the water bending mode. (c) Residuals for the fits shown in (a) and (b).**

### 2.6.2 Orientation determination of *p*-methyl benzoic acid and *p*-methyl benzoate

The intensity of the SFG signal,  $I_{SFG}$  is given by

$$I_{SFG} \propto \left| \chi_{eff}^{(2)} \right|^2 I_{800} I_{IR} \quad (S2.3)$$

where  $I_{800}$  and  $I_{IR}$  are the intensities of the incident 800 nm and IR beams, respectively.

The effective second order susceptibility,  $\chi_{eff}^{(2)}$ , is defined further below and is proportional to the macroscopic second order susceptibility,

$$\chi_{ijk}^{(2)} \chi_{ijk}^{(2)} = N_s \sum_{i'j'k'} \langle R_{ii'} R_{jj'} R_{kk'} \rangle \beta_{i'j'k'}^{(2)} \quad (S2.4)$$

where  $N_s$  is the surface number density of vibrational species,  $\beta_{i'j'k'}^{(2)}$  represents the microscopic hyperpolarizability elements in the molecular fixed ( $i'j'k'$ ) frame, and  $R_{\lambda\lambda'}$  are the elements of the Euler rotational transformation matrix to the space fixed ( $ijk$ ) frame.

The effective second order susceptibility,  $\chi_{eff}^{(2)}$ , differs from the macroscopic susceptibility, as it accounts for geometric factors, refractive indices, and the reflection of  $s$  and  $p$  polarized beams. For a rotationally isotropic surface of  $C_{\infty v}$  symmetry the effective sum frequency susceptibility,  $\chi_{eff}^{(2)}$ , for  $ppp$  and  $ssp$  polarizations can be written as

$$\chi_{eff,ssp}^{(2)} = L_{yy}(\omega_{SFG}) L_{yy}(\omega_{vis}) L_{zz}(\omega_{IR}) \sin \theta_{IR} \chi_{yyz}^{(2)}$$

$$\chi_{eff,ppp}^{(2)} = -L_{xx}(\omega_{SFG}) L_{xx}(\omega_{vis}) L_{zz}(\omega_{IR}) \cos \theta_{SFG} \cos \theta_{vis} \sin \theta_{IR} \chi_{xxz}^{(2)}$$

$$-L_{xx}(\omega_{SFG}) L_{zz}(\omega_{vis}) L_{xx}(\omega_{IR}) \cos \theta_{SFG} \sin \theta_{vis} \cos \theta_{IR} \chi_{zxx}^{(2)}$$

$$+L_{zz}(\omega_{SFG}) L_{xx}(\omega_{vis}) L_{xx}(\omega_{IR}) \sin \theta_{SFG} \cos \theta_{vis} \cos \theta_{IR} \chi_{zzx}^{(2)}$$

$$+L_{zz}(\omega_{\text{SFG}})L_{zz}(\omega_{\text{vis}})L_{zz}(\omega_{\text{IR}}) \sin \theta_{\text{SFG}} \sin \theta_{\text{vis}} \sin \theta_{\text{IR}} \chi_{zzz}^{(2)}. \quad (\text{S2.5})$$

where  $\theta$  is the reflected angle of each beam with respect to the surface normal. In the laboratory coordinates  $\lambda(x,y,z)$ , all optical beams propagate in the  $xz$  plane perpendicular to the surface ( $xy$  plane), where  $z$  is the direction of the surface normal.  $L_{ii}(\omega)$  is the diagonal element of the Fresnel factor at frequency  $\omega$  (where  $\omega = \omega_{\text{SFG}}, \omega_{\text{vis}},$  or  $\omega_{\text{IR}}$ ) defined by

$$\begin{aligned} L_{xx}(\omega) &= \frac{2n_1(\omega) \cos \gamma}{n_1(\omega) \cos \gamma + n_2(\omega) \cos \theta} \\ L_{yy}(\omega) &= \frac{2n_1(\omega) \cos \theta}{n_1(\omega) \cos \theta + n_2(\omega) \cos \gamma} \\ L_{zz}(\omega) &= \frac{2n_1(\omega) \cos \theta}{n_1(\omega) \cos \gamma + n_2(\omega) \cos \theta} \left( \frac{n_1(\omega)}{n'(\omega)} \right)^2 \end{aligned} \quad (\text{S2.6})$$

where  $n_1(\omega)$ ,  $n_2(\omega)$ , and  $n'(\omega)$  are the refractive index of air, water, and the interface (the average of  $n_1$  and  $n_2$ ), respectively, at frequency  $\omega$ , and  $\gamma$  is the refracted angle for each beam.

Given the  $C_{2v}$  symmetry of  $p\text{MBA}$ , there are 3 nonzero microscopic hyperpolarizability elements for the  $v_{8a}$  ring stretching mode ( $\beta_{x'x'z'}^{(2)}$ ,  $\beta_{y'y'z'}^{(2)}$ , and  $\beta_{z'z'z'}^{(2)}$ ).<sup>96</sup> As a result, the second order susceptibilities  $\chi_{zzz}^{(2)}$ ,  $\chi_{xxz}^{(2)}$ ,  $\chi_{zxx}^{(2)}$ , and  $\chi_{xxz}^{(2)}$  can be reduced to

$$\begin{aligned} \chi_{zzz}^{(2)} &= \frac{1}{2} N_s \beta_{z'z'z'}^{(2)} \{ \langle \cos^3 \theta_t \rangle + R \langle \sin^2 \theta_t \cos \theta_t \sin^2 \psi \rangle + R' \langle \sin^2 \theta_t \cos \theta_t \cos^2 \psi \rangle \} \\ \chi_{xxz}^{(2)} &= \frac{1}{2} N_s \langle \cos \theta_t \rangle \beta_{z'z'z'}^{(2)} \{ \langle \sin^2 \theta_t \rangle + (R + R') - R \langle \sin^2 \theta_t \sin^2 \psi \rangle \\ &\quad - R' \langle \sin^2 \theta_t \cos^2 \psi \rangle \} \end{aligned}$$

$$\chi_{xzx}^{(2)} = \chi_{zxx}^{(2)} = \frac{1}{2} N_s \langle \sin^2 \theta_t \cos \theta_t \rangle \beta_{z'z'z'}^{(2)} \{1 - R \langle \sin^2 \psi \rangle - R' \langle \cos^2 \psi \rangle\} \quad (\text{S2.7})$$

where  $\theta_t$  is the tilt angle of the IR transition dipole for the  $\nu_{8a}$  ring stretching mode relative to the surface normal,  $\psi$  is the twist angle defined by the rotation of the benzene ring around the vibrational transition moment, and  $R$  and  $R'$  are the ratios,  $R = \beta_{y'y'z'}^{(2)} / \beta_{z'z'z'}^{(2)}$  and  $R' = \beta_{x'x'z'}^{(2)} / \beta_{z'z'z'}^{(2)}$  calculated by Gaussian 09 using B3LYP/6-311+G level density functional theory (DFT).

**Table S2.1: Gaussian Calculated Hyperpolarizabilities Values**

$\beta_{y'y'z'}^{(2)}$	$-2.67 \times 10^{-51}$
$\beta_{x'x'z'}^{(2)}$	$2.57 \times 10^{-52}$
$\beta_{z'z'z'}^{(2)}$	$-1.47 \times 10^{-50}$

Hyperpolarizability values reported in units  $\text{C}^3 \text{m}^3 \text{J}^{-2}$

Substituting the above expressions into Eq. (B3) yields the effective second order susceptibility as a function of the tilt and twist angle,  $\theta_t$  and  $\psi$ , respectively. Plotting the square of Eq. (S2.5) as a function of  $\theta$  for *ssp* and *ppp* polarization generates the plot shown in **Figure 2.6** of the Discussion section above

### 2.6.3 SFG spectra of $\text{CH}_3$ (*ss* and *as*) of *p*-methyl benzoic acid in *ssp* and *ppp* polarization configuration

The  $2950 \text{ cm}^{-1}$  band in the SFG spectra corresponds to the  $\text{CH}_3$  asymmetric stretching mode and is shown for the *ssp* and *ppp* polarization conditions in **Figures S2.2a** and **S2.2b**, respectively. In acidic conditions, the peak intensity of the  $\text{CH}_3$  (*as*) is relatively weak compared to the  $\text{CH}_3$  (*as*) in basic conditions and at pH 6.3. When looking at the SFG spectra in *ppp* polarization in **Figure S2.2b**, the peak intensity of the  $\text{CH}_3$  (*as*) is lowest in acidic conditions, but nearly the same in the two higher pH

solutions. Thus, we observe that the *ppp*:*ssp* peak intensity ratio changes with pH, indicating a change in orientation of *p*-methyl benzoic acid at the interface.<sup>40</sup> A similar trend is seen in the COO<sup>-</sup> (*ss*) of *p*-methyl benzoate (*pMBA*<sup>-</sup>), the conjugate base of *p*-methyl benzoic acid. In *ssp* polarization configuration, the COO<sup>-</sup> (*ss*) SFG intensity is high and nearly the same for solutions of pH 6.4, 7.3, and 12.1. However, in the *ppp* configuration the COO<sup>-</sup> (*ss*) SFG intensity is lowered by nearly half at pH 6.4 when compared to pH 7.3 and 12.1. The change in the *ppp*:*ssp* SFG intensity ratio at pH 6.4 indicates a change in orientation of the *p*-methyl benzoate species<sup>40</sup>, attributed to complexation with the protonated *pMBA* molecules.

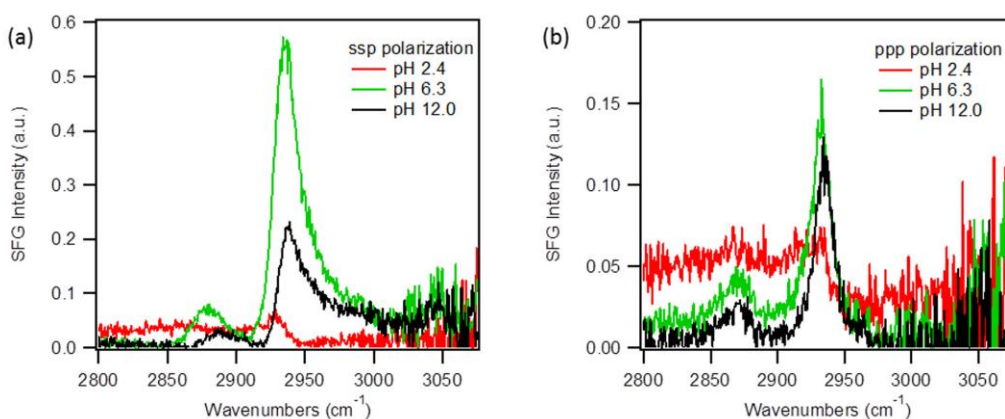


**Figure S2.2:** (a) SFG spectra of CH<sub>3</sub> (*ss* and *as*) of *p*-methyl benzoic acid in *ssp* polarization. (b) SFG spectra of CH<sub>3</sub> (*ss* and *as*) of *p*-methyl benzoic acid in *ppp* polarization. The ratio of *ppp*:*ssp* intensity changes with pH, which indicates a change in the orientation of *p*-methyl benzoic acid at the interface.

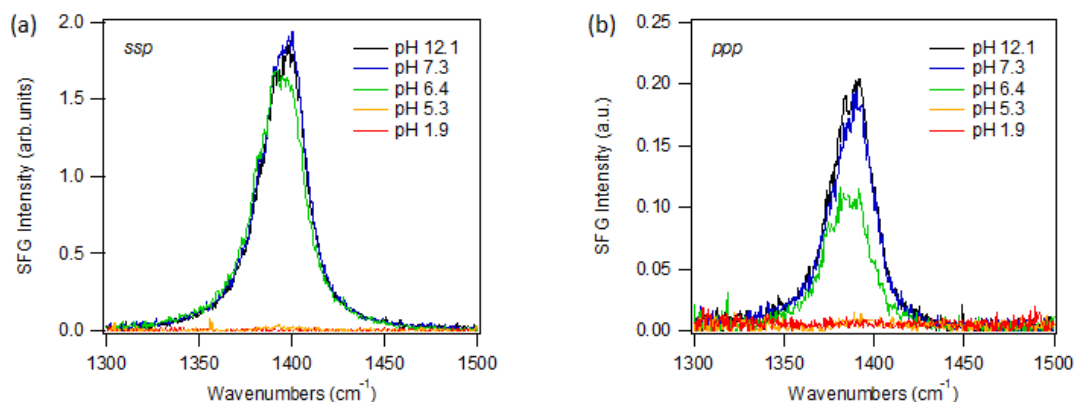


**Figure S2.3: (a) SFG spectra of COO<sup>-</sup> (*ss*) of *p*-methyl benzoate in *ssp* polarization combination. (b) SFG spectra of COO<sup>-</sup> (*ss*) in *ppp* polarization combination. The *ppp*:*ssp* intensity ratio changes at pH 6.4, indicating a change in orientation of the *p*-methyl benzoate species at the air-water interface. A COO<sup>-</sup> (*ss*) SFG peak is not observed below pH 5.3 since most of the molecules are in the protonated, -COOH, form.**

**Figure S2.4** (below) shows the bulk titration of 1 mM *p*MBA with NaOH. In contrast to the SFG surface-selective titration, the bulk titration shows a monotonic increase in pH as more NaOH is added. Also, no anomalous features are present at pH 6.3, as observed by SFG spectroscopy and surface pressure measurements. The experimentally determined bulk pK<sub>a</sub> is also lower (by ~1.5 pH units) than when measured by SFG.

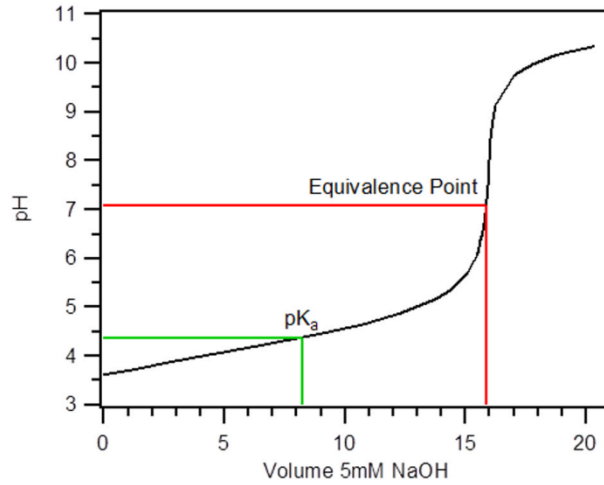


**Figure S2.4: Titration of 1 mM pMBA with 5 mM NaOH. The equivalence point, indicated by the red lines, occurs near pH 7.1 when approximately 16 mL of NaOH is added. The observed bulk  $pK_a$  is at pH 4.4, indicated by the green lines.**

#### 2.6.4 Cooperative interactions and the Virial expansion

The Helmholtz Free energy for a given fixed area  $A_s$  is expanded in terms of the number densities of the two species  $\rho_A = N_A/A_s$  and  $\rho_{HA} = N_{HA}/A_s$  with the total number density  $\rho \equiv \rho_A + \rho_{HA} = N/A_s$ . As described in the main text, [A] stands for acid and [HA] represents the protonated form. The mole fractions are  $x_A = \frac{N_A}{N}$  and  $x_{HA} = \frac{N_{HA}}{N}$  where  $N$  is the total number of A and HA molecules on the surface. The Free energy  $F$  is extensive and can be written as

$$F = F_{ideal} + F_{int} = N_A k_B T \ln \rho_A + N_{HA} k_B T \ln \rho_{HA} + A_s k_B T \Phi(\rho_A, \rho_{HA}) \quad (S2.8)$$

where  $\Phi(\rho_A, \rho_{HA})$  is the (intensive) interaction term. Explicit contributions from water molecules are omitted in this bimolecular description approximation. Water molecules can play a crucial role in modulating the interactions and will determine the parameters in the interaction term  $\Phi(\rho_A, \rho_{HA})$ .

The surface pressure and chemical potentials are given by

$$\pi = -\left(\frac{\partial F}{\partial A_s}\right)_{N_A, N_{HA}, T} = \rho k_B T + k_B T \left[ -\Phi + \rho_A \left(\frac{\partial \Phi}{\partial \rho_A}\right)_{\rho_{HA}} + \rho_{HA} \left(\frac{\partial \Phi}{\partial \rho_{HA}}\right)_{\rho_A} \right] \quad (\text{S2.9})$$

$$\mu_A = \left(\frac{\partial F}{\partial N_A}\right)_{A_s, N_{HA}, T} = k_B T \ln\left(\frac{\rho_A}{\rho_{0A}}\right) + k_B T \left(\frac{\partial \Phi}{\partial \rho_A}\right)_{\rho_{HA}, T} \quad (\text{S2.10})$$

$$\mu_{HA} = \left(\frac{\partial F}{\partial N_{HA}}\right)_{A_s, N_A, T} = k_B T \ln\left(\frac{\rho_{HA}}{\rho_{0HA}}\right) + k_B T \left(\frac{\partial \Phi}{\partial \rho_{HA}}\right)_{\rho_A, T} \quad (\text{S2.11})$$

In mean field theory, the bimolecular interaction term per unit area in units of  $k_B T$  is of the form

$$\frac{1}{A_s k_B T} F_{int} = \Phi(\rho_A, \rho_{HA}) = \rho_A^2 \Psi_A + \rho_{HA}^2 \Psi_{HA} + 2\rho_A \rho_{HA} \Psi_{AHA} + \dots \quad (\text{S2.12})$$

The coefficient terms  $\Psi_{ij}$  are in general functions of the densities, with the third representing mixing. In the lowest order virial expansion, the coefficients are constants and

$$\pi = -(\partial F / \partial A_s)_{N_A, N_{HA}, T} = \rho k_B T + \rho^2 k_B T B + \dots \quad (\text{S2.13})$$

where the second virial coefficient is more conventionally written in terms of the mole-fractions, rather than the number densities, following Ben-Amotz and Widom<sup>99</sup>:

$$B = \rho_A^2 x_A + \rho_{HA}^2 x_{HA} + 2x_A x_{HA} \Psi_{AHA} \quad (\text{S2.14})$$

In the Gibbs ensemble, the expansion is in terms of the mole fractions instead of the densities, but leads to the same equation of state.

In Redlich-Kister models, the mixing term is expanded in the form and are used to fit the data as described in the main text. This provides a connection between the Gibbs ensemble commonly used in multi-component systems and the Grand Canonical ensemble and associated Landau potential.

$$\Psi_{AHA}(\rho_A, \rho_{HA}) = \Psi_0 + \Psi_1(\rho_A - \rho_{HA}) + \Psi_2(\rho_A - \rho_{HA})^2 + \dots$$

As described in the main text, an advantage of the Redlich-Kister form is that it provides a physically intuitive description of cooperative interactions.

## CHAPTER 3. Determination of Short-Chain Carboxylic Acid Surface $pK_a$ via Surface Tension and Vibrational Sum-Frequency Generation Spectroscopy

### 3.1 Introduction

The air-water interface gives rise to unique chemical, physical, and biological properties due to its inherent asymmetry, reduced dimensionality, and low dielectric permittivity.<sup>36, 106-107</sup> Changes in the local environment can have an effect on the acidity of molecules, thus the surface  $pK_a$  of organic acids is different from the bulk solution  $pK_a$ .<sup>69, 108-110</sup> Understanding the changes in the local solvation environment at the surface and its effect on the  $pK_a$  is important, since acidic and basic aqueous solutions play a key role in environmental and atmospheric chemistry.<sup>7, 48-51</sup> Furthermore, atmospheric aerosols have been shown to possess organic compounds such as *n*-alkanes, alkanols, and carboxylic acids.<sup>51, 111-113</sup>

An ideal technique to study acids at the air-water interface is vibrational sum-frequency generation (SFG) spectroscopy.<sup>17-18, 63, 65-66</sup> SFG is a second order, non-linear optical phenomenon that is forbidden in media with inversion symmetry and selectively probes molecules at the air-water interface.<sup>35, 114</sup> Recently, SFG spectroscopy has been used as a surface titration method to determine the interfacial  $pK_a$  of *L*-alanine and *L*-proline at the air-water interface by measuring the intensities of the carboxylic acid group (protonated) and carboxylate anion group (ionized) over a wide range of pH values.<sup>115</sup> It was determined that the surface  $pK_a$  of *L*-alanine and *L*-proline are greater than the bulk solution  $pK_a$  by 0.3 and 0.8 pH units, respectively. This is attributed to the decreased solvation interactions at the surface of the negatively charged carboxylate group, thus

making it less stable and requiring a higher bulk pH to induce the deprotonation of the carboxylic acid group.<sup>115</sup>

Measuring increased surface  $pK_a$  values relative to bulk  $pK_a$  values is not uncommon, as previous studies of long-chain fatty acids at the interface found that the surface  $pK_a$  is greater than the  $pK_a$  observed in bulk solution, and the surface  $pK_a$  increases with increasing carbon chain length.<sup>71, 73-74, 116</sup> Long-chain fatty acids are of particular interest due to the role they play in surface adsorption in the alveoli and their potential impact for controlling therapeutic effects in lungs and related tissues.<sup>4, 68</sup> The increase in surface  $pK_a$  of long-chain fatty acids relative to the bulk value is attributed to an increased surface proton concentration effects described above<sup>63</sup>, while the trend of increasing surface  $pK_a$  with increasing carbon chain length is explained by stronger van der Waals interactions between the hydrophobic tails. Due to increased intramolecular interactions, the molecules are brought closer together and shield the acidic hydrogen atom and thus increasing the surface  $pK_a$ .<sup>71, 75</sup>

Surface tension measurements have also been a tool for determining the  $pK_a$  values of acids. The first surface tension  $pK_a$  study was reported in 2015 by Dickhaus and Priefer.<sup>117</sup> Polyelectrolyte solutions were titrated and surface tension was measured using a surface tensiometer. Plots of surface tension as a function of pH yielded sigmoidal curves, and the  $pK_a$  was determined by the inflection point. It was shown that the surface tension, and consequently the surface  $pK_a$ , of the polyelectrolytes varied with both polymer and salt concentrations.<sup>117</sup> Following this study, recent work by Allen et al. also used surface tension to measure the surface  $pK_a$  of medium-chain ( $C_8$ - $C_{10}$ ) fatty acids at

the air-water interface.<sup>118</sup> The surface tension plots as a function of pH also produced sigmoidal curve, however an anomalous dip in surface tension near the experimentally determined  $pK_a$  was also reported. The anomalous dip in surface tension is attributed to the formation of an acid-soap complex between the acid and its conjugate base that occurs due to favorable interactions in the hydrophobic tails of the fatty acids.<sup>71, 75, 118</sup> The study by Allen et al. determined that the surface  $pK_a$  of octanoic, nonanoic, and decanoic acid was increased relative to the bulk solution  $pK_a$  and the surface  $pK_a$  increased with increasing number of carbons following the order: octanoic acid (4.9) < nonanoic acid (5.8) < decanoic acid (6.4). While there are differences in the surface  $pK_a$  values compared to previous literature studies,<sup>71, 74, 119</sup> attributed to differences between measurement techniques and concentrations, the measurements follow the increasing surface  $pK_a$  trend with increasing number of carbons.

In this study, we use both surface tension measurements and vibrational sum-frequency spectroscopy to determine the surface  $pK_a$  of three short-chain aliphatic acids: acetic acid ( $C_2$ ), propionic acid ( $C_3$ ), and valeric acid ( $C_5$ ). We report the carbonyl ( $C=O$ ) stretching and carboxylate ( $COO^-$ ) symmetric stretching ( $ss$ ) vibrational sum-frequency generation spectra in aqueous solution kept at constant ionic strength as a function of bulk pH. The  $C=O$  and  $COO^-$  ( $ss$ ) SFG peak amplitudes, which are linearly proportional to vibrator number density, were determined over the 2-12 pH range and fit to a modified Henderson-Hasselbalch equation to calculate the surface  $pK_a$ . Surface tension measurements are also reported for the short-chain carboxylic acids and surface tension plots as a function of pH were fit to a surface activity model<sup>118, 120</sup> to determine the  $pK_a$ .

Our results are shown to be consistent between the two methods, as small percent differences (within 5%) are measured. We also report trends in our results that are consistent with previous interfacial  $pK_a$  measurements for medium and long-chain fatty acids. We measure a higher surface  $pK_a$  compared to the bulk value and an increasing  $pK_a$  with increasing carbon chain length. However, the magnitude of increasing  $pK_a$  with carbon chain length is smaller than those for longer chain fatty acids.

### 3.2 Experimental

*Sample Preparation.* Acetic acid, propionic acid, and valeric acid were purchased from Sigma Aldrich and used without further purification. 1M acetic acid and propionic acid solutions were prepared at various pH individually by adding standardized 1M NaOH (Sigma Aldrich) and Millipore water (18.2 M $\Omega$ -cm). Solutions of valeric acid were prepared at a concentration of 250 mM, due to its lower solubility relative to acetic acid and propionic acid. Solid sodium chloride (NaCl,  $\geq 99\%$  Sigma Aldrich) was added to the solutions to maintain constant ionic strength. An Accumet Basic 15+ pH meter was used to determine the pH of these solutions.

*Surface Tension Measurements.* Surface tension was measured using a Langmuir-Blodgett (LB) trough and a Pt Wilhelmy plate (KSV NIMA). For surface tension measurements, the Pt plate and sample dish were plasma cleaned (Harrick Plasma, Model PDC-001) and rinsed with ethanol and Millipore water. N<sub>2</sub> (g) was used to dry the plate prior to each measurement.

*Sum-Frequency Generation (SFG) Spectroscopy.* The previously described broad-band vibrational sum-frequency spectrometer was used to obtain SFG spectra in the carbonyl

stretching region (centered at  $\sim 1725 \text{ cm}^{-1}$ ) and the carboxylate symmetric stretching (*ss*) region (centered at  $\sim 1415 \text{ cm}^{-1}$ ) and normalized relative to the non-vibrational SFG response from a GaAs crystal. The bandwidths of the overlapping visible (800 nm) and IR beams were  $\sim 7 \text{ cm}^{-1}$  and  $200 \text{ cm}^{-1}$ , respectively. Half-wave/polarizer elements determined the relative incident polarizations and the measured signal polarization component was defined by a polarizer in the signal beam path. All SFG spectra for this study were collected in the *ssp* polarization configuration (*s*-polarized SFG, *s*-polarized visible, *p*-polarized IR).

The intensity of the sum-frequency generation signal,  $I_{SFG}$ , can be expressed as<sup>43, 104</sup>

$$I_{SFG} \propto \left| \chi_{NR}^{(2)} + \sum_q \chi_q^{(2)} \right|^2 I_{800} I_{IR} \quad (3.1)$$

where  $I_{800}$  and  $I_{IR}$  are the intensities of the incident 800 nm and IR beams.  $\chi_{NR}^{(2)}$  and  $\chi_q^{(2)}$  are the complex second order susceptibilities of the non-resonant background, which includes contributions from the water resonance<sup>92-93</sup> and the vibrationally resonant sum-frequency term, respectively. The resonant term,  $\chi_q^{(2)}$ , can be expressed as a Lorentzian shaped contribution<sup>105</sup>

$$\chi_q^{(2)} \propto \frac{A_q}{\omega_{IR} - \omega_q + i\Gamma_q} \quad (3.2)$$

where  $\omega_{IR}$  is the frequency of the incident IR beam.  $A_q$ ,  $\omega_q$ , and  $\Gamma_q$  are the amplitude, the frequency and the line width of  $q^{\text{th}}$  the vibrational transition. The amplitude is nonzero only if both the Raman and IR transitions are allowed, therefore the resonant term dominates the intensity of the SFG signal when  $\omega_{IR}$  is resonant with a vibration mode that is Raman and IR active. The observed SFG signals are fit to Eqs. 3.1 and 3.2 to

determine the peak amplitudes of the carbonyl stretching and carboxylate (*ss*) modes as a function of pH. The peak amplitudes are normalized to the lowest (for C=O stretching) and highest (for COO<sup>-</sup> *ss*) pH solutions, at which all of the molecules will be in the protonated or deprotonated state, respectively.

### 3.3 Results and Discussion

#### 3.3.1 Surface Tension Titration of Aliphatic Acids

Traditional surface tension measurements were carried out for the acetic, propionic, and valeric acid in the pH range 1 to 13. The results (**Figure 3.1**) show that the surface tension of each acid exhibits a monotonic decrease as pH decreases.

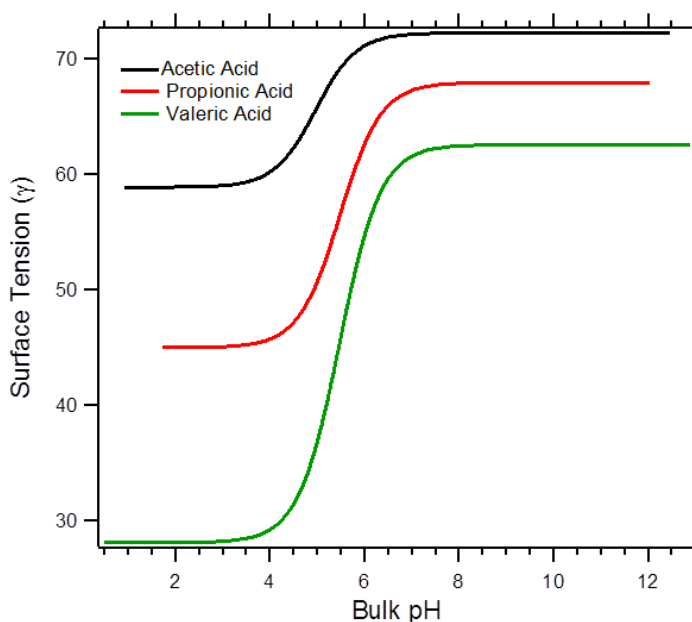


**Figure 3.1:** Surface tension of acetic (black), propionic (red), and valeric (green) acid as a function of bulk pH. The surface tension at high pH values (pH > 9) decreases with increasing number of carbons, due to higher number density of propionic and valeric acid relative to acetic acid. At pH < 3 the difference in surface tension values are greater than that observed at high pH, attributed to greater number density and stronger interactions between the hydrophobic tails with increasing number of carbons.

Differences between the three aliphatic acids in the surface tension measurements are evident as shown in **Figure 3.1**. Across the entire pH range a decrease in surface tension is seen as the carbon chain length increases from acetic acid ( $C_2$ ) to valeric acid ( $C_5$ ). In a first approximation the differences in surface tension are attributed to changes in the surface number density for each deprotonated species. Valeric acid (green curve in **Figure 3.1**), is the most hydrophobic of the three acids, has the longest hydrophobic tail and lowest bulk solubility, and will therefore be the most surface active due to the reduced dielectric constant at the interface.<sup>106-107</sup> Thus, it exhibits the lowest surface tension. **Figure 3.1** also reveals that  $\Delta\gamma_{\max}$  for each acid increases as the carbon chain length increases.  $\Delta\gamma_{\max}$  is defined as the difference in surface tension between the highest and lowest pH solution ( $\Delta\gamma_{\max} = \gamma_{\text{pH } 12} - \gamma_{\text{pH } 2}$ ). The increase in  $\Delta\gamma_{\max}$  can be explained by stronger interactions between the hydrophobic tails as the number of carbons increases.<sup>71, 75, 118</sup>

The surface tension measurement of valeric acid (**Figure 3.1**) reveals a striking difference to that *p*-methyl benzoic acid (*p*MBA), as described in Chapter 2. At high pH the surface tension of the two molecules are comparable. However, at low pH the surface tension of *p*-methyl benzoic acid is ~64 mN/m, whereas the surface tension of valeric acid is ~30 mN/m. The large difference in surface tension can be attributed to the difference in surface number density between the two species, which can be affected by the size and orientation of the molecules. *p*MBA is larger in the sense that it possesses a “bulky” aromatic ring in its hydrophobic region, while the hydrophobic tail of valeric acid is a saturated carbon chain that allows it to better pack at the interface. It has also

been shown that at low pH the protonated form of *p*MBA is tilted by  $\sim 30^\circ$  relative to the surface normal (details provided in Chapter 2), which will hinder it from packing as efficiently as valeric acid at the surface. This contributes to the larger effective calculated area per molecule of *p*-methyl benzoic acid compared to that of valeric acid. In Chapter 2 we showed that the calculated area per molecule for *p*MBA is  $\sim 2.5 \text{ nm}^2$ . This is an order of magnitude greater than the typical area per molecule of long-chain carboxylic acids,  $\sim 0.30 \text{ nm}^2$ . Thus, a higher surface number density of valeric acid compared to *p*MBA is a reasonable expectation, thus resulting in a significantly lower surface tension. At high pH, when the surface tension of *p*MBA and valeric acid are comparable, the change in orientation of *p*MBA with pH must be considered. The deprotonated *p*MBA<sup>-</sup> molecule is oriented nearly vertical to the surface normal, which can allow it to pack more efficiently—possibly also allowing for more energetically favorable  $\pi$ -stacking interactions—leading to a similar surface tension value that is observed with valeric acid,  $\sim 64 \text{ mN/m}$  (**Fig. 3.1**).

To determine the surface  $\text{pK}_a$ , a surface activity model previously described by Cratin<sup>120</sup> and Allen et al.<sup>118</sup> was used to fit the surface tension data as a function of pH:

$$\Delta\gamma = \frac{\Delta\gamma_{\text{max}}}{1+10^{(\text{pH}-\text{pK}_a)}} \quad (3.3)$$

where  $\Delta\gamma = \gamma_{\text{max}} - \gamma$ , and  $\gamma_{\text{max}}$  is the max surface tension measured at high pH. The  $\text{pK}_a$  corresponds to the surface  $\text{pK}_a$  value of the acid. The surface activity model is described in further detail in the Supporting Information. Fits of the surface tension data to Equation 3.3 are shown in **Figure 3.2** as solid lines. The vertical dashed lines in **Figure**

**3.2** represent the experimentally determined value of the surface  $pK_a$  obtained from fitting the model (Eq. 3.3) averaged over at least four trials.

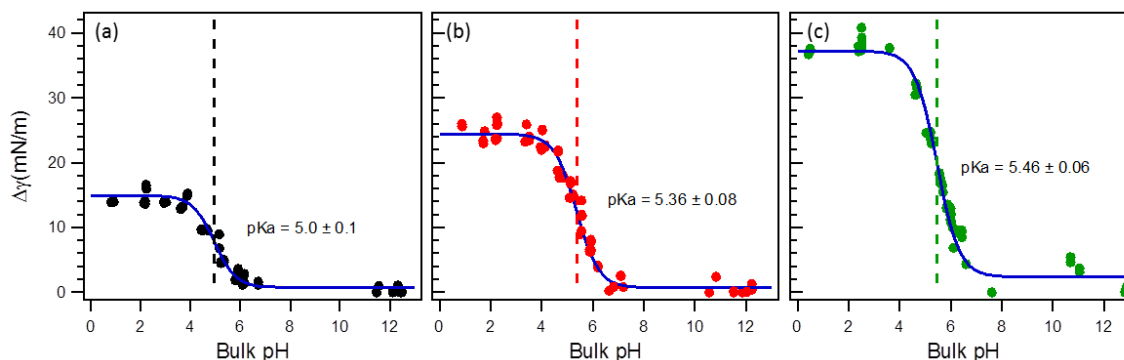


**Figure 3.2:** Surface pressure of (a) acetic acid, (b) propionic acid, and (c) valeric acid as a function of pH. The solid blue line is a fit to the surface activity model, and the dashed lines represent the average surface  $pK_a$  value. A trend of increasing average surface  $pK_a$  with increasing number of carbons is observed.

These results of the fitting are summarized in **Table 3.1** below. Two distinct trends can be seen from the surface  $pK_a$  values: (1) for each acid, surface  $pK_a > \text{bulk } pK_a^{121}$  and (2) as the carbon chain length increases from  $C_2$  to  $C_5$  the experimentally determined surface  $pK_a$  also increases.

**Table 3.1** Surface  $pK_a$  of short-chain acids determined by surface tension and SFG titration

$C_n$	Bulk $pK_a^{121}$	Surface $pK_a$ (Surface Tension)	Surface $pK_a$ (SFG)
$C_2$	4.76	$5.0 \pm 0.1$	$5.08 \pm 0.04$
$C_3$	4.87	$5.36 \pm 0.08$	$5.61 \pm 0.08$
$C_5$	4.83	$5.46 \pm 0.06$	$5.74 \pm 0.14$

The increase in surface  $pK_a$  relative to the bulk  $pK_a$  value can be attributed to the higher surface proton concentration induced by the surface electric field,<sup>19, 69-70</sup> favoring the neutral form of the acid/base pair in comparison to the bulk. The observed increase in surface  $pK_a$  with increasing carbon chain length is owed to increased van der Waals

forces between the longer carbon chains bringing the molecules closer together, packing the carboxylic acid groups and shielding the hydrogen atom. As the shielding increases, the  $pK_a$  increases.<sup>71, 118</sup>

### 3.3.2 *Sum-Frequency Titration of Aliphatic Acids*

Unlike the surface tension measurements discussed above, the sum-frequency titration method provides molecular level details of the protonated and deprotonated forms of the aliphatic acids by independently probing the carbonyl (C=O) stretching and carboxylate (COO<sup>-</sup>) symmetric stretching regions. To spectroscopically determine the surface  $pK_a$ , measurements of the SFG intensities of the carbonyl and carboxylate vibrations were collected for the three short-chain acids and their respective conjugate bases as a function of pH. The pH-dependent SFG spectra for acetic, propionic, and valeric acid, along with their conjugate bases, are shown in **Figure 3.3**. The SFG spectrum for each acid due to resonance with the protonated carbonyl stretch (**Fig. 3.3 a-c**) at  $\sim 1725\text{ cm}^{-1}$  shows a monotonic decrease as pH increases from 2 to 12. The same monotonic behavior is exhibited in the SFG intensities of the carboxylate (*ss*) region at  $\sim 1415\text{ cm}^{-1}$  (**Fig. 3.3 d-f**). The decrease in the COO<sup>-</sup> (*ss*) intensities occurs as pH decreases from 12 to 2.

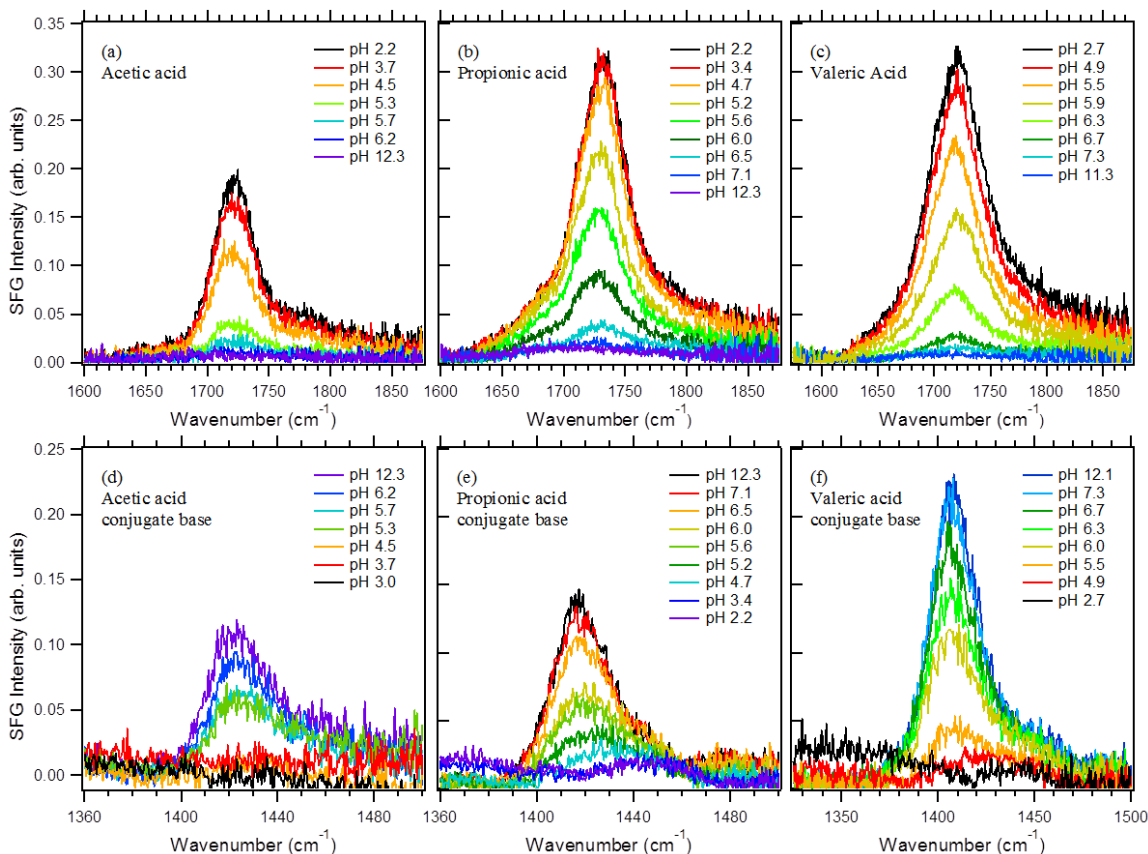


**Figure 3.3: Vibrational sum-frequency generation spectra for acetic, propionic, and valeric acid in the (a-c) carbonyl stretching region, centered at  $\sim 1725\text{ cm}^{-1}$ , and the carboxylate (*ss*) region, centered at  $\sim 1415\text{ cm}^{-1}$  (d-f).**

Previous studies<sup>55, 71, 75</sup> have shown that, due to van der Waals interactions, long-chain carboxylic acids can form surface active acid-soap complexes at a pH near the surface  $pK_a$ , evidenced by a dip in the surface tension as a function of pH.<sup>118</sup> *p*-methyl benzoic acid has also been shown to exhibit this dip in surface tension at the air-water interface. In addition to this, the carbonyl stretching and carboxylate (*ss*) SFG intensities show an anomalous increase in the region where the dip in surface tension occurs, near its observed surface  $pK_a$  (see Chapter 2, **Figure 2.3**). However, these shorter chain acids show no evidence of acid-soap complexation in their SFG spectra, i.e. no anomalous increase in SFG intensity is observed in **Figure 3.3** and no dip is observed in the surface

tension measurements (**Fig. 3.1**). The absence of acid-soap complexation in these short-chain aliphatic acids is attributed to the differences in  $\text{Na}^+$  ion concentration between the two studies. In the current study, NaCl was added to all aliphatic acid solutions to maintain a constant ion concentration of 1M  $\text{Na}^+$ , whereas the  $\text{Na}^+$  concentration in the *p*MBA system was  $\sim 8$  mM. It has been shown that at high  $\text{Na}^+$  ion concentration the hydrogen bonding network between protonated and deprotonated fatty acids is disrupted due to the ionic binding affinity between the deprotonated carboxylate group and the  $\text{Na}^+$  ion.<sup>65, 118</sup> Thus, the change in the hydrogen bonding network could prevent the formation of the acid-soap complex. This is supported by the study of Allen et al. in which no dip in  $\text{C}_8$ - $\text{C}_{10}$  surface tension titrations was observed for high  $\text{Na}^+$  concentration solutions.<sup>118</sup>

In order to calculate the surface  $\text{pK}_a$  from the SFG spectra, the peak amplitude,  $A_q$ , was determined by fitting the SFG spectra to Eqs. 3.1 and 3.2. The peak amplitude is used because it is directly proportional to the surface number density ( $\rho$ )—assuming the orientation of the acid and its conjugate base remains unchanged—whereas the SFG intensity is proportional to the square of the surface number density (see Chapter 1, Eqs. 1.1 and 1.6). In this fitting procedure, all center frequencies and widths were kept fixed, while the peak amplitude and non-resonant contributions fitting parameters. **Figure 3.4a** and **3.4b** show the normalized SFG peak amplitude plots for the carbonyl and carboxylate (*ss*) vibrations as a function of pH for each acid. The solid lines in **Figure 3.4** are fits to a Henderson-Hasselbalch (HH) model for the surface number density, following the form:

$$\rho_{\text{HA}} = A_{\text{max}}^{1725} \frac{1}{1+10^{(\text{pH}-\text{pK}_a)}} + C \text{ and } \rho_{\text{A}^-} = A_{\text{max}}^{1415} \frac{10^{(\text{pH}-\text{pK}_a)}}{1+10^{(\text{pH}-\text{pK}_a)}} + C \quad (3.4)$$

where  $A_{\max}^{1725}$  and  $A_{\max}^{1415}$  are the fitted peak amplitudes for the lowest and highest pH solutions, respectively. A derivation of Eq. 3.4 is provided in the Supporting Information. This model assumes that the changes in SFG peak amplitude are due only to changes in the surface number density of the protonated form and deprotonated form of each acid, ignoring the contributions from orientation changes and other ions present in solution. This is justified, as the ionic strength of all solutions is kept constant by the addition of NaCl, thus preventing the acid-soap complexation due to high  $\text{Na}^+$  ion concentrations.<sup>65,</sup>  
<sup>118</sup> Plots of the average HH fitted peak amplitude as a function of pH for acetic, propionic, and valeric acid—black, red, and green lines, respectively—and their respective conjugate base are shown in **Figure 3.4**.

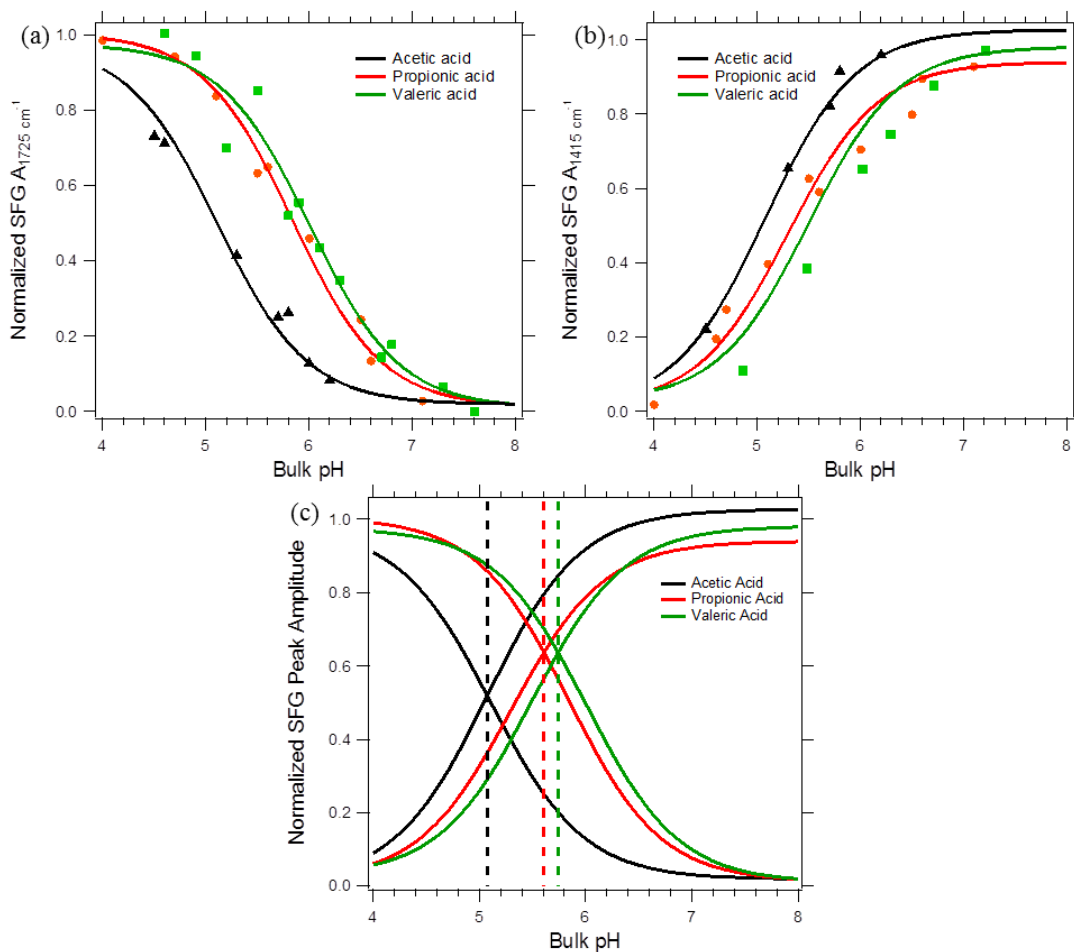


**Figure 3.4:** Plot of the (a) carbonyl and (b) carboxylate (*ss*) peak amplitude for acetic (black), propionic (red), and valeric acid (green). Peak amplitudes were determined by fitting the SFG spectra (Fig. 3.3) to Eqs. 3.1 and 3.2. The solid lines represent fits of the peak amplitude as a function of pH to a HH model (Eq. 3.4). The dashed lines in (c) represent the point where  $\rho_{\text{HA}} = \rho_{\text{A}^-}$  for each acid. We define this point as the surface  $\text{pK}_a$ .

Following the HH model described above, we define the surface  $\text{pK}_a$  to be the pH at which the surface number density of the protonated acid form and deprotonated conjugate base are equal, i.e.  $\rho_{\text{HA}} = \rho_{\text{A}^-}$ . This was determined by finding the pH at which the carbonyl and carboxylate (*ss*) peak amplitudes intersect and is indicated by the dashed lines in **Figure 3.4c** for each acid. The results obtained by this SFG analysis are consistent with our surface tension measurements and are listed in **Table 3.1**. The surface

$pK_a$  determined by SFG titration for each aliphatic acid is larger than the bulk  $pK_a$ , and the trend as a function of number of carbons is consistent with previous literature studies as well.<sup>71, 74, 116, 118</sup> That is, the surface  $pK_a$  as determined by sum-frequency spectroscopy increases with increasing carbon chain length,  $C_n$ . A small difference in the magnitude of the experimentally determined surface  $pK_a$  between the surface tension titration and the SFG analysis is observed. However the differences reported here are small, as they are within 5% each  $C_n$  acid.

A summary of the results obtained in these studies, along with the results from previous literature are shown in **Figure 3.5**. Including the shorter chain aliphatic acids from the current study, a clear trend of increasing surface  $pK_a$  with increasing number of carbons from  $C_2$  to  $C_{18}$  is observed.

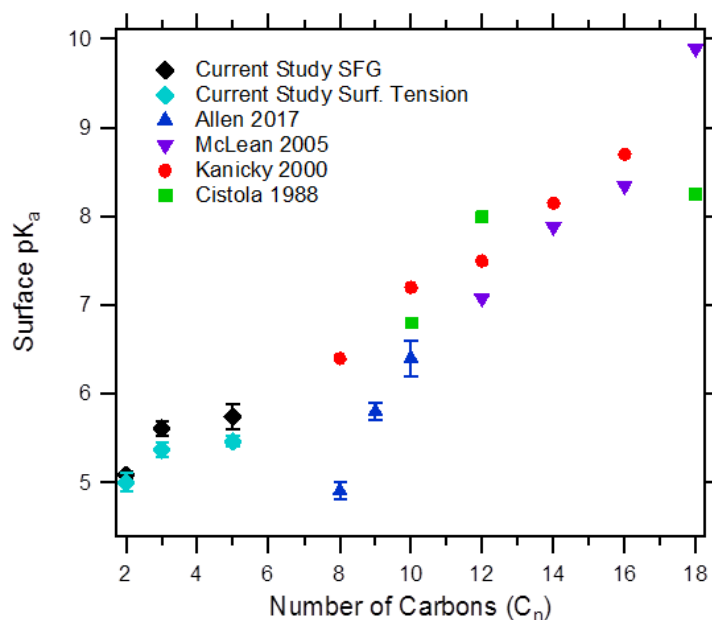


**Figure 3.5: Summarized values of surface  $pK_a$  from previous literature studies.**<sup>71, 74, 116, 118</sup> The results from our surface tension and SFG studies are depicted as the turquoise and black diamonds, respectively.

A variety of techniques and experimental conditions were used to determine these values, so inconsistencies in the literature results are justified. As mentioned by Allen et al.<sup>118</sup>, the inconsistencies can be attributed to the use of different concentrations, which may affect the activity coefficient of the ionized species and lead to the observed differences in surface  $pK_a$ .<sup>122</sup> Furthermore, it has been previously shown that the  $pK_a$  decreases upon dilution of fatty acid systems.<sup>75</sup> We should note that 250 mM valeric acid solutions were used for our studies compared to 1M solutions for acetic acid and propionic acid. However, the experimentally determined  $pK_a$  of valeric acid was greater than that of acetic and propionic acid.

### 3.4 Conclusion

The surface  $pK_a$  of acetic ( $C_2$ ), propionic ( $C_3$ ), and valeric ( $C_5$ ) acid were determined by macroscopic surface tension measurements and molecular level measurements via sum-frequency generation spectroscopy. Both methods reveal the same trends in the surface  $pK_a$  of these acids. That is, at the air-water interface the surface  $pK_a$  is larger than the bulk value  $pK_a$ , indicating that the protonated species is more favorable than the ionized deprotonated species compared to the bulk at the same pH. In addition, both methods reveal that the  $pK_a$  increases with increasing carbon chain length due to stronger interactions between the hydrophobic tails. With the addition of our data, surface  $pK_a$  values as a function of carbon chain length from  $C_2$ - $C_{18}$  have been determined, although some discrepancies still exist due to differences in experimental methods, such as the concentrations used. Future studies of this work can be aimed at performing SFG intensity measurements for the carbonyl and carboxylate (*ss*) modes with the medium and

long-chain acids. We expect to see an increasing trend and anticipate the uncertainty in the surface  $pK_a$  values for  $C_n \geq 8$  will be reduced by maintaining consistent fatty acid concentration and ionic strength.

Due to the role that fatty acids play in environmental, atmospheric, and biological systems<sup>7, 48-51</sup>, understanding the reactivity of these molecules at the interface is crucial. Furthermore, the surface  $pK_a$  values should be utilized when applied to systems such as atmospheric aerosols or lung surfactant.

### 3.5 Supporting Information

#### 3.5.1 Surface Activity Model

The equilibrium constant for the dissociation of an acid, HA, at the surface can be written as

$$K_a = \frac{[A^-][H^+]}{[HA]} \quad (S3.1)$$

From Eq. S3.1, the fraction of protonated (HA) and deprotonated ( $A^-$ ) species can be written as

$$f_{HA} = \frac{1}{1+K_a[H^+]^{-1}} \text{ and } f_{A^-} = \frac{K_a[H^+]^{-1}}{1+K_a[H^+]^{-1}} \quad (S3.2)$$

and using the definition of pH and  $pK_a$  we can express Eq. S3.2 as

$$f_{HA} = \frac{1}{1+10^{(pH-pK_a)}} \text{ and } f_{A^-} = \frac{10^{(pH-pK_a)}}{1+10^{(pH-pK_a)}} \quad (S3.3)$$

In order to adapt Cratin's surface activity model<sup>120</sup> to the short-chain aliphatic acids, the surface tension must be presented as a difference  $\Delta\gamma$  against pH, where  $\Delta\gamma = \gamma_{\max} - \gamma$  and  $\gamma_{\max}$  is the surface tension of  $C_n$  at pH 12. The surface activity is then defined in terms of lowering the surface tension

$$a = \frac{(\Delta\gamma_{\max} - \Delta\gamma)}{\Delta\gamma_{\max}} \quad (\text{S3.4})$$

where  $\Delta\gamma_{\max}$  is the surface tension difference between the highest pH solution and the lowest pH solution. In order to express the total activity of the system ( $a_t$ ) as a sum of the activity and fraction of protonated and deprotonated species, we must assume that all species only interact weakly. Thus, the total activity can be expressed as

$$\frac{(\Delta\gamma_{\max} - \Delta\gamma)}{\Delta\gamma_{\max}} = a_{\text{HA}}f_{\text{HA}} + a_{\text{A}^-}f_{\text{A}^-}. \quad (\text{S3.5})$$

As Allen et al. showed in their study,<sup>118</sup>  $a_{\text{A}^-} = 1$  and  $a_{\text{HA}} = 0$ . Equation S3.5 can then be rearranged to the form used for fitting (Eq. 3.3).

### 3.5.2 Henderson-Hasselbalch Fitting Model for SFG Amplitudes

Equation 3.4 in the Results/Discussion section above is derived from the Henderson-Hasselbalch relation between pH and  $\text{pK}_a$ :

$$\text{pH} = \text{pK}_a + \log \frac{[\text{A}^-]}{[\text{HA}]} \quad (\text{S3.6})$$

From Eq. S3.6 we can express the ratio of deprotonated to protonated species as

$$\frac{[\text{A}^-]}{[\text{HA}]} = 10^{(\text{pH} - \text{pK}_a)} \quad (\text{S3.7})$$

In order to apply the Henderson-Hasselbalch model to our system we must assume that the total concentration of protonated and deprotonated species at the interface does not change, that is  $[\text{HA}] + [\text{A}^-]$  remains constant. For the protonated species, we denote the total surface concentration as  $[\text{HA}]_{\max}$ , giving the expression

$$\frac{[\text{HA}]_{\max} - [\text{HA}]}{[\text{HA}]} = 10^{(\text{pH} - \text{pK}_a)}. \quad (\text{S3.8})$$

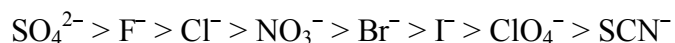
Since the peak amplitude is proportional to the surface number density, the value  $[\text{HA}]_{\text{max}}$  is based on the carbonyl peak stretching amplitude at the lowest pH. We can then rewrite Eq. S3.7 in terms of the number density, yielding

$$\rho_{\text{HA}} = A_{\text{max}}^{1725} \frac{1}{1+10^{(\text{pH}-\text{pK}_a)}} + C \quad (3.4)$$

## CHAPTER 4. Ion Effects on poly(*N*-isopropylacrylamide) at the Air-Water Interface Revealed by Vibrational Sum-Frequency Generation Spectroscopy

### 4.1 Introduction

The well-studied Hofmeister series<sup>123-126</sup> characterizes the ability of ions to salt proteins into or out of solution. This is traditionally described by the ability of the salt to “make” or “break” bulk water structure around the solute. The order of anions in the Hofmeister series is listed below:



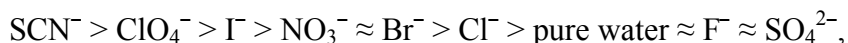
The structure-making anions are known as kosmotropes and salt proteins out of solution (left), while the structure-breaking anions are called chaotropes and salt proteins into solution (right). The Hofmeister effect can be treated as a surface phenomenon occurring at the air-water interface, as past studies<sup>127-129</sup> have shown that the properties of bulk water molecules beyond the immediate solvation shell are essentially unperturbed by ions dissolved in solution. The interfacial water structure at the air-water interface in the presence of poly(*N*-isopropylacrylamide) (pNIPAM) exhibits a Hofmeister trend, becoming more ordered in the presence of chaotropic anions, evidenced by an increase in the OH stretching region SFG intensities.<sup>130</sup>

An ideal technique for investigating structure at the air-water interface is vibrational sum-frequency generation (SFG) spectroscopy. SFG spectroscopy is a second-order nonlinear optical phenomenon that is forbidden in media with inversion symmetry, thus the signal generated excludes contributions from bulk media and selectively probes molecules at the interface—the location where spatial inversion

symmetry is broken. Many water-soluble macromolecules can align their hydrophobic moieties into the gas phase and are therefore surface active. For example, the hydrophobic isopropyl moieties of pNIPAM anchor the polymer to the interface to form a Gibbs monolayer, which is well suited for SFG spectroscopy studies.

pNIPAM is a thermo-responsive biological polymer, which has a lower critical solution temperature (LCST) of 31 °C.<sup>131-133</sup> Below this temperature, pNIPAM exists in a swollen, coiled state and is completely solvated, while above this temperature pNIPAM undergoes a phase transition to a collapsed, globular state.<sup>131</sup> In bulk solution, the addition of kosmotropic Hofmeister salts to pNIPAM lower the LCST from ~31 °C to ~22 °C, and thus pNIPAM will undergo a coil-to-globular transition at temperatures slightly above room temperature.<sup>132, 134</sup> The coil-to-globular transition of pNIPAM can be monitored via FTIR spectroscopy because the amide I mode of the globular form at 1650 cm<sup>-1</sup> is slightly blue shifted relative to its value of 1625 cm<sup>-1</sup> in the coiled form.<sup>135-136</sup> The blue shift of the amide I mode in the globular form is attributed to the intra- and inter-chain hydrogen bonded amide I mode, i.e. C=O hydrogen bonding with N-H<sup>135, 137</sup> that occurs when water is expelled from the polymer chain.

Previous SFG studies of pNIPAM in the presence of Hofmeister salts by Cremer et al.<sup>130</sup> showed that the interfacial water structure became more ordered with chaotropic anions, following the Hofmeister series,



with the most chaotropic anions inducing the most ordering and the most kosmotropic anions not inducing ordering of the interfacial waters. While the water structure at the

interface was affected by the Hofmeister ions, Cremer's study of the CH stretching region showed that the pNIPAM structure remains nearly unchanged at the air-water interface.<sup>130</sup>

This chapter describes the effects of Hofmeister salts on poly(*N*-isopropylacrylamide) (pNIPAM) structure at the air-water interface using sum-frequency generation (SFG) spectroscopy by directly monitoring the pNIPAM molecules via the amide I stretching mode, centered at 1630/1625  $\text{cm}^{-1}$  in  $\text{H}_2\text{O}/\text{D}_2\text{O}$ , respectively. Our results differ from previous literature that shows chaotropic anions do not alter the structure of pNIPAM at the air-water interface. We observe two distinct observations that have not yet been previously reported for pNIPAM at the air-water interface: (i.) the structure of pNIPAM is altered in the presence of different Hofmeister salts, due to the presence of two solvation environments, and (ii.) a Hofmeister trend can be seen in the amide I mode of pNIPAM.

## 4.2 Experimental

*Sample Preparation.* Poly(*n*-isopropylacrylamide),  $M_n = 20,000\text{-}40,000$  (Sigma Aldrich, used as delivered), stock solutions were prepared by dissolving 0.6 mg/mL in  $\text{H}_2\text{O}$  (Millipore, 18.2  $\text{M}\Omega\cdot\text{cm}$ ). Solutions in  $\text{D}_2\text{O}$  were made using  $\text{D}_2\text{O}$  purchased from Cambridge Isotopes. Stock pNIPAM solutions were diluted to a final concentration of 0.06 mg/mL in 1M salt solutions (sodium thiocyanate, sodium perchlorate, sodium nitrate, sodium bromide, and sodium chloride). Sodium sulfate solutions were prepared at 0.33 M to maintain a constant ionic strength. All sodium salts were purchased from Sigma Aldrich and used as delivered. Cloudy pNIPAM solutions were stored in a refrigerator

overnight to dissolve completely and allowed to warm to room temperature before collecting SFG spectra.

*Sum Frequency Generation (SFG) Spectroscopy.* All SFG spectra were recorded with a broad-band vibrational sum-frequency spectrometer as previously described<sup>43-44</sup> and normalized to the non-resonant SFG response of a GaAs crystal. The intensity of the sum-frequency generation signal,  $I_{SFG}$ , can be expressed as<sup>11</sup>

$$I_{SFG} \propto \left| \chi_{NR}^{(2)} + \sum_q \chi_q^{(2)} \right|^2 I_{800} I_{IR} \quad (4.1)$$

where  $I_{800}$  and  $I_{IR}$  are the intensities of the incident 800 nm and IR beams, respectively.

$\chi_{NR}^{(2)}$  and  $\chi_q^{(2)}$  are the complex second order susceptibilities of the non-resonant background that include contributions from the water bending mode<sup>92-93</sup> and the vibrationally resonant sum-frequency term. The resonant term,  $\chi_q^{(2)}$ , can be expressed as<sup>33, 105</sup>

$$\chi_q^{(2)} \propto \frac{A_q}{\omega_{IR} - \omega_q + i\Gamma_q} \quad (4.2)$$

where  $\omega_{IR}$  is the frequency of the incident IR beam.  $A_q$ ,  $\omega_q$ , and  $\Gamma_q$  are the amplitude, the frequency and the line width of the vibrational transition, respectively. The amplitude,  $A_q$  is only nonzero if the  $q^{\text{th}}$  mode is both Raman and IR active. Peak amplitudes and frequencies were obtained by fitting SFG spectra to Eq. 4.1 and 4.2.

### 4.3 Results and Discussion

Our study focuses on the differences between the bulk and interfacial pNIPAM vibrational spectra, while also observing the specific ion effect on pNIPAM at the air-water interface, by monitoring the amide I mode, via sum-frequency generation

spectroscopy. Any changes of the amide I peak in the SFG spectrum, as a function of anion, indicate that the Hofmeister salts can have a direct effect on the pNIPAM structure at the air-water interface. This has not yet been reported in previous literature.

The ATR-FTIR spectrum of pNIPAM in D<sub>2</sub>O, shown in **Figure 4.1**, is consistent with previous FTIR studies<sup>135-137</sup> and shows one visible peak in the amide I region centered at 1625 cm<sup>-1</sup>.

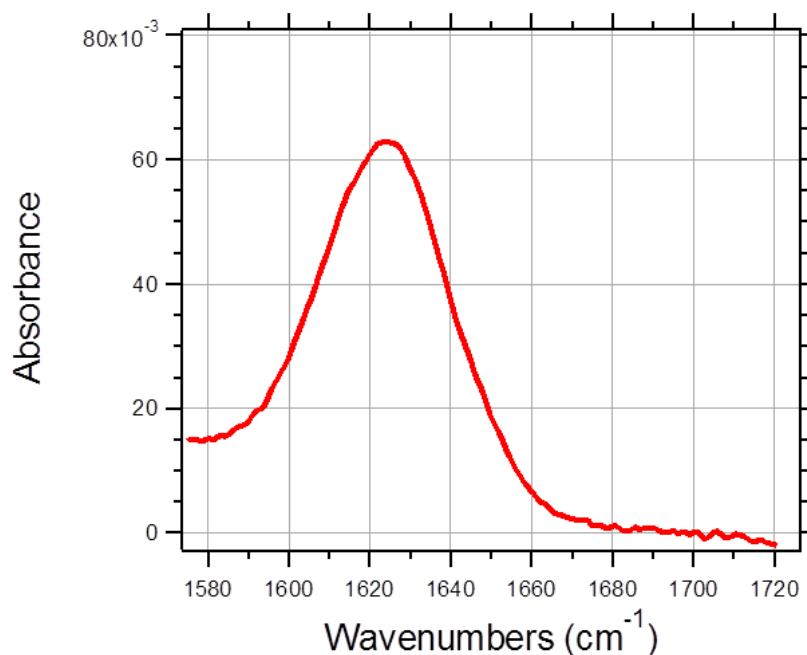


**Figure 4.1:** ATR-FTIR spectrum of 0.6 mg/mL pNIPAM dissolved in D<sub>2</sub>O in the amide I region. D<sub>2</sub>O was used as the solvent to avoid overlap with the OH bending mode centered at 1600 cm<sup>-1</sup>. One amide I peak centered at 1625 cm<sup>-1</sup> is visible.

The IR spectrum was collected in D<sub>2</sub>O to avoid spectral overlap in this region with the H<sub>2</sub>O bending mode.<sup>137</sup> This feature is due to the amide I mode of pNIPAM molecules, arising from a combination of C=O and C-N stretching modes,<sup>135</sup> that are fully solvated in bulk water by the surrounding D<sub>2</sub>O molecules. However, the sum-frequency generation (SFG) spectrum of pNIPAM in H<sub>2</sub>O and D<sub>2</sub>O, **Figure 4.2 (a and b,**

respectively), shows one visible peak centered at  $\sim 1665\text{ cm}^{-1}$ , nearly  $40\text{ cm}^{-1}$  blue shifted from the bulk FTIR spectrum. A second, smaller intensity peak can be seen at  $\sim 1630\text{ cm}^{-1}$  in  $\text{H}_2\text{O}$  and  $\sim 1625\text{ cm}^{-1}$  in  $\text{D}_2\text{O}$ , corresponding to the amide I mode observed in the bulk FTIR spectrum. Since SFG is a surface-selective technique, only the pNIPAM molecules at the air-water interface are probed. Therefore, the observed blue shift is due to the “free” amide I modes of pNIPAM—amide I modes arising from non-fully hydrogen bonded C=O moieties in pNIPAM<sup>137</sup>—while the peak centered at  $1630/1625\text{ cm}^{-1}$  corresponds to a “sub-phase” layer of pNIPAM in which the amide I vibrational feature is due to fully hydrogen bonded C=O moieties in the solvating  $\text{H}_2\text{O}/\text{D}_2\text{O}$ , respectively .

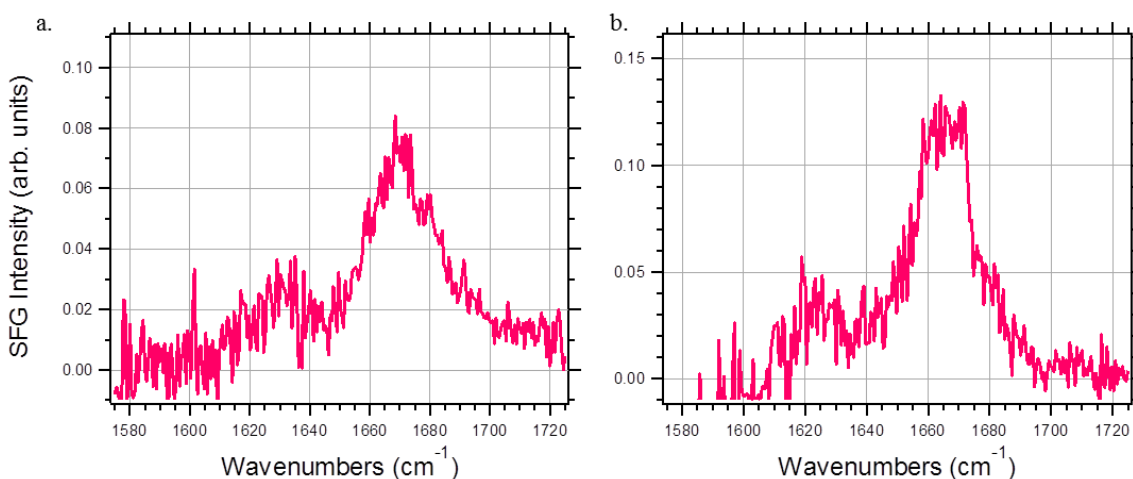


**Figure 4.2: SFG spectrum of 0.06 mg/mL pNIPAM in (a)  $\text{H}_2\text{O}$  and (b)  $\text{D}_2\text{O}$ . Two amide I peaks are visible, indicative of two different solvation environments at the air-water interface. The higher intensity peak centered at  $1665\text{ cm}^{-1}$  is attributed to the “free” amide I peak—amide I moieties located in the hydrophobic region closest to the air. The smaller peak located at  $1625\text{ cm}^{-1}$  is due to pNIPAM amide I moieties located in the sub-phase layer that is solvated by  $\text{H}_2\text{O}$ . This peak appears at the same frequency as the bulk amide I mode of pNIPAM in the ATR-FTIR spectrum.**

These features are analogous to what is observed in the sum frequency spectrum of pure water, where the “dangling” OH stretching mode is blue shifted from the bulk-like hydrogen bonded OH stretching mode.<sup>11, 33, 138-140</sup>

**Figure 4.3** shows the SFG spectra of the pNIPAM amide I mode with the addition of various Hofmeister salts. The addition of kosmotropic anions, such as  $\text{Cl}^-$  and  $\text{SO}_4^{2-}$ , has no discernible effect on the SFG spectra of the pNIPAM amide I mode (purple and light blue curves, respectively), and these spectra are unchanged from that of pNIPAM dissolved in  $\text{H}_2\text{O}/\text{D}_2\text{O}$  without the addition of Hofmeister salts. However, as the anions became more chaotropic we observe an increase in the intensity of the amide I peak centered at  $1630/1625\text{ cm}^{-1}$ .

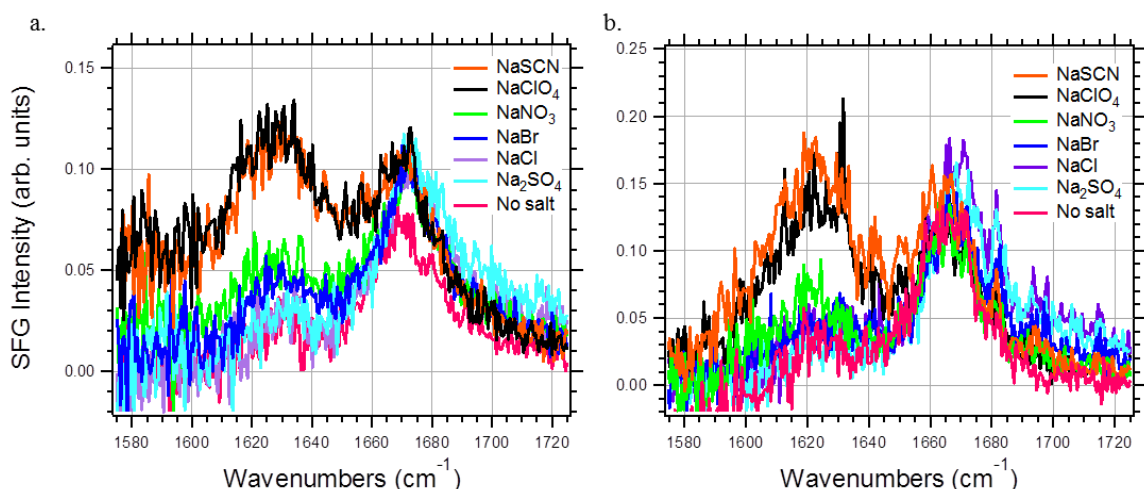


**Figure 4.3: SFG spectra of 0.06 mg/mL pNIPAM in 1 M salt solutions dissolved in (a)  $\text{H}_2\text{O}$  and (b)  $\text{D}_2\text{O}$ .  $\text{Na}_2\text{SO}_4$  concentration was 0.33 M to maintain constant ionic strength. The free amide I peak, centered at  $1665\text{ cm}^{-1}$ , does not exhibit a Hofmeister trend, as the peak intensity remains constant with varying anions. The sub-phase amide I peak ( $1625\text{ cm}^{-1}$ ) shows a Hofmeister trend, as the peak intensity is small in the presence of kosmotropic anions,  $\text{SO}_4^-$  and  $\text{Cl}^-$ , and becomes greater with more chaotropic anions, such as  $\text{SCN}^-$  and  $\text{ClO}_4^-$ .**

Since this peak is a feature of the bulk spectrum of pNIPAM, it indicates that this amide I mode is due to solvated  $\text{C}=\text{O}$  moieties that are fully hydrogen bonded to the surrounding  $\text{H}_2\text{O}/\text{D}_2\text{O}$ . The black and red curves in **Figure 4.3** show the SFG spectra of pNIPAM in the presence of 1M  $\text{ClO}_4^-$  and  $\text{SCN}^-$ , respectively. In the presence of chaotropic anions,

the “bulk-like” amide I mode intensity matches the free (non-hydrogen bonded) amide I mode intensity, which remains unchanged as a function of Hofmeister anion. Along with the absence of an isosbestic point, this indicates that at the air-water interface there is no exchange between states—i.e. the free amide I moieties are *not* being solvated into “bulk-like” amide I moieties—when dissolved with kosmotropic versus chaotropic anions.

The “bulk-like” amide I peak can be attributed to a sub-phase layer of pNIPAM that forms as more chaotropic anions are introduced. We propose that the sub-phase layer of pNIPAM forms due to the ordering of interfacial water structure in the presence of chaotropic anions, as shown schematically in **Figure 4.4** and quantitatively in **Figure 4.5**.

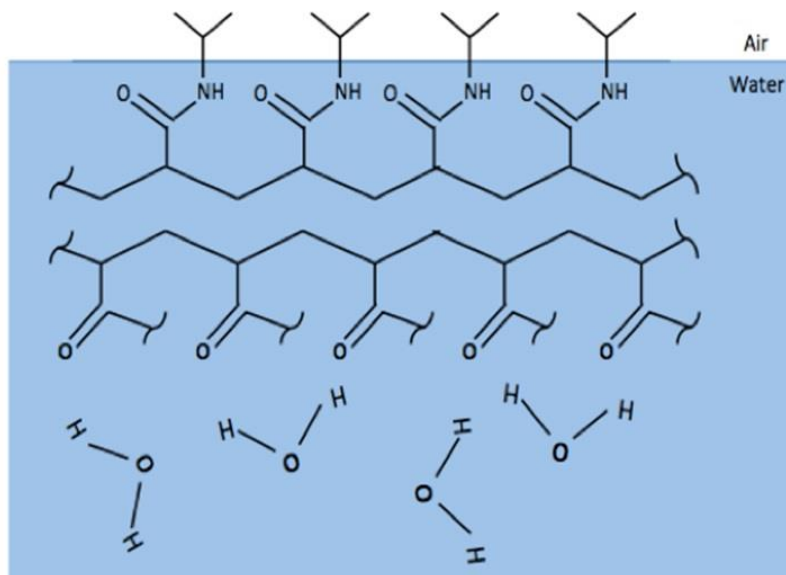


**Figure 4.4: Depiction of pNIPAM structure at the air-water interface. The hydrophobic isopropyl moieties can anchor pNIPAM to the surface, expelling water molecules and leading to a hydrophobic environment than in the bulk. The amide I moieties in this solvation environment give rise to the free amide I peak, centered at  $1665\text{ cm}^{-1}$  in the SFG spectrum and are unaffected by the Hofmeister anions. The second layer of pNIPAM represents the sub-phase, bulk-like pNIPAM structure that can be ordered by the increasing interfacial water structure in the presence of chaotropic anions. This layer of pNIPAM exhibits a Hofmeister trend, as the peak intensity of the  $1630\text{ cm}^{-1}$  peak in the SFG spectrum increases with more chaotropic anions.**

Previous SFG studies have shown that interfacial water molecules become more aligned as anions become more chaotropic, while having no effect on the pNIPAM molecules at the interface.<sup>130</sup> The increased structure of the interfacial water molecules is taken to account for increased alignment of the amide I modes in the sub-phase layer through hydrogen bonding interactions. It has been shown that nonlinear responses can be improved by inducing the alignment of dipoles.<sup>141-142</sup> We believe that increased interfacial water alignment and interaction with pNIPAM amide I moieties through hydrogen bonding—this is evidenced by the SFG amide I mode appearing at the same

frequency as the bulk amide I mode in, shown in **Figure 4.1**—induces alignment of the amide I transition dipoles. Thus, a larger SFG response is observed from amide I moieties in the presence of chaotropic anions.

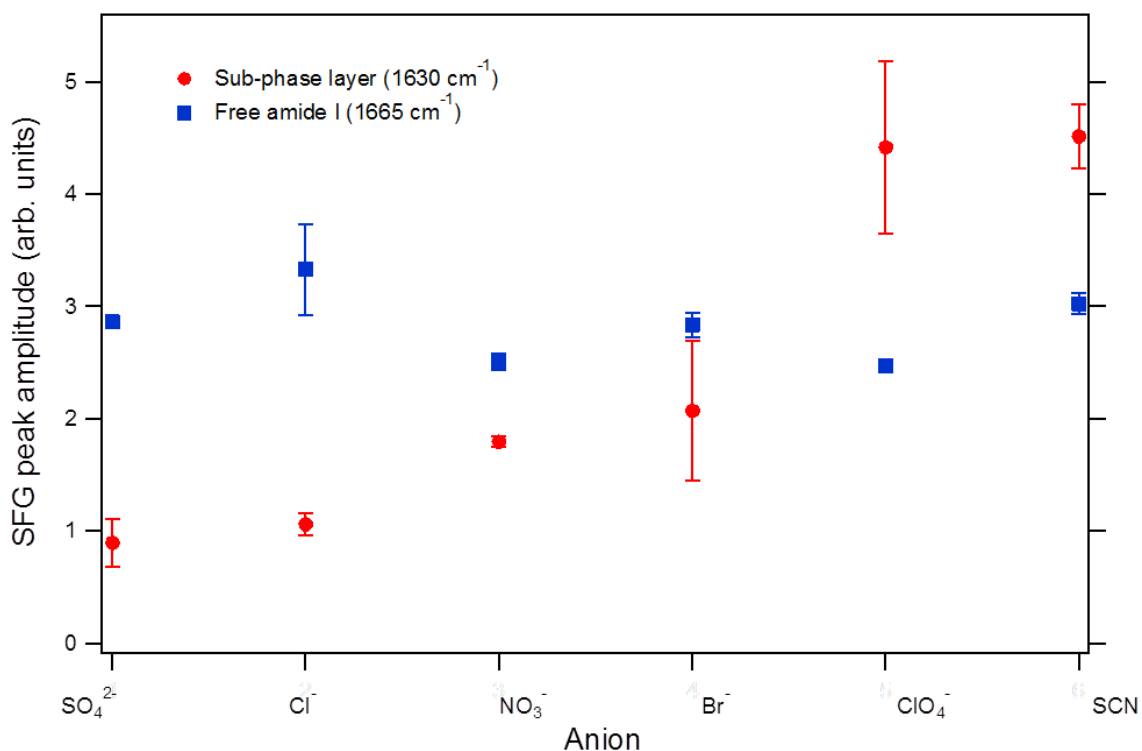
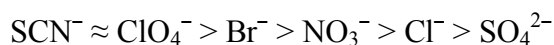


**Figure 4.5:** The SFG free amide I peak amplitude (blue squares) and the sub-phase amide I peak amplitude (red circles) of pNIPAM plotted against Hofmeister anions. The free amide I peak amplitude remains constant as a function of Hofmeister anion, indicating that the pNIPAM structure in the uppermost layer does not exhibit a Hofmeister trend. The sub-phase amide I peak amplitude increases as the anions become more chaotropic, attributed to the increasing interfacial water structure. This is the first evidence of a direct Hofmeister effect on the structure of pNIPAM at the air-water interface.

It is interesting to note that the bulk-like amide I mode follows the Hofmeister series, as the peak intensity increases with the more chaotropic anions, while the free amide I mode remains unchanged (**Fig. 4.5**). **Figure 4.5** plots the free amide I (blue) and sub-phase amide I mode (red) SFG peak amplitude for each anion. The peak amplitude is

an indication of the number of molecules at the interface; an increase in the ratio corresponds to more molecules contributing to the signal. For the free amide I mode, centered at  $\sim 1665\text{ cm}^{-1}$ , the peak amplitude remains unchanged, indicating that the anions have no discernable effect on the amide I moieties at uppermost layer of the air-water interface. This could be due to the pNIPAM polymer chain occupying the interface, expelling water, and preventing the anions from inducing any interfacial water structure near the interfacial amide I moieties. Thus no Hofmeister trend is seen in this region of the interface. This is corroborated by sum-frequency studies of the pNIPAM CH stretching region as a function of anion by Cremer et al.<sup>130</sup> Their studies show that anions do not substantially perturb the CH stretching moieties of pNIPAM at the air-water interface, as no change in CH stretching SFG peak intensities or peak positions were observed. The lack of change in the SFG spectra were attributed to the interaction of the hydrophobic isopropyl side chains with the vapor phase, maintaining fixed orientations for the pNIPAM molecules at the interface regardless of the anion in solution.<sup>130</sup>

In contrast to the free amide I moiety, a Hofmeister trend can be seen in the peak amplitude of the sub-phase layer amide I moiety. As the anions become more chaotropic the peak amplitude increases in magnitude, with  $\text{SO}_4^{2-}$  giving the lowest amplitude while  $\text{SCN}^-$  and  $\text{ClO}_4^-$  give the largest amplitude, following the order:



This Hofmeister trend is similar to what was observed by Cremer et al. in 2007,<sup>130</sup> who reported that the chaotropic anions induced interfacial water structure, while the kosmotropic anions did not. However, our results differ somewhat to those obtained by

Cremer et al. While the pNIPAM molecules at the upper-most layer of the interface are unaffected by the addition of Hofmeister anions, the “bulk-like” amide I moieties exhibit a Hofmeister trend. This observation has not yet been reported in previous literature.

#### 4.4 Conclusion

The SFG spectrum of the pNIPAM amide I mode at the interface differs from what is observed in bulk ATR-FTIR. The bulk FTIR spectrum shows one amide I peak, while the SFG spectrum shows two amide I peaks, one centered at  $1625\text{ cm}^{-1}$  (consistent with bulk amide I modes), and the other at  $1665\text{ cm}^{-1}$ . The two peaks are due to two distinct solvation environments that are present near the air-water interface. At the upper-most layer of the interface, the hydrophobic isopropyl moieties can anchor pNIPAM to the surface by pointing out into the air and expelling water molecules from the surface in the process. Thus the blue-shifted “free” amide I mode observed in the SFG spectrum of pNIPAM arises due to C=O moieties that are not fully hydrogen bonded to the surrounding water molecules. The amide I mode that is consistent with the bulk FTIR spectrum of pNIPAM arises from a sub-phase layer of pNIPAM molecules that are able to hydrogen bond to the surrounding water molecules.

The effects of Hofmeister salts on interfacial pNIPAM molecules were also directly monitored via sum-frequency generation spectroscopy. The results of this show that there is no discernable Hofmeister trend on the “free” amide I mode, evidenced by constant amplitude to peak width ratio as a function of Hofmeister anion. However, there is direct evidence of a Hofmeister trend on the sub-phase amide I moiety of pNIPAM, where chaotropic anions give a rise to the bulk-like amide I mode, which has not been

previously reported. This Hofmeister effect on the amide I mode of pNIPAM is attributed to the ordering of interfacial water molecules in the presence of chaotropic anions. We propose that the ordering of interfacial water molecules promote the solvation and alignment of amide I dipoles, giving rise to the increase in the “bulk-like” amide I peak SFG intensity.

## CHAPTER 5. Spectroscopic Evidence for the Origin of Odd-Even Effects in Self-Assemble Monolayers and Effects of Substrate Roughness

### 5.1 Introduction

The odd–even effect, which describes the oscillations in structure and the resultant properties depending on the presence of either an odd or even number of repeating units, has been widely observed across basic science and engineering.<sup>143-153</sup> The odd–even effect in *n*-alkanethiolate self-assembled monolayers (SAMs) manifests in properties like wetting, charge transport, melting point, friction, and vibrational spectroscopy.<sup>147-152</sup> These properties are dependent on the presence of either odd (SAM<sup>O</sup>) or even (SAM<sup>E</sup>) numbers of non-H atoms in the *n*-alkanethiolate molecule making up the SAM.<sup>147-148, 150-151</sup> The origin of the odd–even effect in SAMs is, therefore, either due to (i) variation in the tilting angle of the terminal group, considered as either –CH<sub>3</sub> or –CH<sub>2</sub>–CH<sub>3</sub>, or (ii) the effect of molecular orientation on the effective surface normal dipole. From an idealized model of a SAM, chemisorbed all-trans extended *n*-alkanethiol molecules on a gold (Au) surface show different tilting angles for the terminal –CH<sub>2</sub>–CH<sub>3</sub> group depending on whether the molecule bears an odd or even number of carbons (**Fig. 5.1a**).

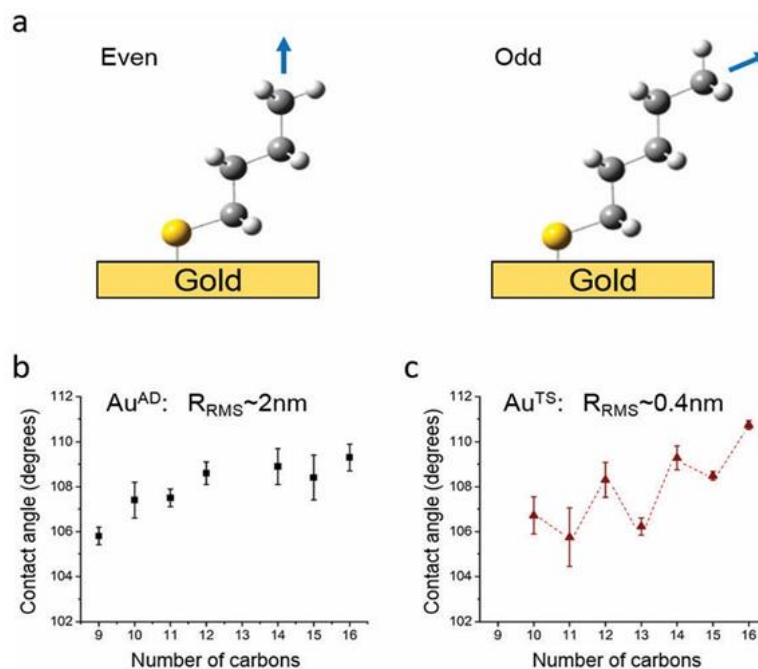


**Figure 5.1: Previously described manifestation of the odd–even effect in selfassembled monolayers.<sup>147-148</sup> (a) A schematic illustration of the odd–even effect in an ideal all-trans *n*-alkanethiol attached on Au and its effect on surface dipoles. (b and c) Dependence of the odd–even effect in hydrophobicity of self-assembled monolayers on surface roughness. The magnitude of the zig-zag oscillation is inversely proportional to the roughness.**

Techniques that have been utilized to investigate the odd–even effect in SAMs include wetting,<sup>147-148, 150</sup> UV-photoelectron spectroscopy (UPS),<sup>154</sup> X-ray photoelectron spectroscopy (XPS),<sup>153, 155</sup> near edge X-ray absorption fine structure spectroscopy (NEXAFS),<sup>156-157</sup> scanning tunneling microscopy (STM),<sup>158-162</sup> atomic force microscopy (AFM),<sup>143</sup> infrared reflection absorption spectroscopy (IRRAS),<sup>143, 161, 163</sup> cyclic voltammetry,<sup>164-165</sup> and sum frequency generation (SFG).<sup>166-167</sup> All these studies have focused on defects and/or orientation of the terminal moiety without consideration of the stereo-electronic effects (the relation between the 3D molecular structure and the associated electronic structure) resulting from molecular orientation and its effect(s) on

the local chemical environment of the terminal moiety and its subsequent influence on SAM surface properties. The orientation of this terminal group is, however, also dependent on the morphology of the substrate used to fabricate the SAMs.

Sum-frequency-generation spectroscopy is a well-known, powerful nonlinear technique that can be used to selectively obtain the vibrational spectra of molecules at interfaces.<sup>11, 36, 168-169</sup> SFG is sensitive only to molecules adsorbed at interfaces because the second-order susceptibility becomes zero in media with inversion symmetry under the electric dipole approximation.<sup>168</sup> Nishi and co-workers first applied SFG to investigate the odd–even effects of SAMs of *n*-alkanethiols on gold surfaces.<sup>167</sup> Compared with direct IR spectroscopic measurements, SFG is more sensitive to the orientation of the terminal methyl group in *n*-alkanethiolate SAMs because nonlinear spectroscopies have a higher order dependence on angular factors. Nishi and coworkers observed a chain-length dependence of the SFG intensity ratio of the CH<sub>3</sub> symmetric to CH<sub>3</sub> asymmetric stretching modes, and attributed the difference to differences in the orientation of the methyl group in SAM<sup>E</sup> and SAM<sup>O</sup>. Their results also assumed (or implied without substrate data) that the alkyl chains of SAMs, on their surfaces, showed an all-trans conformation. Cimatu and coworkers used SFG imaging microscopy (SFGIM) to chemically visualize regions of micro-contact-printed SAMs derived from C<sub>16</sub> or C<sub>17</sub> thiols.<sup>166</sup> Guo and coworkers provided a global modeling of SFG spectra of SAMs of alkanethiols on gold.<sup>170</sup> Their model included the Fermi resonance of the CH<sub>3</sub> symmetric stretch with the CH<sub>3</sub> bending overtone. They applied their model to simulate the odd–even intensity alternation of SFG CH<sub>3</sub> vibrational bands as a function of chain length.

We<sup>147-148, 150-151</sup> and others<sup>152, 171-173</sup> are interested in understanding and developing applications of the odd–even effect in SAMs—and more broadly, the role of interfacial stereo-electronic effects on SAM properties<sup>147</sup> and their applications.<sup>152, 157</sup> Nijhuis and coworkers have recently reported that substrate surface topology, i.e. grain boundaries and grain size, strongly affect the rate of charge transport across SAMs.<sup>174-176</sup> We recently reported that the odd–even effect in the hydrophobicity of SAMs depends on the degree of surface roughness and showed existence of a surface roughness transition point at which the odd–even effect is not detectable by wetting (**Fig. 5.1b** and **5.1c**).<sup>147, 177-178</sup> On comparatively rough “as-deposited” gold surfaces ( $\text{Au}^{\text{AD}}$ ), the odd–even oscillation in water contact angle was not observed (**Fig. 5.1c**), while on smoother template-stripped gold surfaces,  $\text{Au}^{\text{TS}}$ , we observed a significant odd–even effect in hydrophobicity (**Fig. 5.1d**).<sup>147-148</sup> Interestingly, the zig-zag odd–even oscillation in contact angles with water is asymmetric  $\langle C_{12}$  and symmetric  $\rangle C_{14}$  with  $C_{13}$  giving inconsistent values of contact angle that the cause of which we are yet to understand. We also demonstrated, from an extrapolation of contact angles derived from both  $\text{SAM}^{\text{O}}$  and  $\text{SAM}^{\text{E}}$ , a dependence of the magnitude of the odd–even effect in hydrophobicity on roughness.<sup>147</sup> We hypothesized that the roughness dependence of this odd–even effect is, in part, due to changes in how well the SAM is ordered. We, however, at the time, did not have any direct spectroscopic evidence for this inference. This inference is, in part, an overgeneralization since the wetting properties depend on both the local structure (roughness) and the chemical differences between the moieties on the surface and those on the wetting liquid. Recently,<sup>177</sup> we have observed that the odd–even effect in SAM wetting by non-polar

liquids (oleophilicity) is not significantly affected by substrate roughness, suggesting that the odd–even effect in wetting may entail more than just the structural orientation of the CH<sub>3</sub> moiety. This discrepancy in substrate-roughness dependence of hydrophobicity vs. oleophilicity—two otherwise complementary surface properties—calls for further detailed studies of the evolution of surface structure with changing molecular length and the role of substrate morphology in such changes. To evaluate our earlier inference and build a better understanding of the nature of the SAM interface, we hypothesized that (i) as expected, there should be a significant difference in the SFG signal across an interface of a SAM on a smooth and rough surface, in part due to the expected difference in the overall order of the SAM and the orientation of terminal moieties. (ii) The expected decrease in gauche defects with an increase in molecular length should lead to significant changes in the local intermolecular chemical environment of the terminal CH<sub>3</sub> moiety, a feature that has largely been ignored in previous studies. The latter may be partly responsible for the recently observed discrepancy<sup>147, 177</sup> in the effect of surface roughness on wetting with polar and non-polar liquids in *n*-alkanethiolate SAMs.

## 5.2 Experimental

### *Chemicals and materials*

All chemicals except 1-hexadecanethiol (TCI) and ethanol (Pharmco-AAPER) were purchased from Sigma-Aldrich and were used as received. All Au substrates were either prepared in-house or purchased from Substrata Solution Inc. and were used as received. A 200 nm layer of Au was e-beam evaporated onto a 4-inch silicon wafer (100).

### *Preparation of Au surface substrates*

“As-deposited” Au ( $\text{Au}^{\text{AD}}$ ): a 4-inch silicon wafer was coated with a 200 nm thick layer of Au using an e-beam evaporator. The wafer was then rinsed with ethanol and dried with a stream of ultra-high purity nitrogen gas, and was then cut into smaller pieces (1 cm  $\times$  1 cm) using a diamond scribe.

Template striped samples ( $\text{Au}^{\text{TS}}$ ): the template striped gold sample was prepared as described previously.<sup>147-148, 151, 178</sup> In brief, 8 mL of optical adhesive (OA, Norland 61) was applied onto the purchased Au film, and a piece of a clean glass slide was then placed on top of the OA. The sample was then UV cured for 12 hours. Template-striped Au samples were obtained by using a razor blade to lift the glass slide with the attached metal layer from the wafer.

### *AFM characterization*

Atomic force microscopy (Bruker Innova) was used in tapping mode to characterize the surface of the  $\text{Au}^{\text{AD}}$  and  $\text{Au}^{\text{TS}}$  surfaces. An AFM scan was performed at a frequency of 2 Hz with 1024 points per line resolution. AFM data were then processed and analyzed using NanaScope Analysis (v1.5) software to obtain 2D and 3D images, cross-section projection lines and RMS roughness. ImageJ was used to estimate the average grain area and surface coverage.

### *Preparation of *n*-alkanethiolate monolayers*

Both  $\text{Au}^{\text{TS}}$  and  $\text{Au}^{\text{AD}}$  were immersed in vials containing a 3 mM solution of *n*-alkanethiols in ethanol for 3 hours. Prior to immersion, the *n*-alkanethiol solutions were degassed by bubbling ultrahigh purity nitrogen gas for 1 minute. The substrate with

SAMs was then rinsed with copious amounts (*ca.* 2 mL per wash for at least 7 washes) of ethanol and air-dried.

#### *SFG setup and measurements*

The SFG spectrometer used in this study has been previously described.<sup>179</sup> In brief, Ti:sapphire based laser pulses (800 nm, 100 fs, 1 kHz) were produced by a regenerative amplifier system (Libra-F-1k-HE-110, Coherent, CA) and split equally into two beams. One beam pumped an optical parametric amplifier (TOPAS-C, Light Conversion, Lithuania) generating a broad bandwidth ( $\sim 250\text{ cm}^{-1}$ ) IR beam. The other beam passed through a pulse shaper to produce a narrow bandwidth (1.5 ps) pulse. When the narrow bandwidth 800 nm beam was temporally and spatially overlapped with the broad IR beam on a sample surface, the generated SFG signal was collected using a liquid nitrogen-cooled CCD (PyLoN:1340x400B, Princeton Instruments, NJ). Glan-Taylor prisms (Newport Corp.) were used to define the polarizations of the incident 800 nm and signal beams. All SFG spectra of SAMs were acquired in the C–H stretching region between  $2700\text{ cm}^{-1}$  and  $3100\text{ cm}^{-1}$  using the ppp (SF, visible, and IR) polarization configuration, i.e., where the polarization vector of the incident beam and the signal beam is parallel to the plane of incidence that contains the surface normal and the propagation vector of incident light. The acquisition time for each spectrum was 3 seconds.

### **5.3 Results and Discussion**

To evaluate the above hypotheses, Au surfaces with root-mean-square roughness ( $R_{\text{RMS}}$ ) across the odd–even limit,<sup>147, 177</sup> as defined from analysis of wetting measurements, were

prepared ( $R_{\text{RMS}} = 0.40 \text{ nm}$  and  $2.38 \text{ nm}$  for  $\text{Au}^{\text{TS}}$  and  $\text{Au}^{\text{AD}}$ , respectively). These two types ( $\text{Au}^{\text{TS}}$  or  $\text{Au}^{\text{AD}}$ ) of surfaces are commonly used in studies of SAMs as substrates.<sup>148, 150</sup> Atomic force microscopy (AFM) was used to characterize the surface morphology and surface roughness of both  $\text{Au}^{\text{TS}}$  and  $\text{Au}^{\text{AD}}$  (Fig. 5.2a and b and Fig. S3, Supporting Information). ImageJ was used to generate binary images needed to estimate the grain size and surface coverage (see Supporting Information for details).

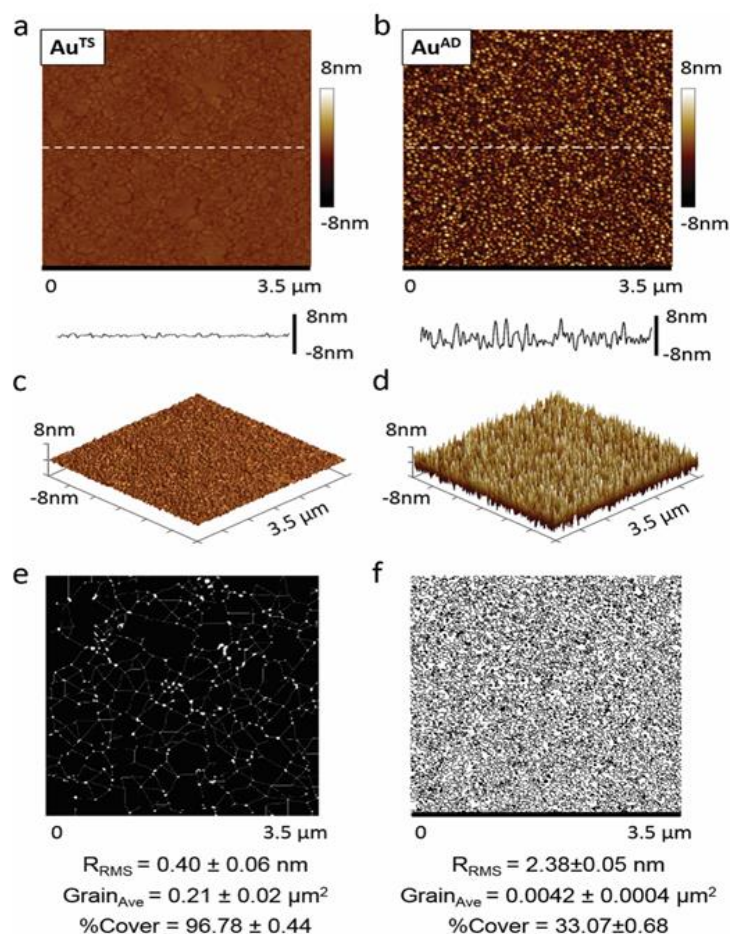


**Figure 5.2: Characterization of Au<sup>TS</sup> and Au<sup>AD</sup> surfaces. (a and b) 2D atomic force microscopy (AFM) images with the corresponding cross-section projection lines. (c and d) 3D view of the AFM image showing asperities on the surfaces. (e and f) The AFM image processed by ImageJ highlighting significant differences in surface coverage and grain areas.**

We observe that the surface morphology is significantly different for these two surfaces with the average grain size being 0.21 and 0.0042  $\mu\text{m}^2$  for Au<sup>TS</sup> and Au<sup>AD</sup>, as shown in **Fig. 5.2a, b and e, f**, respectively. Differences in surface morphologies are also captured by the 3D plots of AFM images (**Fig. 5.2c and d**) and by the cross-sectional line plot (along the dashed white line and the respective 2D AFM topology plots shown in **Fig. 5.2**). Similarly, the percentage of the surface available for well-ordered SAM formation (defined as the surface within 0.1 nm, or *ca.* 1 C–C bond length, of the  $R_{\text{RMS}}$  midline)<sup>170</sup> was 97% and 33% for Au<sup>TS</sup> and Au<sup>AD</sup>, respectively (**Fig. 5.2e and f**). Based on these surface features, SAMs on smooth Au<sup>TS</sup> are likely to be more ordered and pack well compared to those on rough Au<sup>AD</sup>.

SFG spectra were obtained from C<sub>9</sub>–C<sub>16</sub> SAMs fabricated on Au<sup>TS</sup> and Au<sup>AD</sup> (**Fig. 5.3a and b**). Fits of Lorentzian line shapes to these SFG spectra show three major vibrational features centered at approximately 2970  $\text{cm}^{-1}$ , 2940  $\text{cm}^{-1}$  and 2880  $\text{cm}^{-1}$ .<sup>167</sup> (Supporting Information) The bands at 2880  $\text{cm}^{-1}$  and 2970  $\text{cm}^{-1}$  are assigned to the CH<sub>3</sub> symmetric(CH<sub>3</sub>-sym) and asymmetric stretch (CH<sub>3</sub>-asy) bands, respectively.<sup>167</sup> The 2940  $\text{cm}^{-1}$  transition is attributed to the Fermi resonance of the CH<sub>3</sub> symmetric stretch with the CH<sub>3</sub> bending overtone.<sup>170</sup> An odd–even (zig-zag) oscillation in the relative amplitudes of the vibrational intensities of these CH<sub>3</sub> stretching modes is observed in the SFG spectra from SAMs on Au<sup>TS</sup> but not from SAMs on Au<sup>AD</sup> (**Fig. 5.3a and b**).

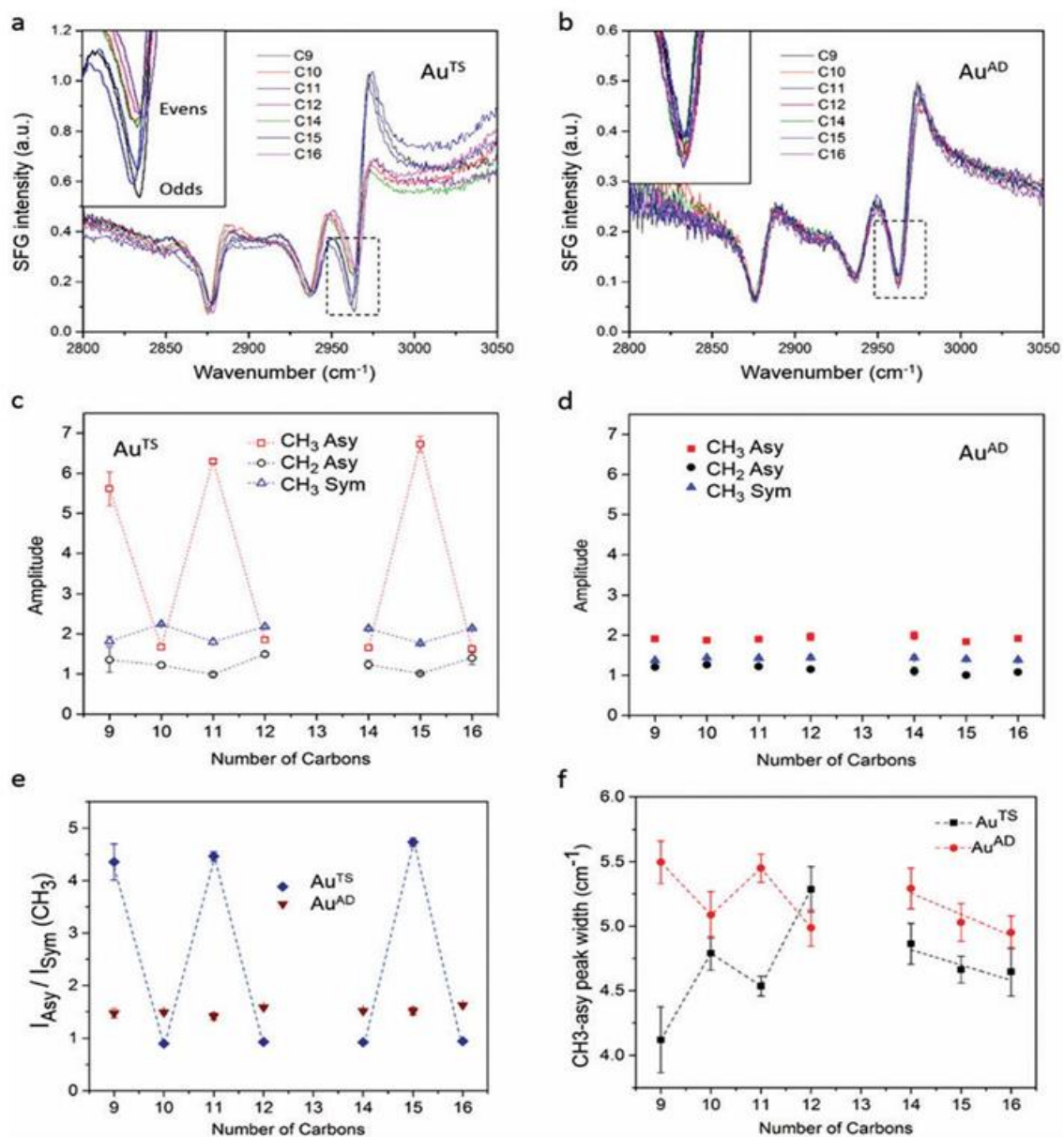


**Figure 5.3: Summary of spectroscopic data.** (a and b) SFG spectra and signal analysis show differences in SAMs on Au<sup>TS</sup> (a) and Au<sup>AD</sup> (b). (c and d) Fitted peak amplitude of the CH<sub>3</sub> asymmetric and symmetric stretches, and the CH<sub>2</sub> asymmetric stretch, derived from the spectra of Au<sup>TS</sup> and Au<sup>AD</sup>, respectively. (e) The ratio of SFG peak signal intensity for the CH<sub>3</sub> asymmetric stretch to the CH<sub>3</sub> symmetric stretch, indicating the increase in the ratio with increasing tilting angle of the terminal CH<sub>3</sub> group relative to the surface normal. (f) The peak width (halfwidth at half maximum, HWHM) of the CH<sub>3</sub> asymmetric stretch.

### 5.3.1 SFG signal intensity and the odd–even effect

The SFG signal strength is dependent on the number density and molecular orientation at the surface. Since all SAMs are prepared on Au, the number of molecules per unit area is expected to be the same.<sup>162, 170</sup> The degree of order or SAM orientation, however, is highly dependent on the surface morphology. Since all SFG signals are generated from *n*-alkanethiolate SAMs on Au surfaces, where the packing density is identical for each carbon chain length, the main difference in the relative SFG signal strengths is, therefore, due to differences in molecule orientations.<sup>167</sup>

By fitting the SFG spectra, the relative amplitude of each C–H stretching band was obtained for Au<sup>TS</sup> and Au<sup>AD</sup> (**Fig. 5.3c and d**). The details of the signal fitting are provided in the Supporting Information. For Au<sup>TS</sup>, a large zig-zag oscillation in the amplitude of the CH<sub>3-asy</sub> stretch is observed with an analogous, albeit small, oscillation observed for the CH<sub>3-sym</sub> stretches. These zig-zag fluctuations indicate a strong variation in the orientation of the terminal CH<sub>3</sub> group that is dependent on an odd or even number of carbons in the molecule making up the SAM. The magnitude of the amplitude segregates into two groups, with the odd-numbered molecules showing a higher amplitude compared to the even-numbered molecules (**Fig. 5.3a and c**). We note that the odd–even oscillation is asymmetric, with SAM<sup>O</sup> (abbreviated CH<sup>O</sup><sub>3-asy</sub>) showing a gradual increase in amplitude with increasing chain length. The SAM<sup>E</sup> (abbreviated CH<sup>E</sup><sub>3-asy</sub>), on the other hand, shows no significant increase in amplitude with increasing chain length. The amplitude of the CH<sub>3-sym</sub> signal, like CH<sup>E</sup><sub>3-asy</sub>, does not show any increase/ decrease with the increase in chain lengths but only a small zig-zag oscillation (**Fig. 5.3c**).

Interestingly, not only are the trends for  $\text{CH}_3^{\text{E}}_{3\text{-asy}}$  and  $\text{CH}_3\text{-sym}$  similar, but the magnitude of their signal amplitude is also comparable (**Fig. 5.3c**). For the  $\text{Au}^{\text{AD}}$ , however, no statistically significant zig-zag oscillations in the amplitude of the respective signal were observed (**Fig. 5.3d**). The magnitude of the amplitude for all peaks of interest ranges from 1 to 2, akin to  $\text{CH}_3^{\text{E}}_{3\text{-asy}}$  and  $\text{CH}_3\text{-sym}$ .

As shown in the Supporting Information, and as discussed previously,<sup>38, 40, 166-167, 179</sup> the ratio of the  $I_{\text{CH}_3\text{-asy}}/I_{\text{CH}_3\text{-sym}}$  SFG signal intensities strongly increases as a function of tilt angle,  $\theta$ , the angle between the  $\text{C}_3$  axis of methyl and the macroscopic surface normal (**Fig. S5.4**, Supporting Information). Thus the observed dramatic alternation in SFG  $I_{\text{CH}_3\text{-asy}}/I_{\text{CH}_3\text{-sym}}$  (**Fig. 5.3e**) is indicative of a large change in orientation of the terminal  $\text{CH}_3$  group as a function of the number of odd or even carbons in the  $n$ -alkanethiol. The observed zig-zag oscillation in the  $-\text{CH}_3$  signal can be attributed to an ordered interface for SAMs on  $\text{Au}^{\text{TS}}$ , akin to what is schematically illustrated for well-ordered all-trans chains (**Fig. 5.1**). Such an ordered interface must be absent for SAMs on the  $\text{Au}^{\text{AD}}$  surface where no  $I_{\text{CH}_3\text{-asy}}/I_{\text{CH}_3\text{-sym}}$  variation with odd or even chain length is observed (**Fig. 5.3e**).

### 5.3.2 Asymmetry in the odd–even effect

We also observe a small increase in the  $I_{\text{CH}_3\text{-asy}}/I_{\text{CH}_3\text{-sym}}$  ratio for  $\text{SAM}^{\text{O}}$  with increasing molecular length. This observation, albeit of a small magnitude, indicates an asymmetry in the odd–even oscillation with an increase in the molecular length analogous to a similar observation in hydrophobicity.<sup>147, 177</sup> We have previously attributed the

asymmetry in wetting behavior to the changing structure of the SAM, assuming that the SAM becomes more ordered (crystalline) with increasing molecular length. An increase in chain length has also been associated with a decrease in gauche defects and this may lead to significantly larger changes in the local intermolecular environment of the terminal CH<sub>3</sub> group in SAM<sup>O</sup> (where the terminal moiety is oriented towards the molecular tilt axis) than those in SAM<sup>E</sup>—where the terminal moiety is oriented towards the surface normal (**Fig. 5.1a**).

### 5.3.3 *Transition to a more ordered (crystalline) phase*

Changes in the CH<sub>3</sub> asymmetric SFG peak width on both surfaces as a function of molecular length are also consistent with changes in the local chemical environment of the terminal CH<sub>3</sub> moiety, which is related to the strength of intermolecular interactions. By letting the width be a fitting parameter for the strongest band in the SFG spectra, odd–even dependent oscillations were found for the widths of the CH<sub>3</sub> asymmetric stretch for SAMS on the Au<sup>TS</sup> surface (**Fig. 5.3f**). The difference in the width is attributed to the differences in the local chemical environments for the terminal CH<sub>3</sub> group. Assuming that these widths are predominantly homogenous in origin, consistent with the excellent fits to Lorentzian line shapes, the odd-numbered molecules have broader widths corresponding to faster dephasing times compared to the even-numbered alkanethiols on Au<sup>TS</sup> substrates. In this homogeneous line-broadening limit, the spectral width is  $\sim\tau_c\Delta^2$  where  $\tau_c$  is a fluctuation timescale and  $\Delta$  is the initial spectral breadth of transition frequencies.<sup>180-</sup>  
<sup>182</sup> These observations indicate that different chemical environments are operative in SAMs from the two types of surfaces. Variation in the local chemical environments of

CH<sub>3</sub> results in odd–even trends on both surfaces, a phenomenon that has not been previously reported. We observe that the odd–even oscillation in peak width is limited to SAMs with  $\leq C_{12}$  while there is a slight decline in peak width for  $\geq C_{14}$  SAMs. We infer that since this change, from an odd–even oscillation to a linear decline, is due to changes in the local environment of the CH<sub>3</sub> moiety, it indicates that either (i) the total number of degrees of rotational/conformational freedom—as manifested in the gauche defects—are significantly declining leading to a more uniform molecular orientation, or (ii) the structural properties<sup>149, 183</sup> of these SAMs could be significantly different and thus this line width effect results from this structural transition akin to a phase change in bulk materials. Gauche defects are known to decrease with an increase in molecular length, with the prediction that they are absent for SAM with  $>C_{14}$ .<sup>149</sup> Although a decrease in defects could lead to a more ordered SAM, this could manifest in a change in the amplitude of the SFG signal and a uniform change in the peak with the decline in defects. What we observe are two different trends in the change in peak width, *viz.*, an odd–even oscillation and a linear decline without an accompanying odd–even oscillation. We hypothesize that this could be due to the  $\leq C_{12}$  SAMs being ‘waxy’ (transition between liquid and solid) while an increase in chain length induces a transition to a more solid-like SAM with an increase in the number of inter-chain van der Waals interactions.<sup>183</sup> We also note that this oscillation in peak width is observed in both Au<sup>TS</sup> and Au<sup>AD</sup> suggesting that unlike the amplitude, peak width is dominated by local intermolecular effects. Of note, however, is the fact that the values of peak width for C<sub>10</sub> and C<sub>12</sub> on a smooth surface are generally larger than those of C<sub>9</sub> and C<sub>11</sub>, which indicates that the

intermolecular environment of  $\text{CH}_3$  in  $\text{SAM}^{\text{O}}$  generally has larger interactions than that in  $\text{SAM}^{\text{E}}$ . This correlates well with our observations in SAM wetting.<sup>183</sup> However, more data are needed to further confirm this interpretation. The trend in peak width offers the first SFG-derived evidence for the transition of SAMs to a solid-like phase with increasing chain length, and allows us to predict that a transition occurs at or around  $\text{C}_{13}$ —an observation that correlates well with anomalies observed in other properties of  $\text{C}_{13}$  SAMs.<sup>147, 151</sup> Subsequent studies are required to substantiate this initial inference.

The odd–even effect in oleophilicity on rough surfaces can be associated with the changing intermolecular chemical environment of the terminal moiety. In a recent manuscript,<sup>177</sup> we observed that unlike with hydrophobicity, the oleophilicity of the  $\text{C}_{10}$ – $\text{C}_{16}$  SAMs showed an odd–even oscillation irrespective of substrate roughness. This rather puzzling result suggests that when the contact is favorable, the probe liquids respond to more than just the orientation of the most exposed group. In the current study, we observed that while the odd–even oscillation in the orientation of the terminal moiety is affected by substrate roughness (i.e. amplitude of the SFG signal), the local chemical environment, as deduced from peak width, shows an odd–even oscillation irrespective of the surface roughness. We infer that with the wetting liquid the observed odd–even oscillation is likely due to a response to the changing conformational order of the molecules associated with changes in the local intermolecular chemical environment of the terminal  $\text{CH}_3$  group which manifests as an odd–even oscillation in the SFG peak width. We can therefore infer that hydrophobicity is dominated by the orientation of the surface exposed moiety, which is dependent on the quality of the substrate, while

oleophilicity is dependent on both the orientation of the terminal moiety and the length-dependent changes in the structure of the SAM irrespective of surface roughness.

### 5.3.4 *Fe and Cu doped Au substrates*

In addition to the Au<sup>TS</sup> and Au<sup>AD</sup> substrates, the odd-even effect on  $R_{\text{RMS}} = 0.20$  nm Au<sup>Fe</sup> (Fe-doped Au) and  $R_{\text{RMS}} > 0.40$  nm Au<sup>Cu</sup> (Cu-doped Au) substrates was investigated in an attempt to determine the minimum roughness at which odd-even oscillations can be detected. The odd-even trend observed on Au<sup>Fe</sup> and Au<sup>Cu</sup> follows the same trend that was observed on Au<sup>TS</sup>. That is, odd-numbered alkanethiol SAMs have larger CH stretching SFG intensities than even-numbered SAMs, however there are differences in the oscillation magnitudes (**Fig. 5.4**). For Au<sup>Fe</sup> the oscillations in amplitude values agree with observations of the SFG spectra. The CH<sub>3</sub> asymmetric stretching amplitudes are higher magnitude and show a clear odd-even oscillation, while the CH<sub>3</sub> symmetric stretching amplitudes do not exhibit a trend (**Fig. 5.4b**). This is similar to what is observed for Au<sup>TS</sup> and Au<sup>Cu</sup> substrates (**Fig. 5.4d and f**), however the magnitude of the oscillation decreases with increasing surface roughness. This is clearly seen in Au<sup>AD</sup> ( $R_{\text{RMS}} = 2.38$  nm) where no odd-even effect is observed.

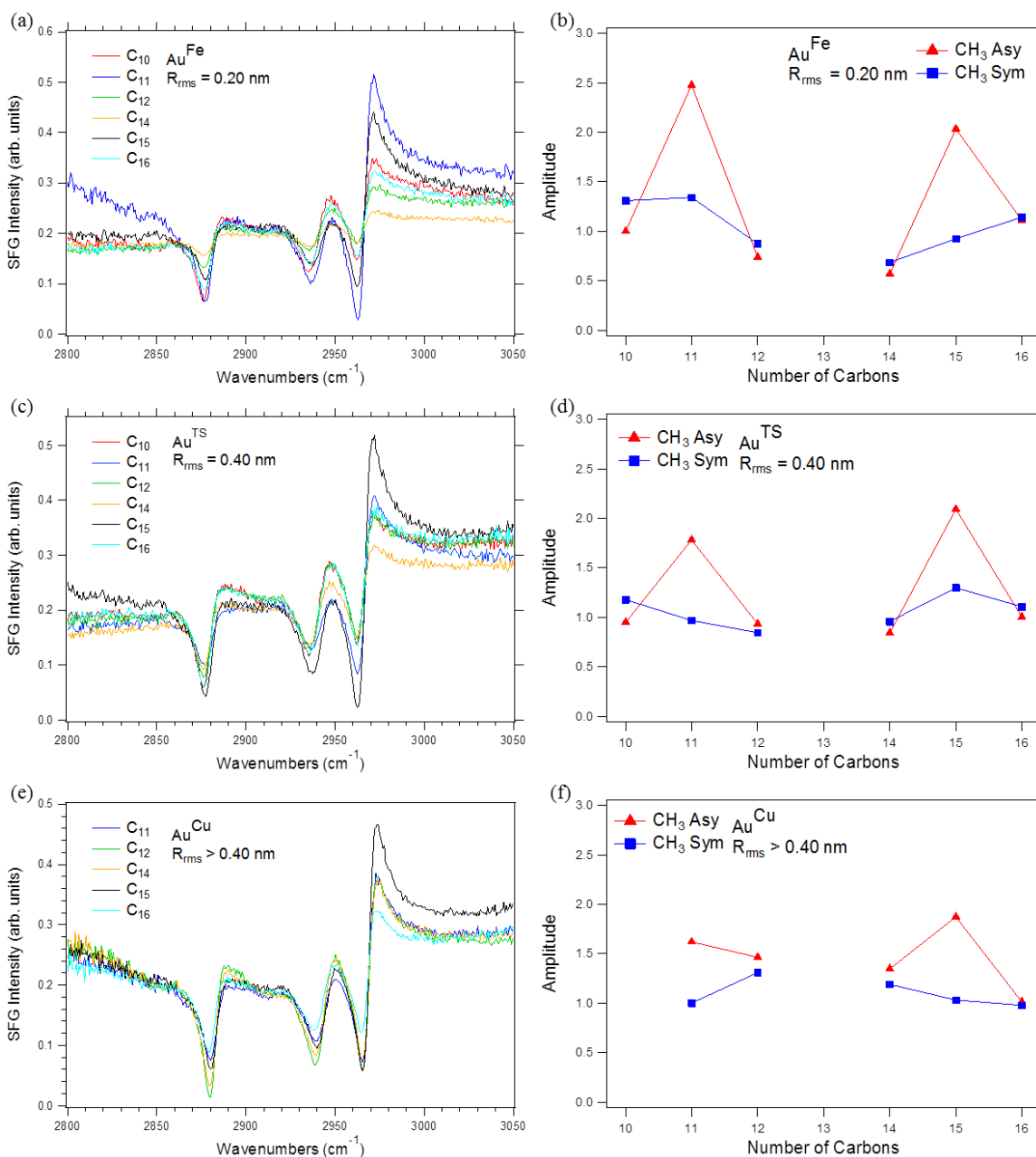


**Figure 5.4: Summary of SFG spectroscopic data. SFG spectra in the CH stretching region for (a) Au<sup>Fe</sup>, (c) Au<sup>TS</sup>, and (e) Au<sup>Cu</sup>. Oscillations in the CH<sub>3</sub> asymmetric stretching mode (red triangles) are observed for all substrates. A decrease of odd-even oscillation is shown for (f) Au<sup>Cu</sup> relative to (b) Au<sup>Fe</sup> and (d) Au<sup>TS</sup>. No oscillations are seen in the CH<sub>3</sub> symmetric stretching mode (blue squares).**

To highlight the change in magnitude of the odd-even oscillation for SAMs on Au substrates with different roughness ( $R_{RMS}$ ),  $I_{CH_3-asym}/I_{CH_3-sym}$  was plotted as a function of the

carbon chain length (**Fig. 5.5**) as described in the previous sections. Across all surface roughness, the intensity ratio for even-numbered SAMs is constant, whereas the intensity ratio for odd-numbered SAMs varies as a function of  $R_{\text{RMS}}$ . Since the intensity ratio oscillation for  $\text{Au}^{\text{Fe}}$  and  $\text{Au}^{\text{TS}}$  is roughly the same, we can infer that surfaces smoother than  $R_{\text{RMS}} = 0.40$  nm will not enhance *n*-alkanethiol SAM odd-even behavior in SFG studies. Therefore, at a surface roughness of 0.20 nm ( $\text{Au}^{\text{Fe}}$ ) the ordering and structure of SAMs is going to be equivalent to that of  $\text{Au}^{\text{TS}}$ . As seen in **Figure 5.5**, the odd-even oscillation magnitude for  $\text{Au}^{\text{Cu}}$  is significantly lower compared to  $\text{Au}^{\text{TS}}$  and  $\text{Au}^{\text{Fe}}$ . This is attributed to the rougher surface of  $\text{Au}^{\text{Cu}}$ , which has been shown to reduce the CH stretching odd-even oscillation.

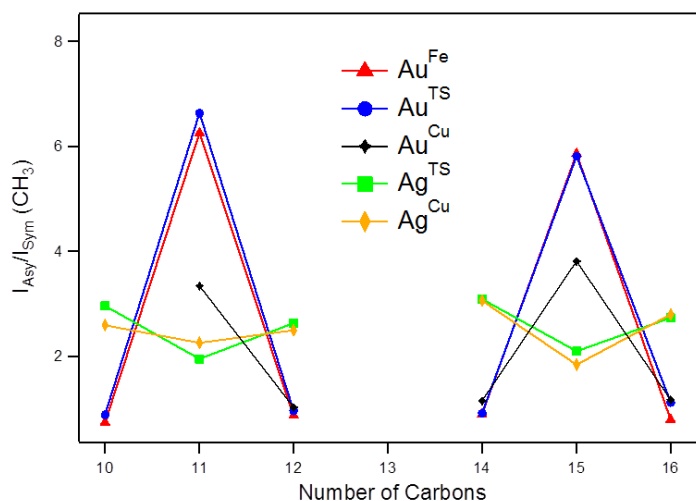


**Figure 5.5:**  $\text{CH}_3$  asymmetric-symmetric stretching ratio for *n*-alkanethiol SAMs deposited on metal substrates. A clear odd-even oscillation is observed for  $\text{Au}^{\text{Fe}}$  (red) and  $\text{Au}^{\text{TS}}$  (blue). The odd-even oscillation is reduced for the rougher  $\text{Au}^{\text{Cu}}$  (black) surface, while no significant odd-even oscillations are observed on  $\text{Ag}^{\text{TS}}$  (green), and  $\text{Ag}^{\text{Cu}}$  (orange) surfaces.

### 5.3.5 Ag substrates

On Ag substrates, the orientation of the terminal CH<sub>3</sub> methyl group is opposite relative to Au substrates. Alkanethiols with odd-numbered carbons orient the terminal methyl group perpendicular to the surface, whereas in even-numbered alkanethiols, the methyl group is at an angle to the surface (**Fig. 5.6**). The difference in orientation relative to Au substrates arises due to the differences in metal-sulfur-carbon bond angle on Ag and Au. The Ag-S-C bond is 180°, due to the *sp* hybridization of the sulfur atom, while the Au-S-C bond angle is ~105° because the sulfur is *sp*<sup>3</sup> hybridized in this environment.

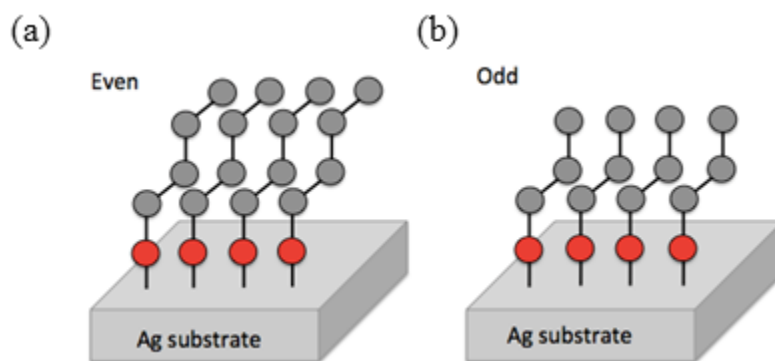


**Figure 5.6: Self-assembled monolayers on Ag substrates. (a) The terminal methyl group is tilted relative to the surface normal for even-numbered alkanethiols and (b) perpendicular to the substrate surface in odd-numbered alkanethiols.**

Due to the change in methyl group orientation, the odd-even oscillation observed on Ag substrates is reversed relative to what is observed on Au substrates. Even-numbered alkanethiols show larger amplitudes and intensity ratios compared to the odd-numbered alkanethiols (**Fig. 5.7**). No obvious odd-even oscillation is observed in the SFG spectra for both Ag<sup>TS</sup> and Au<sup>Cu</sup> (Cu-doped silver) substrates, as shown in **Figure 5.7 a and 5.7c**. For Ag<sup>TS</sup> ( $R_{\text{RMS}} = 0.70$  nm) the CH<sub>3</sub> symmetric stretching amplitudes show no odd-even oscillation, analogous to what is observed for Au substrates (**Fig. 5.4**). The CH<sub>3</sub>

asymmetric stretching amplitudes show a slight odd-even oscillation that appears non-symmetric about  $C_{13}$ . That is, the odd-even oscillation magnitude is greater for  $C_n < C_{13}$  compared to chain lengths  $> C_{13}$ . The odd-even effect observed on  $\text{Au}^{\text{Cu}}$  ( $R_{\text{RMS}} = 1.90$  nm) is slightly different, with both the symmetric and asymmetric stretching amplitudes showing minor odd-even oscillations (**Fig. 5.7d**). However, no significant odd-even oscillation in  $I_{\text{CH}_3\text{-asy}}/I_{\text{CH}_3\text{-sym}}$  is observed for SAMs on Ag substrates (**Fig. 5.5**).

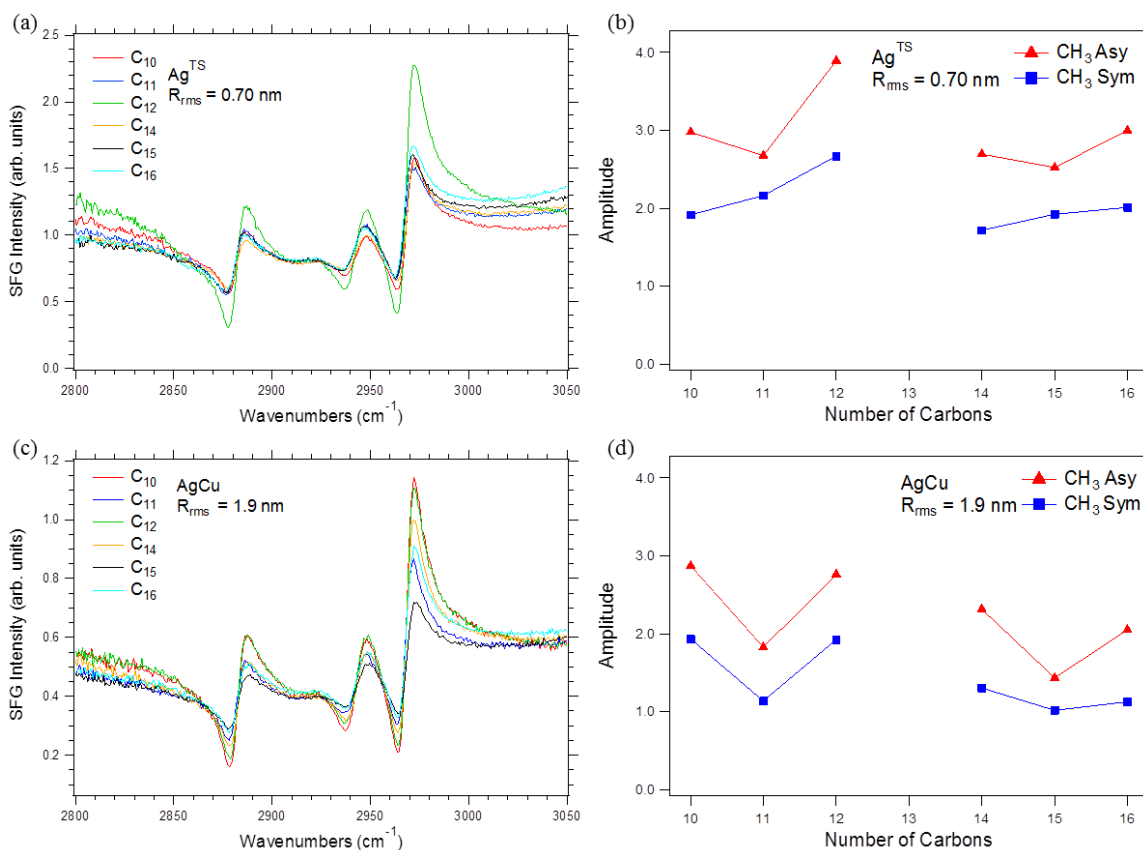


**Figure 5.7:** SFG spectra in the CH stretching region of (a)  $\text{Ag}^{\text{TS}}$  and (c)  $\text{Ag}^{\text{Cu}}$ . Plots of amplitude as a function of carbon chain length for the  $\text{CH}_3$  asymmetric (red) and symmetric (blue) stretching modes for (b)  $\text{Ag}^{\text{TS}}$  and (d)  $\text{Ag}^{\text{Cu}}$ .

There are two possible explanations for the reduced odd-even oscillation observed on Ag substrates. First, the roughness ( $R_{\text{RMS}}$ ) of Ag substrates much greater than that of

$Au^{TS}$  being nearly two times greater for  $Ag^{TS}$  and nearly five times rougher for  $Ag^{Cu}$ . As we have shown above, the odd-even effect is reduced with rougher surfaces. Another possible explanation for the reduced odd-even effect observed could be due to the effect that the Ag-S-C bond angle has on the alkanethiol SAM packing. Since the bond Ag-S-C bond angle is  $180^\circ$  (pointed straight up, perpendicular to the substrate surface), this could allow for *better* packing of the SAM. This is evidenced by greater amplitudes observed for  $SAM^E$  on Ag substrates compared to  $SAM^O$  on Au substrates. In both cases the terminal methyl group is oriented upward so the observed differences in amplitude are attributed to a higher number density on Ag substrates. Thus, the SAMs are packed better on Ag relative to Au. For this reason, it is possible that steric effects reduce the tilting of the terminal methyl group for  $SAM^O$  on Ag substrates, leading to the reduced odd-even oscillations that are observed (**Fig. 5.5**).

#### 5.4 Conclusions

This study captures the effect of substrate roughness on the SAM structure through signal amplitude and peak width from the sum-frequency generation spectroscopic study. From the data and discussions above, we infer the following.

*Surface morphology significantly affects SAM order*

Surface morphology, including  $R_{RMS}$ , grain size and percentage of surface coverage can highly affect the overall order of the SAM, which in turn affects the orientation of the terminal groups, leading to differences in interfacial properties of the SAM.

*Absence of an odd–even effect in hydrophobicity on rough surfaces is associated with lack of SAM order*

This study provides spectroscopic evidence that the previously reported absence of an odd–even effect in hydrophobicity of SAMs on a rough surface (Au<sup>AD</sup>) with water is likely due to the lack of SAM order,<sup>148, 177</sup> hence, there are no differences in the orientation of the terminal CH<sub>3</sub> groups.

*Odd–even effects in SAMs not only depend on the orientation of the terminal moiety but also on its evolving changes in the local intermolecular chemical environment*

By comparing the changes in the signal amplitude and the ratio of the symmetric and asymmetric CH<sub>3</sub> stretches, we observe a clear odd–even oscillation in the orientation of the terminal CH<sub>3</sub> moiety. Similarly, by comparing the changes in the respective peak-widths at half-height, we observe that there is a significant odd–even oscillation in the local intermolecular environment of the CH<sub>3</sub> probe moiety. This demonstrates that the odd–even effect in self-assembled monolayers is not just due to the structural orientation of the terminal moiety, a significant contribution also arises from the changing local chemical environment. This chemical environment effect could be due to structural changes resulting from a decrease in gauche defects, length dependent changes in conformation of the molecule, or a length dependent structural phase transition. These findings may be informative to SAM-based studies that are highly dependent on inter-chain interactions.<sup>184-185</sup>

*The odd–even (zig-zag) oscillation in the orientation (signal amplitude) of the CH<sub>3</sub> moiety is asymmetric*

After observing a clustering of the signal amplitude of the CH<sub>3-asy</sub> peaks into odds and evens, we observed that while the even-numbered SAMs almost showed no change in the absolute amplitude, the odd-numbered cluster showed a gradual increase in intensity. This is due to an asymmetry in the zigzag oscillation with changes from a preceding even-to-odd transition being smaller than the following odd-to-even transition (that is,  $|\Delta I_{\text{CH}_3\text{Asy}}^{\text{E}\rightarrow\text{O}}| < |\Delta I_{\text{CH}_3\text{Asy}}^{\text{O}\rightarrow\text{E}}|$ ). This asymmetry is analogous to the one observed in the wetting properties of the SAM, where odd–even oscillations in static contact angles were observed to be analogously asymmetric (that is,  $|\Delta\theta_s^{\text{E}\rightarrow\text{O}}| < |\Delta\theta_s^{\text{O}\rightarrow\text{E}}|$ ).<sup>147</sup> We can therefore infer that the increase in the origin of asymmetry in the SFG signal is closely associated with that in the hydrophobicity of the SAM. We had previously inferred, and now confirm, that the asymmetry in the hydrophobicity odd–even oscillation is due to the decrease in the dispersive component of the SAM surface energy due to the increase in SAM order.

*There is a potential phase change in SAM structure at ~C<sub>13</sub> chain length*

We observe that odd–even oscillations in peak width change at/or around the C<sub>13</sub> chain length. The odd–even oscillation disappears and a linear decay in the peak width for the CH<sub>3-asy</sub> peak is observed. This drastic change in behavior, and on both smooth and rough surfaces, indicates that the molecules are likely to crystallize upon attachment to the substrate. The decrease in peak width for longer chains indicates that the local environment of the terminal moiety is tending towards uniformity—that is, the chemical

environment is tending towards being similar either due to an actual similarity in the environment or an averaged stochastic environment. Irrespective of the origin to the changes in peak width, we can infer that SAMs from C<sub>10</sub> to C<sub>12</sub> are different from those derived from  $\geq$ C<sub>14</sub> *n*-alkanethiols. In terms of the structure of SAMs and their corresponding behaviors, which are discussed in an upcoming report, we confirm that the  $\geq$ C<sub>14</sub> SAMs are crystalline while the C<sub>10</sub>–C<sub>12</sub> are not, although this region may be the transition zone from liquid-like to crystalline.<sup>183</sup>

## 5.5 Supporting Information

### 5.5.1 Fittings of SFG spectra

The intensity of sum-frequency generation (SFG) signal,  $I_{SFG}$ , can be expressed as

$$I_{SFG} \propto \left| \chi_{NR}^{(2)} + \sum_q \chi_q^{(2)} \right|^2 I_{800} I_{IR} \quad (S5.1)$$

where  $I_{800}$  and  $I_{IR}$  are the intensities of the incident 800 nm and IR beams.  $\chi_{NR}^{(2)}$  and  $\chi_q^{(2)}$  represent the complex second order susceptibilities of a non-resonant background term and the vibrationally resonant sum frequency term, respectively. The vibrationally resonant term,  $\chi_q^{(2)}$ , can be expressed as<sup>105</sup>

$$\chi_q^{(2)} \propto \frac{A_q}{\omega_{IR} - \omega_q + i\Gamma_q} \quad (S5.2)$$

where  $\omega_{IR}$  is the frequency of the incident IR beam.  $A_q$ ,  $\omega_q$  and  $2\Gamma_q$  are the amplitude, the frequency and the line-width (FWHM) of the vibrational transition. The amplitude,  $A_q$ , is non-zero only if both the Raman and infrared transitions are allowed. Hence, the resonant term dominates the intensity of the SFG signal when  $\omega_{IR}$  is resonant with a surface vibrational mode that is both Raman and infrared active. Thus, neglecting cross terms and

background contributions, the SFG relative intensity at the peak of the vibration resonance of two vibrational modes 1 and 2 is given by:

$$\frac{I_1}{I_2} = \left| \frac{A_1/\Gamma_1}{A_2/\Gamma_2} \right|^2 \quad (\text{S5.3})$$

SFG spectra are fitted with Eq. 1S to obtain all spectral parameters. Examples of best fits results to representative spectra on Au<sup>TS</sup> and Au<sup>AD</sup> surfaces for an odd and even number carbon alkanethiol are shown in **Figures S5.1 and S5.2**. The relative contributions of the different vibrational resonances to these spectra are shown with peak frequencies and relative intensities indicated.

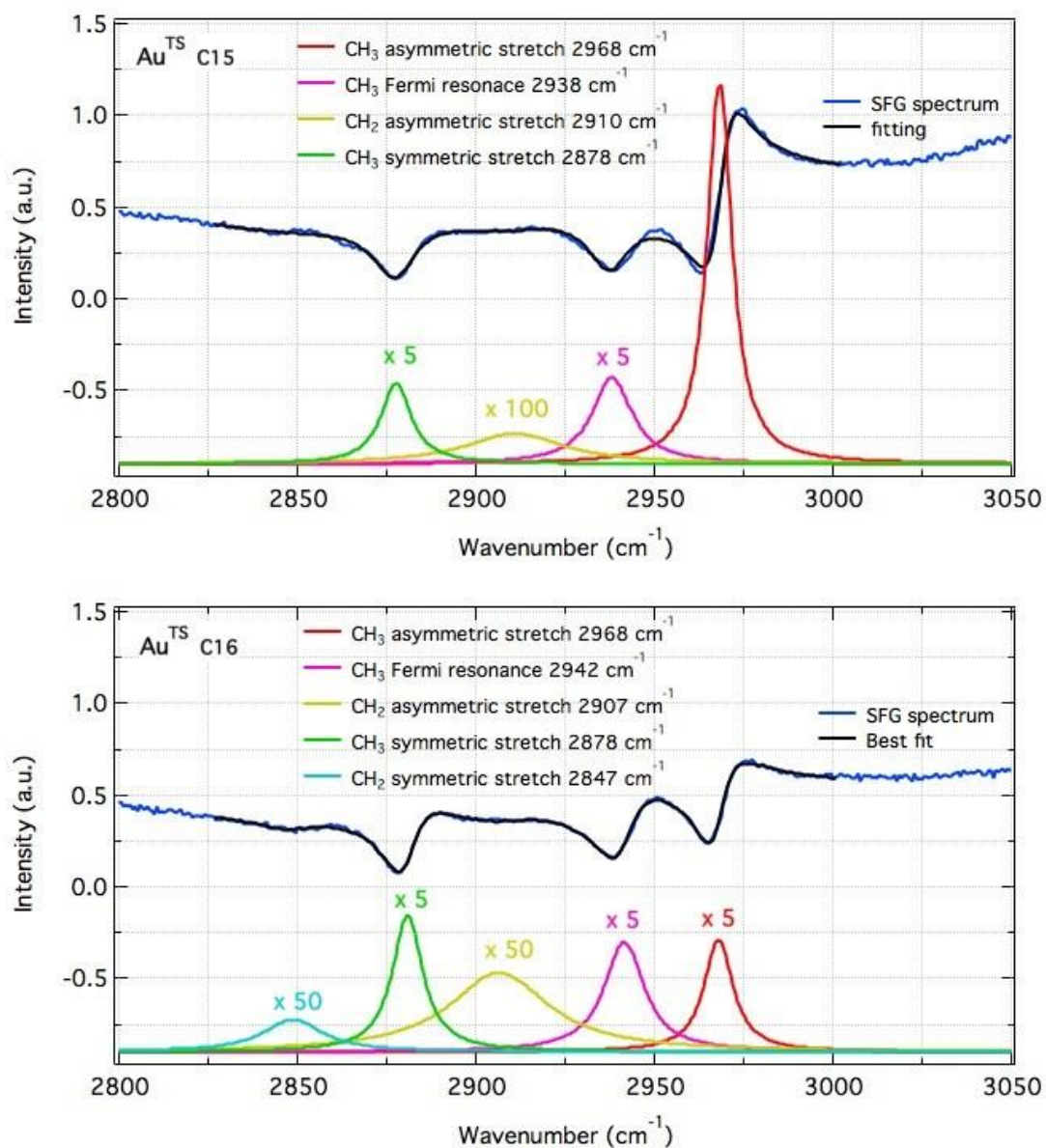


**Figure S5.1: Fitting curves for SFG spectra of pentadecanethiolate (C<sub>15</sub>) and hexadecanethiolate (C<sub>16</sub>) SAMs fabricated on Au<sup>TS</sup> surfaces.**

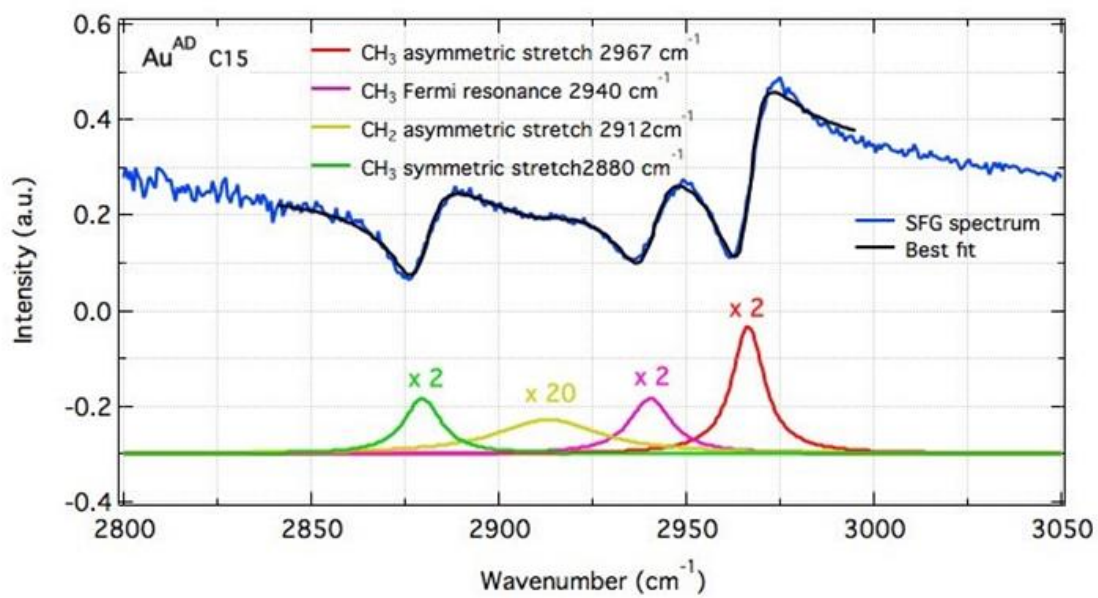


**Figure S5.2: Fitting curve for SFG spectra of pentadecanethiolate (C<sub>15</sub>).**

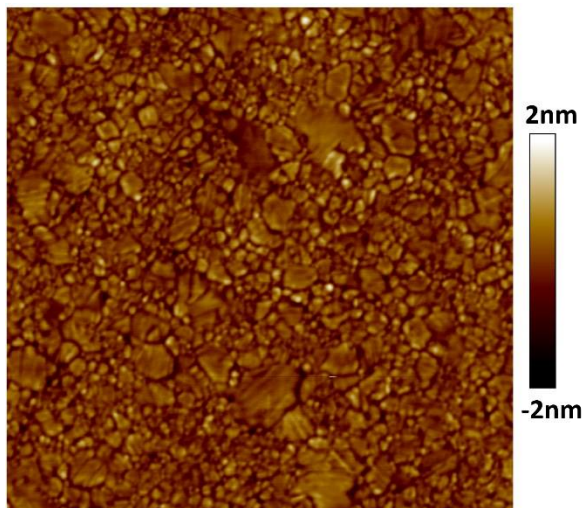


**Figure S5.3: A zoomed-in AFM image of the Au<sup>TS</sup> surface showing the grains and grain boundaries. Although these surfaces are not atomically flat, they have very small asperities and grain sizes.**

### 5.5.2 Calculations for the dependence of SFG intensity on the tilting angle

The intensity of the sum frequency generation signal at  $\omega_{SF}$  in the reflected or transmitted direction,  $I(\omega_{SF})$ , is given by

$$I(\omega_{SF}) \propto |\chi_{eff}^{(2)}|^2 I(\omega_{vis}) I(\omega_{IR}) \quad (S5.4)$$

where  $I(\omega_{vis})$  and  $I(\omega_{IR})$  are the intensities of the incident visible and IR laser beams, respectively. Here we will only be considering the SFG signal in the reflected direction.

The effective second order susceptibility,  $\chi_{eff}^{(2)}$ , defined further below is proportional to the macroscopic susceptibility tensors,  $\chi_{ijk}^{(2)}$ , where  $i, j$ , and  $k$  correspond to the laboratory fixed frame.  $\chi_{ijk}^{(2)}$  is related to the molecular hyperpolarizability  $\beta_{i'j'k'}^{(2)}$  by

$$\chi_{ijk}^{(2)} = N_s \sum_{i'j'k'} \langle R_{ii'} R_{jj'} R_{kk'} \rangle \beta_{i'j'k'}^{(2)} \quad (S5.5)$$

where  $N_s$  is the vibrator number density at the interface and  $i', j'$ , and  $k'$  could be  $a, b$ , or  $c$  in the molecular coordinate system.  $R_{\lambda\lambda'}$  is the element of the Euler rotational

transformation matrix that converts the molecular coordinate system  $\lambda'(a,b,c)$  to the laboratory fixed frame  $\lambda(x,y,z)$ .

The SFG signal strength is thus strongly dependent on the number density and molecular orientation at the surface (Eqs. 4S and 5S). Since SFG signals are generated by the same alkanethiol molecules on both deposited and template-stripped gold surfaces,  $\beta_{i'j'k'}^{(2)}$  is a constant when comparing the relative SFG intensities on these two surface types and thus, the main difference in the relative SFG signal strengths must be due to different orientations and/or different number of molecules on these surfaces.

For a rotationally isotropic interface ( $C_{\infty v}$ ), the distinct polarization dependent  $\chi_{eff}^{(2)}$  elements can be expressed in terms of specific experimental geometry configurations

$$\begin{aligned} \chi_{ppp}^{(2),eff} = & -L_{xx}(\omega_{SFG})L_{xx}(\omega_{vis})L_{zz}(\omega_{IR}) \cos \theta_{SFG} \cos \theta_{vis} \sin \theta_{IR} \chi_{xxz}^{(2)} \\ & -L_{xx}(\omega_{SFG})L_{zz}(\omega_{vis})L_{xx}(\omega_{IR}) \cos \theta_{SFG} \sin \theta_{vis} \cos \theta_{IR} \chi_{xzx}^{(2)} \\ & +L_{zz}(\omega_{SFG})L_{xx}(\omega_{vis})L_{xx}(\omega_{IR}) \sin \theta_{SFG} \cos \theta_{vis} \cos \theta_{IR} \chi_{zxx}^{(2)} \\ & +L_{zz}(\omega_{SFG})L_{zz}(\omega_{vis})L_{zz}(\omega_{IR}) \sin \theta_{SFG} \sin \theta_{vis} \sin \theta_{IR} \chi_{zzz}^{(2)}. \end{aligned} \quad (S5.6)$$

where  $\theta$  is the reflected angle of each beam with respect to the surface normal. In the laboratory coordinates  $\lambda(x,y,z)$ , all light beams propagate in the  $xz$  plane, which is perpendicular to the surface  $xy$  plane, with  $z$  as the surface normal direction.  $L_{ii}(\omega)$  is the diagonal element of the Fresnel factor at frequency  $\omega$  (where  $\omega = \omega_{SFG}$ ,  $\omega_{vis}$  or  $\omega_{IR}$ ) defined by

$$\begin{aligned} L_{xx}(\omega) &= \frac{2n_1(\omega) \cos \gamma}{n_1(\omega) \cos \gamma + n_2(\omega) \cos \beta} \\ L_{yy}(\omega) &= \frac{2n_1(\omega) \cos \theta}{n_1(\omega) \cos \theta + n_2(\omega) \cos \gamma} \end{aligned}$$

$$L_{zz}(\omega) = \frac{2n_1(\omega) \cos \theta}{n_1(\omega) \cos \gamma + n_2(\omega) \cos \theta} \left( \frac{n_1(\omega)}{n'(\omega)} \right)^2 \quad (\text{S5.7})$$

where  $n_1(\omega)$ ,  $n_2(\omega)$ , and  $n'(\omega)$  are the refractive index of air, water, and the interface (the average of  $n_1$  and  $n_2$ ), respectively, at frequency  $\omega$ , and  $\gamma$  is the refracted angle for each beam.

Given the  $C_{3v}$  symmetry of the methyl group, there are 11 nonzero microscopic SFG hyperpolarizability elements for the methyl C-H vibrations.<sup>40</sup> With  $c$  along the  $C_3$  axis of the methyl group, and the perpendicular  $a$  and  $b$  axes defined with the  $a$  axis along the projection of one C-H bond. For the symmetric stretching (ss) mode the nonzero hyperpolarizability elements are  $\beta_{ccc}^{(2)}$  and  $\beta_{aaa}^{(2)} = \beta_{bbc}^{(2)}$ , and correspondingly, for the asymmetric stretching (as) mode, the nonzero elements are  $\beta_{aca}^{(2)} = \beta_{bcb}^{(2)}$ ,  $\beta_{caa}^{(2)} = \beta_{cbb}^{(2)}$ , and  $\beta_{aaa}^{(2)} = -\beta_{bba}^{(2)} = -\beta_{abb}^{(2)} = -\beta_{bab}^{(2)}$ . Thus, if  $\theta$  is defined as the angle between the  $C_3$  axis of methyl and macroscopic surface normal, the  $\chi_{ijk}^{(2)}$  elements are then given by,<sup>40</sup>

$$\begin{aligned} \chi_{xxz}^{(2),ss} &= \chi_{yyz}^{(2),ss} = \frac{1}{2} N_s \beta_{ccc}^{(2)} [(1+R)\langle \cos \theta \rangle - (1-R)\langle \cos^3 \theta \rangle] \\ \chi_{xzx}^{(2),ss} &= \chi_{zxx}^{(2),ss} = \chi_{yzy}^{(2),ss} = \chi_{zyy}^{(2),ss} = \frac{1}{2} N_s \beta_{ccc}^{(2)} (1-R) [\langle \cos \theta \rangle - \langle \cos^3 \theta \rangle] \\ \chi_{zzz}^{(2),ss} &= N_s \beta_{ccc}^{(2)} [\langle \cos \theta \rangle + (1-R)\langle \cos^3 \theta \rangle] \\ \chi_{xxz}^{(2),as} &= \chi_{yyz}^{(2),as} = -N_s \beta_{aca}^{(2)} [\langle \cos \theta \rangle - \langle \cos^3 \theta \rangle] \\ \chi_{xzx}^{(2),as} &= \chi_{zxx}^{(2),as} = \chi_{yzy}^{(2),as} = \chi_{zyy}^{(2),as} = N_s \beta_{aca}^{(2)} \langle \cos^3 \theta \rangle \\ \chi_{zzz}^{(2),as} &= 2N_s \beta_{aca}^{(2)} [\langle \cos \theta \rangle - \langle \cos^3 \theta \rangle] \end{aligned} \quad (\text{S5.8})$$

where the ratio  $R = \beta_{aac}^{(2)}/\beta_{ccc}^{(2)}$ . From the above expressions (Equations S5.4-S5.8) the ratio of the SFG intensity of the asymmetric/symmetric stretch bands on Au as a function of the tilting angle  $\theta$  can be calculated and is shown in **Figure S5.4** for  $R=1$  and

$\beta_{aac}^{(2)}/\beta_{ccc}^{(2)} = 1$ . The exact values do not change the shape of the intensity ratio shown in

**Figure S5.4**, just the absolute value of this quantity.

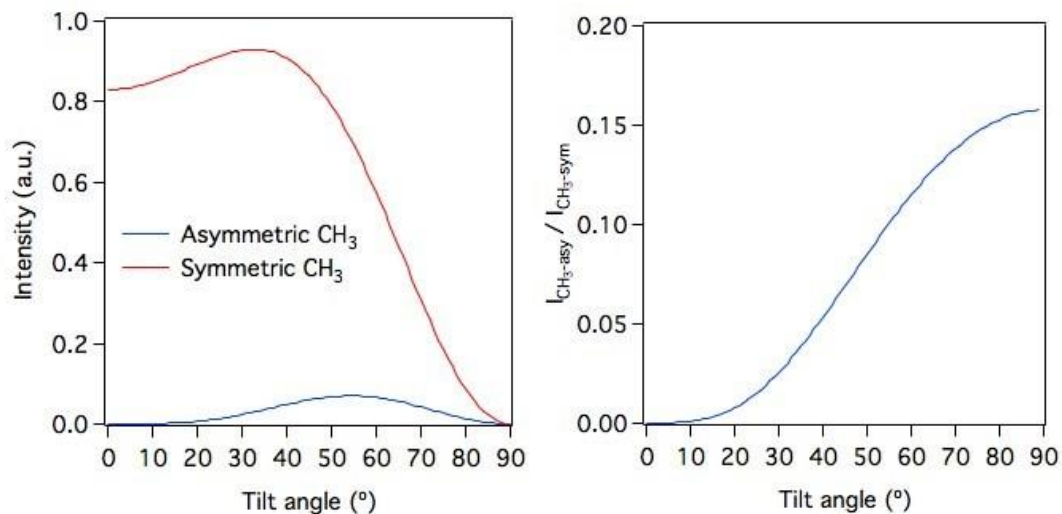


**Figure S5.4:** The dependence of SFG intensities of symmetric and asymmetric stretch of CH<sub>3</sub> on the tilt angle  $\theta$  on gold surface.

## REFERENCES

1. Berkowitz, M. L.; Bostick, D. L.; Pandit, S., Aqueous Solutions next to Phospholipid Membrane Surfaces: Insights from Simulations. *Chemical Reviews*. **2006**, *106* (4), 1527-1539.
2. Chung, S.-H.; Anderson, O. S.; Krishnamurthy, V. V., *Biological Membrane Ion Channels: Dynamics, Structure, and Applications*. 1st ed.; Springer-Verlag: New York, 2007; p 658.
3. Lodish, H.; Berk, A.; Zipursky, S. L.; Matsudaira, P.; Baltimore, D.; Darnell, J., *Molecular Cell Biology*. 4th ed.; W. H. Freeman: New York, 2000.
4. Creuwels, L. A.; van Golde, L. M.; Haagsman, H. P., The pulmonary surfactant system: biochemical and clinical aspects. *Lung* **1997**, *175* (1), 1-39.
5. Patton, J. S., Mechanisms of macromolecule absorption by the lungs. *Advanced Drug Delivery Reviews* **1996**, *19* (1), 3-36.
6. Patton, J. S.; Byron, P. R., Inhaling medicines: delivering drugs to the body through the lungs. *Nature Reviews Drug Discovery* **2007**, *6*, 67.
7. Jubb, A. M.; Hua, W.; Allen, H. C., Environmental chemistry at vapor/water interfaces: insights from vibrational sum frequency generation spectroscopy. *Annual Review of Physical Chemistry*. **2012**, *63*, 107-30.
8. Finlayson-Pitts, B.; Pitts, J., *Chemistry of the Upper and Lower Atmosphere: Theory, Experiments, and Applications*. Academic: San Diego, 2000; p 969.
9. CHARLSON, R. J.; SCHWARTZ, S. E.; HALES, J. M.; CESS, R. D.; COAKLEY, J. A.; HANSEN, J. E.; HOFMANN, D. J., Climate Forcing by Anthropogenic Aerosols. *Science* **1992**, *255* (5043), 423-430.
10. Ångström, A., On the Atmospheric Transmission of Sun Radiation and on Dust in the Air. *Geografiska Annaler* **1929**, *11*, 156-166.
11. Richmond, G. L., Molecular Bonding and Interactions at Aqueous Surfaces as Probed by Vibrational Sum Frequency Spectroscopy. *Chemical Reviews*. (Washington, DC, U. S.) **2002**, *102* (8), 2693-2724.
12. Tarbuck, T. L.; Richmond, G. L., Adsorption and Reaction of CO<sub>2</sub> and SO<sub>2</sub> at a Water Surface. *Journal of the American Chemical Society*. **2006**, *128* (10), 3256-3267.
13. Levering, L. M.; Sierra-Hernández, M. R.; Allen, H. C., Observation of Hydronium Ions at the Air–Aqueous Acid Interface: Vibrational Spectroscopic Studies of Aqueous HCl, HBr, and HI. *The Journal of Physical Chemistry C* **2007**, *111* (25), 8814-8826.
14. Tian, C.; Ji, N.; Waychunas, G. A.; Shen, Y. R., Interfacial Structures of Acidic and Basic Aqueous Solutions. *Journal of the American Chemical Society*. **2008**, *130* (39), 13033-13039.
15. Shultz, M. J.; Schnitzer, C.; Simonelli, D.; Baldelli, S., Sum frequency generation spectroscopy of the aqueous interface: Ionic and soluble molecular solutions. *International Reviews in Physical Chemistry*. **2000**, *19* (1), 123-153.
16. Allen, H. C.; Raymond, E. A.; Richmond, G. L., Non-linear vibrational sum frequency spectroscopy of atmospherically relevant molecules at aqueous solution surfaces. *Current Opinion in Colloid & Interface Science* **2000**, *5* (1), 74-80.

17. Chen, X.; Minofar, B.; Jungwirth, P.; Allen, H. C., Interfacial Molecular Organization at Aqueous Solution Surfaces of Atmospherically Relevant Dimethyl Sulfoxide and Methanesulfonic Acid Using Sum Frequency Spectroscopy and Molecular Dynamics Simulation. *The Journal of Physical Chemistry B* **2010**, *114* (47), 15546-15553.
18. Blower, P. G.; Shamay, E.; Kringle, L.; Ota, S. T.; Richmond, G. L., Surface Behavior of Malonic Acid Adsorption at the Air/Water Interface. *The Journal of Physical Chemistry A* **2013**, *117* (12), 2529-2542.
19. Miranda, P. B.; Du, Q.; Shen, Y. R., Interaction of water with a fatty acid Langmuir film. *Chemical Physics Letters*. **1998**, *286* (1–2), 1-8.
20. Gragson, D. E.; McCarty, B. M.; Richmond, G. L., Surfactant/Water Interactions at the Air/Water Interface Probed by Vibrational Sum Frequency Generation. *The Journal of Physical Chemistry* **1996**, *100* (34), 14272-14275.
21. Ma, G.; Allen, H. C., DPPC Langmuir Monolayer at the Air–Water Interface: Probing the Tail and Head Groups by Vibrational Sum Frequency Generation Spectroscopy. *Langmuir* **2006**, *22* (12), 5341-5349.
22. Harper, K. L.; Allen, H. C., Competition between DPPC and SDS at the Air–Aqueous Interface. *Langmuir* **2007**, *23* (17), 8925-8931.
23. Muller, M.; Schins, J. M.; Roke, S.; Bonn, M. In *Phase transitions in a lipid monolayer observed with vibrational sum-frequency generation*, Biomedical Optics, SPIE: 2003; p 8.
24. Adamson, A.; Gast, A., *Physical Chemistry of Surfaces*. 6th ed.; John Wiley & Sons, Inc.: New York, 1997; p 784.
25. Mitsui, T.; Rose, M. K.; Fomin, E.; Ogletree, D. F.; Salmeron, M., Water Diffusion and Clustering on Pd(111). *Science* **2002**, *297* (5588), 1850-1852.
26. Cerdá, J.; Michaelides, A.; Bocquet, M. L.; Feibelman, P. J.; Mitsui, T.; Rose, M.; Fomin, E.; Salmeron, M., Novel Water Overlayer Growth on Pd(111) Characterized with Scanning Tunneling Microscopy and Density Functional Theory. *Physical Review Letters*. **2004**, *93* (11), 116101.
27. Tyrrell, J. W. G.; Attard, P., Images of Nanobubbles on Hydrophobic Surfaces and Their Interactions. *Physical Review Letters*. **2001**, *87* (17), 176104.
28. Ghosal, S.; Hemminger, J. C.; Bluhm, H.; Mun, B. S.; Hebenstreit, E. L. D.; Ketteler, G.; Ogletree, D. F.; Requejo, F. G.; Salmeron, M., Electron Spectroscopy of Aqueous Solution Interfaces Reveals Surface Enhancement of Halides. *Science* **2005**, *307* (5709), 563-566.
29. Toney, M. F.; Howard, J. N.; Richer, J.; Borges, G. L.; Gordon, J. G.; Melroy, O. R.; Wiesler, D. G.; Yee, D.; Sorensen, L. B., Voltage-dependent ordering of water molecules at an electrode–electrolyte interface. *Nature* **1994**, *368*, 444.
30. Wilson, K. R.; Schaller, R. D.; Co, D. T.; Saykally, R. J.; Rude, B. S.; Catalano, T.; Bozek, J. D., Surface relaxation in liquid water and methanol studied by x-ray absorption spectroscopy. *The Journal of Chemical Physics* **2002**, *117* (16), 7738-7744.
31. Schwendel, D.; Hayashi, T.; Dahint, R.; Pertsin, A.; Grunze, M.; Steitz, R.; Schreiber, F., Interaction of Water with Self-Assembled Monolayers: Neutron

- Reflectivity Measurements of the Water Density in the Interface Region. *Langmuir* **2003**, *19* (6), 2284-2293.
32. Thompson, K. C.; Jones, S. H.; Rennie, A. R.; King, M. D.; Ward, A. D.; Hughes, B. R.; Lucas, C. O. M.; Campbell, R. A.; Hughes, A. V., Degradation and Rearrangement of a Lung Surfactant Lipid at the Air–Water Interface during Exposure to the Pollutant Gas Ozone. *Langmuir* **2013**, *29* (14), 4594-4602.
33. Shen, Y. R.; Ostroverkhov, V., Sum-frequency vibrational spectroscopy on water interfaces: polar orientation of water molecules at interfaces. *Chemical Reviews*. **2006**, *106* (4), 1140-54.
34. Shen, Y. R., Surface nonlinear optics: a historical perspective. *IEEE Journal of Selected Topics in Quantum Electronics* **2000**, *6* (6), 1375-1379.
35. Eisenthal, K. B., Equilibrium and Dynamic Processes at Interfaces by Second Harmonic and Sum Frequency Generation. *Annual Review of Physical Chemistry*. **1992**, *43* (1), 627-661.
36. Eisenthal, K. B., Liquid Interfaces Probed by Second-Harmonic and Sum-Frequency Spectroscopy. *Chemical Reviews*. **1996**, *96* (4), 1343-1360.
37. Wang, H.-F.; Gan, W.; Lu, R.; Rao, Y.; Wu, B.-H., Quantitative spectral and orientational analysis in surface sum frequency generation vibrational spectroscopy (SFG-VS). *International Reviews in Physical Chemistry*. **2005**, *24* (2), 191-256.
38. Zhuang, X.; Miranda, P. B.; Kim, D.; Shen, Y. R., Mapping molecular orientation and conformation at interfaces by surface nonlinear optics. *Physical Review B* **1999**, *59* (19), 12632-12640.
39. Lu, R.; Gan, W.; Wu, B.-h.; Chen, H.; Wang, H.-f., Vibrational Polarization Spectroscopy of CH Stretching Modes of the Methylene Group at the Vapor/Liquid Interfaces with Sum Frequency Generation. *The Journal of Physical Chemistry B* **2004**, *108* (22), 7297-7306.
40. Lu, R.; Gan, W.; Wu, B.-h.; Zhang, Z.; Guo, Y.; Wang, H.-f., C–H Stretching Vibrations of Methyl, Methylene and Methine Groups at the Vapor/Alcohol (n = 1–8) Interfaces. *The Journal of Physical Chemistry B* **2005**, *109* (29), 14118-14129.
41. Buck, M.; Himmelhaus, M., Vibrational spectroscopy of interfaces by infrared–visible sum frequency generation. *Journal of Vacuum Science & Technology A* **2001**, *19* (6), 2717-2736.
42. Bloembergen, N.; Pershan, P. S., Light Waves at the Boundary of Nonlinear Media. *Physical Review* **1962**, *128* (2), 606-622.
43. Liu, J.; Andino, R. S.; Miller, C. M.; Chen, X.; Wilkins, D. M.; Ceriotti, M.; Manolopoulos, D. E., A Surface-Specific Isotope Effect in Mixtures of Light and Heavy Water. *The Journal of Physical Chemistry C* **2013**, *117* (6), 2944-2951.
44. Stiopkin, I. V.; Jayathilake, H. D.; Weeraman, C.; Benderskii, A. V., Temporal effects on spectroscopic line shapes, resolution, and sensitivity of the broad-band sum frequency generation. *The Journal of Chemical Physics* **2010**, *132* (23), 234503.
45. Vezenov, D. V.; Noy, A.; Rozsnyai, L. F.; Lieber, C. M., Force Titrations and Ionization State Sensitive Imaging of Functional Groups in Aqueous Solutions by Chemical Force Microscopy. *Journal of the American Chemical Society*. **1997**, *119* (8), 2006-2015.

46. Reeve, W.; Erikson, C. M.; Aluotto, P. F., A new method for the determination of the relative acidities of alcohols in alcoholic solutions. The nucleophilicities and competitive reactivities of alkoxides and phenoxides. *Canadian Journal of Chemistry*. **1979**, *57* (20), 2747-2754.
47. Brauman, J. I.; Blair, L. K., Gas-phase acidities of alcohols. *Journal of the American Chemical Society*. **1970**, *92* (20), 5986-92.
48. Irwin, J. G.; Williams, M. L., Acid rain: Chemistry and transport. *Environmental Pollution*. **1988**, *50* (1-2), 29-59.
49. Gibson, E. R.; Hudson, P. K.; Grassian, V. H., Physicochemical Properties of Nitrate Aerosols: Implications for the Atmosphere. *The Journal of Physical Chemistry A* **2006**, *110* (42), 11785-11799.
50. Kido Soule, M. C.; Blower, P. G.; Richmond, G. L., Nonlinear Vibrational Spectroscopic Studies of the Adsorption and Speciation of Nitric Acid at the Vapor/Acid Solution Interface. *The Journal of Physical Chemistry A* **2007**, *111* (17), 3349-3357.
51. Gilman, J. B.; Tervahattu, H.; Vaida, V., Interfacial properties of mixed films of long-chain organics at the air-water interface. *Atmos. Environ.* **2006**, *40* (34), 6606-6614.
52. Creighton, T., *Proteins: Structures and Molecular Properties*. 2nd ed.; W. H. Freeman and Company: New York, 1993.
53. Rontu, N.; Vaida, V., Miscibility of Perfluorododecanoic Acid with Organic Acids at the Air-Water Interface. *The Journal of Physical Chemistry C* **2007**, *111* (27), 9975-9980.
54. Dai, Z.; Ju, H., Effect of chain length on the surface properties of [small omega]-carboxy alkanethiol self-assembled monolayers. *PHYSICAL CHEMISTRY CHEMICAL PHYSICS* **2001**, *3* (17), 3769-3773.
55. Kanicky, J. R.; Shah, D. O., Effect of Degree, Type, and Position of Unsaturation on the pKa of Long-Chain Fatty Acids. *Journal of Colloid and Interface Science*. **2002**, *256* (1), 201-207.
56. Delgado, J. M.; Berná, A.; Orts, J. M.; Rodes, A.; Feliu, J. M., In Situ Infrared Study of the Adsorption and Surface Acid-Base Properties of the Anions of Dicarboxylic Acids at Gold Single Crystal and Thin-Film Electrodes. *The Journal of Physical Chemistry C* **2007**, *111* (27), 9943-9952.
57. Mudunkotuwa, I. A.; Grassian, V. H., Citric Acid Adsorption on TiO<sub>2</sub> Nanoparticles in Aqueous Suspensions at Acidic and Circumneutral pH: Surface Coverage, Surface Speciation, and Its Impact on Nanoparticle-Nanoparticle Interactions. *Journal of the American Chemical Society*. **2010**, *132* (42), 14986-14994.
58. Whiddon, C. R.; Bunton, C. A.; Söderman, O., Titration of Fatty Acids in Sugar-Derived (APG) Surfactants: A <sup>13</sup>C NMR Study of the Effect of Headgroup Size, Chain Length, and Concentration on Fatty Acid pKa at a Nonionic Micellar Interface. *The Journal of Physical Chemistry B* **2003**, *107* (4), 1001-1005.
59. Burris, S. C.; Zhou, Y.; Maupin, W. A.; Ebelhar, A. J.; Daugherty, M. W., The Effect of Surface Preparation on Apparent Surface pKa's of ω-Mercaptocarboxylic Acid Self-Assembled Monolayers on Polycrystalline Gold. *The Journal of Physical Chemistry C* **2008**, *112* (17), 6811-6815.

60. Wang, D.; Nap, R. J.; Lagzi, I.; Kowalczyk, B.; Han, S.; Grzybowski, B. A.; Szeleifer, I., How and Why Nanoparticle's Curvature Regulates the Apparent pKa of the Coating Ligands. *Journal of the American Chemical Society*. **2011**, *133* (7), 2192-2197.
61. Schnitzer, C.; Baldelli, S.; Campbell, D. J.; Shultz, M. J., Sum Frequency Generation of O–H Vibrations on the Surface of H<sub>2</sub>O/HNO<sub>3</sub> Solutions and Liquid HNO<sub>3</sub>. *The Journal of Physical Chemistry A* **1999**, *103* (32), 6383-6386.
62. Allen, H. C.; Raymond, E. A.; Richmond, G. L., Surface Structural Studies of Methanesulfonic Acid at Air /Aqueous Solution Interfaces Using Vibrational Sum Frequency Spectroscopy†. *The Journal of Physical Chemistry A* **2001**, *105* (9), 1649-1655.
63. Tarbuck, T. L.; Ota, S. T.; Richmond, G. L., Spectroscopic Studies of Solvated Hydrogen and Hydroxide Ions at Aqueous Surfaces. *Journal of the American Chemical Society*. **2006**, *128* (45), 14519-14527.
64. Mucha, M.; Frigato, T.; Levering, L. M.; Allen, H. C.; Tobias, D. J.; Dang, L. X.; Jungwirth, P., Unified Molecular Picture of the Surfaces of Aqueous Acid, Base, and Salt Solutions. *The Journal of Physical Chemistry B* **2005**, *109* (16), 7617-7623.
65. Tang, C. Y.; Allen, H. C., Ionic Binding of Na<sup>+</sup> versus K<sup>+</sup> to the Carboxylic Acid Headgroup of Palmitic Acid Monolayers Studied by Vibrational Sum Frequency Generation Spectroscopy†. *The Journal of Physical Chemistry A* **2009**, *113* (26), 7383-7393.
66. Valley, N. A.; Blower, P. G.; Wood, S. R.; Plath, K. L.; McWilliams, L. E.; Richmond, G. L., Doubling Down: Delving into the Details of Diacid Adsorption at Aqueous Surfaces. *The Journal of Physical Chemistry A* **2014**, *118* (26), 4778-4789.
67. Rao, Y.; Li, X.; Lei, X. G.; Jockusch, S.; George, M. W.; Turro, N. J.; Eisenthal, K. B., Observations of Interfacial Population and Organization of Surfactants with Sum Frequency Generation and Surface Tension. *The Journal of Physical Chemistry C* **2011**, *115* (24), 12064-12067.
68. Ma, G.; Allen, H. C., New Insights into Lung Surfactant Monolayers Using Vibrational Sum Frequency Generation Spectroscopy. *Photochemistry and Photobiology*. **2006**, *82* (6), 1517-1529.
69. Rao, Y.; Subir, M.; McArthur, E. A.; Turro, N. J.; Eisenthal, K. B., Organic ions at the air/water interface. *Chemical Physics Letters*. **2009**, *477* (4–6), 241-244.
70. Tang, C. Y.; Huang, Z.; Allen, H. C., Binding of Mg<sup>2+</sup> and Ca<sup>2+</sup> to Palmitic Acid and Deprotonation of the COOH Headgroup Studied by Vibrational Sum Frequency Generation Spectroscopy. *The Journal of Physical Chemistry B* **2010**, *114* (51), 17068-17076.
71. Kanicky, J. R.; Poniatowski, A. F.; Mehta, N. R.; Shah, D. O., Cooperativity among Molecules at Interfaces in Relation to Various Technological Processes: Effect of Chain Length on the pKa of Fatty Acid Salt Solutions. *Langmuir* **2000**, *16* (1), 172-177.
72. Wellen, B. A.; Lach, E. A.; Allen, H. C., Surface pKa of octanoic, nonanoic, and decanoic fatty acids at the air-water interface: applications to atmospheric aerosol chemistry. *PHYSICAL CHEMISTRY CHEMICAL PHYSICS* **2017**.
73. Glazer, J.; Dogan, M. Z., Ionization of protein monolayers and related substances. *Transactions of the Faraday Society* **1953**, *49* (0), 448-455.

74. Cistola, D. P.; Hamilton, J. A.; Jackson, D.; Small, D. M., Ionization and phase behavior of fatty acids in water: application of the Gibbs phase rule. *Biochemistry* **1988**, 27 (6), 1881-1888.
75. Kanicky, J. R.; Shah, D. O., Effect of Premicellar Aggregation on the pKa of Fatty Acid Soap Solutions. *Langmuir* **2003**, 19 (6), 2034-2038.
76. Griffith, E. C.; Vaida, V., Ionization state of L-Phenylalanine at the Air-Water Interface. *Journal of the American Chemical Society*. **2013**, 135 (2), 710-716.
77. Meinders, M. B.; van den Bosch, G. G.; de Jongh, H. H., Adsorption properties of proteins at and near the air/water interface from IRRAS spectra of protein solutions. *European biophysics journal : EBJ* **2001**, 30 (4), 256-67.
78. Vacha, R.; Buch, V.; Milet, A.; Devlin, J. P.; Jungwirth, P., Autoionization at the surface of neat water: is the top layer pH neutral, basic, or acidic? *PHYSICAL CHEMISTRY CHEMICAL PHYSICS* **2007**, 9 (34), 4736-4747.
79. Langmuir, I., THE CONSTITUTION AND FUNDAMENTAL PROPERTIES OF SOLIDS AND LIQUIDS. II. LIQUIDS.1. *Journal of the American Chemical Society*. **1917**, 39 (9), 1848-1906.
80. Fromherz, P., Instrumentation for handling monomolecular films at an air–water interface. *Review of Scientific Instruments*. **1975**, 46 (10), 1380-1385.
81. Buch, V.; Milet, A.; Vácha, R.; Jungwirth, P.; Devlin, J. P., Water surface is acidic. *Proceedings of the National Academy of Sciences* **2007**, 104 (18), 7342-7347.
82. Markovich, T.; Andelman, D.; Podgornik, R., Surface Tension of Acid Solutions: Fluctuations beyond the Nonlinear Poisson-Boltzmann Theory. *Langmuir* **2016**.
83. Guggenheim, E. A., The Theoretical Basis of Raoult's Law. *Transactions of the Faraday Society* **1937**, 33, 151-156.
84. Scatchard, G., Equilibrium in non-electrolyte mixtures. *Chem Rev* **1949**, 44, 7-35.
85. Elliott, J. R.; Lira, C. T., *Introductory Chemical Engineering Thermodynamics*. 2nd ed.; Prentice Hall: 2012.
86. Redlich, O.; Kister, A. T., Algebraic Representation of Thermodynamic Properties and the Classification of Solutions. *Industrial and Engineering Chemistry* **1948**, 40 (2), 345-348.
87. Stanley, H. E., Scaling, universality, and renormalization: Three pillars of modern critical phenomena. *Reviews of Modern Physics* **1999**, 71 (2), S358-S366.
88. Andelman, D.; Brochard, F.; Joanny, J. F., Phase-Transitions in Langmuir Monolayers of Polar-Molecules. *Journal of Chemical Physics* **1987**, 86 (6), 3673-3681.
89. Andelman, D.; Brochard, F.; de Gennes, P.-G.; Joanny, J.-F., *Transitions de monocouches &#224; mol&#233;cules polaires*. Gauthier-Villars: Paris, FRANCE, 1985; Vol. 301.
90. Andelman, D.; Brochard, F.; Joanny, J. F., Modulated Structures and Competing Interactions in Amphiphilic Monolayers. *Proceedings of the National Academy of Sciences of the United States of America* **1987**, 84 (14), 4717-4718.
91. Beattie, J. K.; Djerdjev, A. M.; Gray-Weale, A.; Kallay, N.; Lützenkirchen, J.; Preočanin, T.; Selmani, A., pH and the surface tension of water. *Journal of Colloid and Interface Science*. **2014**, 422, 54-57.

92. Nagata, Y.; Hsieh, C.-S.; Hasegawa, T.; Voll, J.; Backus, E. H. G.; Bonn, M., Water Bending Mode at the Water–Vapor Interface Probed by Sum-Frequency Generation Spectroscopy: A Combined Molecular Dynamics Simulation and Experimental Study. *The Journal of Physical Chemistry Letters* **2013**, *4* (11), 1872-1877.
93. Vinaykin, M.; Benderskii, A. V., Vibrational Sum-Frequency Spectrum of the Water Bend at the Air/Water Interface. *The Journal of Physical Chemistry Letters* **2012**, *3* (22), 3348-3352.
94. Varsanyi, G., *Vibrational Spectra of Benzene Derivatives*. Academic Press: New York and London, 1969.
95. Rao, Y.; Comstock, M.; Eienthal, K. B., Absolute Orientation of Molecules at Interfaces. *The Journal of Physical Chemistry B* **2006**, *110* (4), 1727-1732.
96. Moad, A. J.; Simpson, G. J., A Unified Treatment of Selection Rules and Symmetry Relations for Sum-Frequency and Second Harmonic Spectroscopies. *The Journal of Physical Chemistry B* **2004**, *108* (11), 3548-3562.
97. Roke, S.; Bonn, M.; Petukhov, A. V., Nonlinear optical scattering: The concept of effective susceptibility. *Physical Review B* **2004**, *70* (11), 115106.
98. Gan, W.; Wu, B.-h.; Zhang, Z.; Guo, Y.; Wang, H.-f., Vibrational Spectra and Molecular Orientation with Experimental Configuration Analysis in Surface Sum Frequency Generation (SFG). *The Journal of Physical Chemistry C* **2007**, *111* (25), 8716-8725.
99. Ben-Amotz, D.; Widom, B., Nonideal gas solvation thermodynamics. *The Journal of Chemical Physics* **2007**, *126* (10), 104502.
100. Goldstein, R. E., Phenomenological theory of multiply reentrant solubility. *The Journal of Chemical Physics* **1985**, *83* (3), 1246-1254.
101. Ben-Amotz, D.; Widom, B., Nonideal gas solvation thermodynamics. *The Journal of Chemical Physics* **2007**, *126* (10).
102. Zhao, X.; Subrahmanyam, S.; Eienthal, K. B., Orientational fluctuations and phase transitions of long chain molecules at the air/water interface. *Physical Review Letters* **1991**, *67* (15), 2025-2028.
103. Zhao, X.; Eienthal, K. B., Monolayer orientational fluctuations and a new phase transition at the air water interface detected by second harmonic generation. *Journal of Chemical Physics* **1995**, *102* (14), 5818-5826.
104. Chen, J.; Liu, J.; Tevis, I. D.; Andino, R. S.; Miller, C. M.; Ziegler, L. D.; Chen, X.; Thuo, M. M., Spectroscopic evidence for the origin of odd-even effects in self-assembled monolayers and effects of substrate roughness. *PHYSICAL CHEMISTRY CHEMICAL PHYSICS* **2017**, *19* (10), 6989-6995.
105. Wang, H.-F.; Velarde, L.; Gan, W.; Fu, L., Quantitative Sum-Frequency Generation Vibrational Spectroscopy of Molecular Surfaces and Interfaces: Lineshape, Polarization, and Orientation. *Annual Review of Physical Chemistry*. **2015**, *66* (1), 189-216.
106. Manciu, M.; Ruckenstein, E., On the Interactions of Ions with the Air/Water Interface. *Langmuir* **2005**, *21* (24), 11312-11319.
107. Boström, M.; Kunz, W.; Ninham, B. W., Hofmeister Effects in Surface Tension of Aqueous Electrolyte Solution. *Langmuir* **2005**, *21* (6), 2619-2623.

108. Andersson, M. P.; Olsson, M. H. M.; Stipp, S. L. S., Predicting the pKa and Stability of Organic Acids and Bases at an Oil–Water Interface. *Langmuir* **2014**, *30* (22), 6437-6445.
109. Konek, C. T.; Musorrafiti, M. J.; Al-Abadleh, H. A.; Bertin, P. A.; Nguyen, S. T.; Geiger, F. M., Interfacial Acidities, Charge Densities, Potentials, and Energies of Carboxylic Acid-Functionalized Silica/Water Interfaces Determined by Second Harmonic Generation. *Journal of the American Chemical Society*. **2004**, *126* (38), 11754-11755.
110. Gershevit, O.; Sukenik, C. N., In Situ FTIR-ATR Analysis and Titration of Carboxylic Acid-Terminated SAMs. *Journal of the American Chemical Society*. **2004**, *126* (2), 482-483.
111. Marty, J. C.; Saliot, A.; Buat-Menard, P.; Chesselet, R.; Hunter, K. A., Relationship Between the Lipid Compositions of Marine Aerosols, the Sea Surface Microlayer, and Subsurface Water. *Journal of Geophysical Research* **1979**, *84* (C9), 5707-5716.
112. K., S. J.; B., G. R., Particle size distribution of lipids in aerosols off the coast of Peru. *Journal of Geophysical Research: Atmospheres* **1985**, *90* (D5), 7889-7898.
113. Donaldson, D. J.; Vaida, V., The Influence of Organic Films at the Air–Aqueous Boundary on Atmospheric Processes. *Chemical Reviews*. **2006**, *106* (4), 1445-1461.
114. Shen, Y. R., Basic Theory of Surface Sum-Frequency Generation. *The Journal of Physical Chemistry C* **2012**, *116* (29), 15505-15509.
115. Strazdaite, S.; Meister, K.; Bakker, H. J., Reduced Acid Dissociation of Amino-Acids at the Surface of Water. *Journal of the American Chemical Society*. **2017**, *139* (10), 3716-3720.
116. McLean, D. S.; Vercoe, D.; Stack, K. R.; Richardson, D., The colloidal pKa of lipophilic extractives commonly found in *Pinus radiata*. *Appita J.* **2005**, *58*, 362-366.
117. Dickhaus, B. N.; Priefer, R., Determination of polyelectrolyte pKa values using surface-to-air tension measurements. *Colloids and Surfaces A: Physicochemical and Engineering Aspects* **2016**, *488*, 15-19.
118. Wellen, B. A.; Lach, E. A.; Allen, H. C., Surface pKa of octanoic, nonanoic, and decanoic fatty acids at the air-water interface: applications to atmospheric aerosol chemistry. *PHYSICAL CHEMISTRY CHEMICAL PHYSICS* **2017**, *19* (39), 26551-26558.
119. Prisle, N. L.; Ottoson, N.; Öhrwall, G.; Söderström, J.; Dal Maso, M.; Björneholm, O., Surface/bulk partitioning and acid/base speciation of aqueous decanoate: direct observations and atmospheric implications. *Atmospheric Chemistry and Physics*. **2012**, *12* (24), 12227-12242.
120. Cratin, P. D., Mathematical Modeling of Some pH-Dependent Surface and Interfacial Properties of Stearic Acid. *J. Dispersion Sci. Technol.* **1993**, *14* (5), 559-602.
121. *CRC Handbook of Chemistry and Physics*. 89th ed.; CRC Taylor and Francis Group: Boca Raton, FL, 2008.
122. Drummond, C. J.; Grieser, F.; Healy, T. W., Acid–base equilibria in aqueous micellar solutions. Part 1.—‘Simple’ weak acids and bases. *Journal of the Chemical Society, Faraday Transactions 1: Physical Chemistry in Condensed Phases* **1989**, *85* (3), 521-535.

123. Hofmeister, F., Zur Lehre von der Wirkung der Salze. *Archiv für experimentelle Pathologie und Pharmakologie* **1888**, 24 (4), 247-260.
124. Collins, K. D.; Washabaugh, M. W., The Hofmeister effect and the behaviour of water at interfaces. *Quarterly Reviews of Biophysics* **1985**, 18 (4), 323-422.
125. Parsegian, V. A., Hopes for Hofmeister. *Nature* **1995**, 378, 335.
126. Kunz, W.; Henle, J.; Ninham, B. W., 'Zur Lehre von der Wirkung der Salze' (about the science of the effect of salts): Franz Hofmeister's historical papers. *Current Opinion in Colloid & Interface Science* **2004**, 9 (1), 19-37.
127. Omta, A. W.; Kropman, M. F.; Woutersen, S.; Bakker, H. J., Negligible Effect of Ions on the Hydrogen-Bond Structure in Liquid Water. *Science* **2003**, 301 (5631), 347-349.
128. Funkner, S.; Niehues, G.; Schmidt, D. A.; Heyden, M.; Schwaab, G.; Callahan, K. M.; Tobias, D. J.; Havenith, M., Watching the Low-Frequency Motions in Aqueous Salt Solutions: The Terahertz Vibrational Signatures of Hydrated Ions. *Journal of the American Chemical Society*. **2012**, 134 (2), 1030-1035.
129. Stirnemann, G.; Wernersson, E.; Jungwirth, P.; Laage, D., Mechanisms of Acceleration and Retardation of Water Dynamics by Ions. *Journal of the American Chemical Society*. **2013**, 135 (32), 11824-11831.
130. Chen, X.; Yang, T.; Kataoka, S.; Cremer, P. S., Specific Ion Effects on Interfacial Water Structure near Macromolecules. *Journal of the American Chemical Society*. **2007**, 129 (40), 12272-12279.
131. Heskins, M.; Guillet, J. E., Solution Properties of Poly(N-isopropylacrylamide). *Journal of Macromolecular Science: Part A - Chemistry* **1968**, 2 (8), 1441-1455.
132. Zhang, Y.; Furyk, S.; Bergbreiter, D. E.; Cremer, P. S., Specific Ion Effects on the Water Solubility of Macromolecules: PNIPAM and the Hofmeister Series. *Journal of the American Chemical Society*. **2005**, 127 (41), 14505-14510.
133. Schild, H. G., Poly(N-isopropylacrylamide): experiment, theory and application. *Progress in Polymer Science*. **1992**, 17 (2), 163-249.
134. Lo Nostro, P.; Ninham, B. W., Hofmeister Phenomena: An Update on Ion Specificity in Biology. *Chemical Reviews*. **2012**, 112 (4), 2286-2322.
135. Maeda, Y.; Higuchi, T.; Ikeda, I., Change in Hydration State during the Coil-Globule Transition of Aqueous Solutions of Poly(N-isopropylacrylamide) as Evidenced by FTIR Spectroscopy. *Langmuir* **2000**, 16 (19), 7503-7509.
136. Maeda, Y.; Higuchi, T.; Ikeda, I., FTIR Spectroscopic and Calorimetric Studies of the Phase Transitions of N-Isopropylacrylamide Copolymers in Water. *Langmuir* **2001**, 17 (24), 7535-7539.
137. Tu, C.-W.; Kuo, S.-W., Using FTIR spectroscopy to study the phase transitions of poly(N-isopropylacrylamide) in tetrahydrofuran-d 8/D2O. *Journal of Polymer Research* **2014**, 21 (6), 476.
138. Scatena, L. F.; Brown, M. G.; Richmond, G. L., Water at Hydrophobic Surfaces: Weak Hydrogen Bonding and Strong Orientation Effects. *Science* **2001**, 292 (5518), 908-912.
139. Fan, Y.; Chen, X.; Yang, L.; Cremer, P. S.; Gao, Y. Q., On the structure of water at the aqueous/air interface. *The Journal of Physical Chemistry B* **2009**, 113 (34), 11672-9.

140. Du, Q.; Superfine, R.; Freysz, E.; Shen, Y. R., Vibrational spectroscopy of water at the vapor/water interface. *Physical Review Letters*. **1993**, *70* (15), 2313-2316.
141. Verbiest, T.; Samyn, C.; Boutton, C.; Houbrechts, S.; Kauranen, M.; Persoons, A., Second-order nonlinear optical properties of a chromophore-functionalized polypeptide. *Advanced Materials*. **1996**, *8* (9), 756-759.
142. Verbiest, T.; Elshocht, S. V.; Kauranen, M.; Hellemans, L.; Snauwaert, J.; Nuckolls, C.; Katz, T. J.; Persoons, A., Strong Enhancement of Nonlinear Optical Properties Through Supramolecular Chirality. *Science* **1998**, *282* (5390), 913-915.
143. Frank, A.; Gabriele, N.; Börje, S., Odd–Even Chain Length-Dependent Order in pH-Switchable Self-Assembled Layers. *Chemistry – A European Journal* **2004**, *10* (13), 3232-3240.
144. Azzam, W.; Cyganik, P.; Witte, G.; Buck, M.; Wöll, C., Pronounced Odd–Even Changes in the Molecular Arrangement and Packing Density of Biphenyl-Based Thiol SAMs: A Combined STM and LEED Study. *Langmuir* **2003**, *19* (20), 8262-8270.
145. Blumstein, A.; Blumstein, R., *Recent Advances in Liquid Crystalline Polymers*. Springer: 1985.
146. Cacelli, I.; Gaetani, L. D.; Prampolini, G.; Tani, A., How the Odd-Even Effects on the Inter-Molecular Potentials Propagate to the Order Parameter in the 4-Cyano-4' n-Alkylbiphenyl Series. *Molecular Crystals and Liquid Crystals* **2007**, *465* (1), 175-186.
147. Chen, J.; Wang, Z.; Oyola-Reynoso, S.; Gathiaka, S. M.; Thuo, M., Limits to the Effect of Substrate Roughness or Smoothness on the Odd–Even Effect in Wetting Properties of n-Alkanethiolate Monolayers. *Langmuir* **2015**, *31* (25), 7047-7054.
148. Newcomb, L. B.; Tevis, I. D.; Atkinson, M. B. J.; Gathiaka, S. M.; Luna, R. E.; Thuo, M., Odd–Even Effect in the Hydrophobicity of n-Alkanethiolate Self-Assembled Monolayers Depends upon the Roughness of the Substrate and the Orientation of the Terminal Moiety. *Langmuir* **2014**, *30* (40), 11985-11992.
149. Ramin, L.; Jabbarzadeh, A., Odd–Even Effects on the Structure, Stability, and Phase Transition of Alkanethiol Self-Assembled Monolayers. *Langmuir* **2011**, *27* (16), 9748-9759.
150. Wang, Z.; Chen, J.; Oyola-Reynoso, S.; Thuo, M., The Porter-Whitesides Discrepancy: Revisiting Odd-Even Effects in Wetting Properties of n-Alkanethiolate SAMs. *Coatings* **2015**, *5* (4), 1034.
151. Thuo, M. M.; Reus, W. F.; Nijhuis, C. A.; Barber, J. R.; Kim, C.; Schulz, M. D.; Whitesides, G. M., Odd–Even Effects in Charge Transport across Self-Assembled Monolayers. *Journal of the American Chemical Society*. **2011**, *133* (9), 2962-2975.
152. Jiang, L.; Sangeeth, C. S. S.; Nijhuis, C. A., The Origin of the Odd–Even Effect in the Tunneling Rates across EGaIn Junctions with Self-Assembled Monolayers (SAMs) of n-Alkanethiolates. *Journal of the American Chemical Society*. **2015**, *137* (33), 10659-10667.
153. Rong, H.-T.; Frey, S.; Yang, Y.-J.; Zharnikov, M.; Buck, M.; Wühn, M.; Wöll, C.; Helmchen, G., On the Importance of the Headgroup Substrate Bond in Thiol Monolayers: A Study of Biphenyl-Based Thiols on Gold and Silver. *Langmuir* **2001**, *17* (5), 1582-1593.

154. Alloway, D. M.; Hofmann, M.; Smith, D. L.; Gruhn, N. E.; Graham, A. L.; Colorado, R.; Wysocki, V. H.; Lee, T. R.; Lee, P. A.; Armstrong, N. R., Interface Dipoles Arising from Self-Assembled Monolayers on Gold: UV-Photoemission Studies of Alkanethiols and Partially Fluorinated Alkanethiols. *The Journal of Physical Chemistry B* **2003**, *107* (42), 11690-11699.
155. Heister, K.; Rong, H. T.; Buck, M.; Zharnikov, M.; Grunze, M.; Johansson, L. S. O., Odd-Even Effects at the S-Metal Interface and in the Aromatic Matrix of Biphenyl-Substituted Alkanethiol Self-Assembled Monolayers. *The Journal of Physical Chemistry B* **2001**, *105* (29), 6888-6894.
156. Zharnikov, M.; Frey, S.; Rong, H.; Yang, Y. J.; Heister, K.; Buck, M.; Grunze, M., The effect of sulfur-metal bonding on the structure of self-assembled monolayers. *PHYSICAL CHEMISTRY CHEMICAL PHYSICS* **2000**, *2* (15), 3359-3362.
157. Nerngchamng, N.; Yuan, L.; Qi, D.-C.; Li, J.; Thompson, D.; Nijhuis, C. A., The role of van der Waals forces in the performance of molecular diodes. *Nature Nanotechnology* **2013**, *8*, 113.
158. Cyganik, P.; Buck, M.; Azzam, W.; Wöll, C., Self-Assembled Monolayers of  $\omega$ -Biphenylalkanethiols on Au(111): Influence of Spacer Chain on Molecular Packing. *The Journal of Physical Chemistry B* **2004**, *108* (16), 4989-4996.
159. Cyganik, P.; Szelagowska-Kunstman, K.; Terfort, A.; Zharnikov, M., Odd-Even Effect in Molecular Packing of Biphenyl-Substituted Alkaneselenolate Self-Assembled Monolayers on Au(111): Scanning Tunneling Microscopy Study. *The Journal of Physical Chemistry C* **2008**, *112* (39), 15466-15473.
160. Dendzik, M.; Terfort, A.; Cyganik, P., Odd-Even Effect in the Polymorphism of Self-Assembled Monolayers of Biphenyl-Substituted Alkaneselenolates on Au(111). *The Journal of Physical Chemistry C* **2012**, *116* (36), 19535-19542.
161. Liu, J.; Schüpbach, B.; Bashir, A.; Shekhah, O.; Nefedov, A.; Kind, M.; Terfort, A.; Wöll, C., Structural characterization of self-assembled monolayers of pyridine-terminated thiolates on gold. *PHYSICAL CHEMISTRY CHEMICAL PHYSICS* **2010**, *12* (17), 4459-4472.
162. Tao, F.; Bernasek, S. L., Understanding Odd-Even Effects in Organic Self-Assembled Monolayers. *Chemical Reviews*. **2007**, *107* (5), 1408-1453.
163. Angelico, V. J.; Mitchell, S. A.; Wysocki, V. H., Low-Energy Ion-Surface Reactions of Pyrazine with Two Classes of Self-Assembled Monolayers: Influence of Alkyl Chain Orientation. *Analytical Chemistry*. **2000**, *72* (11), 2603-2608.
164. Rulkens, R.; Lough, A. J.; Manners, I.; Lovelace, S. R.; Grant, C.; Geiger, W. E., Linear Oligo(ferrocenyldimethylsilanes) with between Two and Nine Ferrocene Units: Electrochemical and Structural Models for Poly(ferrocenylsilane) High Polymers. *Journal of the American Chemical Society*. **1996**, *118* (50), 12683-12695.
165. Imahori, H.; Norieda, H.; Nishimura, Y.; Yamazaki, I.; Higuchi, K.; Kato, N.; Motohiro, T.; Yamada, H.; Tamaki, K.; Arimura, M.; Sakata, Y., Chain Length Effect on the Structure and Photoelectrochemical Properties of Self-Assembled Monolayers of Porphyrins on Gold Electrodes. *The Journal of Physical Chemistry B* **2000**, *104* (6), 1253-1260.

166. Cimatu, K.; Moore, H. J.; Lee, T. R.; Baldelli, S., Sum Frequency Generation Imaging of Microcontact-Printed Monolayers Derived from Aliphatic Dithiocarboxylic Acids: Contrast Based on Terminal-Group Orientation. *The Journal of Physical Chemistry C* **2007**, *111* (32), 11751-11755.
167. Nishi, N.; Hobara, D.; Yamamoto, M.; Kakiuchi, T., Chain-length-dependent change in the structure of self-assembled monolayers of n-alkanethiols on Au(111) probed by broad-bandwidth sum frequency generation spectroscopy. *The Journal of Chemical Physics* **2003**, *118* (4), 1904-1911.
168. Shen, Y. R., Surface properties probed by second-harmonic and sum-frequency generation. *Nature* **1989**, *337*, 519.
169. Bain, C. D., Sum-frequency vibrational spectroscopy of the solid/liquid interface. *Journal of the Chemical Society, Faraday Transactions*. **1995**, *91* (9), 1281-1296.
170. Guo, Z.; Zheng, W.; Hamoudi, H.; Dablemont, C.; Esaulov, V.; Bourguignon, B., *On the chain length dependence of CH<sub>3</sub> vibrational mode relative intensities in sum frequency generation spectra of self assembled alkanethiols*. 2008; Vol. 602, p 3551-3559.
171. Nurbawono, A.; Liu, S.; Nijhuis, C. A.; Zhang, C., Odd–Even Effects in Charge Transport through Self-Assembled Monolayer of Alkanethiolates. *The Journal of Physical Chemistry C* **2015**, *119* (10), 5657-5662.
172. Baghbanzadeh, M.; Simeone, F. C.; Bowers, C. M.; Liao, K.-C.; Thuo, M.; Baghbanzadeh, M.; Miller, M. S.; Carmichael, T. B.; Whitesides, G. M., Odd–Even Effects in Charge Transport across n-Alkanethiolate-Based SAMs. *Journal of the American Chemical Society*. **2014**, *136* (48), 16919-16925.
173. Jiang, L.; Sangeeth, C. S. S.; Yuan, L.; Thompson, D.; Nijhuis, C. A., One-Nanometer Thin Monolayers Remove the Deleterious Effect of Substrate Defects in Molecular Tunnel Junctions. *Nano Letters*. **2015**, *15* (10), 6643-6649.
174. Jiang, L.; Yuan, L.; Cao, L.; Nijhuis, C. A., Controlling Leakage Currents: The Role of the Binding Group and Purity of the Precursors for Self-Assembled Monolayers in the Performance of Molecular Diodes. *Journal of the American Chemical Society*. **2014**, *136* (5), 1982-1991.
175. Li, Y.; Li, J.; Bo, Z.; A., N. C., Dependency of the Tunneling Decay Coefficient in Molecular Tunneling Junctions on the Topography of the Bottom Electrodes. *Angewandte Chemie International Edition* **2014**, *53* (13), 3377-3381.
176. Yuan, L.; Jiang, L.; Thompson, D.; Nijhuis, C. A., On the Remarkable Role of Surface Topography of the Bottom Electrodes in Blocking Leakage Currents in Molecular Diodes. *Journal of the American Chemical Society*. **2014**, *136* (18), 6554-6557.
177. Wang, Z.; Chen, J.; Oyola-Reynoso, S.; Thuo, M., Empirical Evidence for Roughness-Dependent Limit in Observation of Odd–Even Effect in Wetting Properties of Polar Liquids on n-Alkanethiolate Self-Assembled Monolayers. *Langmuir* **2016**, *32* (32), 8230-8237.
178. Wang, Z.; Chen, J.; Gathiaka, S. M.; Oyola-Reynoso, S.; Thuo, M., Effect of Substrate Morphology on the Odd–Even Effect in Hydrophobicity of Self-Assembled Monolayers. *Langmuir* **2016**, *32* (40), 10358-10367.

179. Hirose, C.; Akamatsu, N.; Domen, K., Formulas for the analysis of surface sum - frequency generation spectrum by CH stretching modes of methyl and methylene groups. *The Journal of Chemical Physics* **1992**, *96* (2), 997-1004.
180. Mukamel, S., *Principles of nonlinear optical spectroscopy*. Oxford University Press on Demand: 1999.
181. Kubo, R.; Toda, M.; Hashitsume, N., *Statistical physics II: nonequilibrium statistical mechanics*. Springer Science & Business Media: 2012.
182. Peng, J.; Castonguay, T. C.; Coker, D. F.; Ziegler, L. D., Ultrafast H<sub>2</sub> and D<sub>2</sub> rotational Raman responses in near critical CO<sub>2</sub>: An experimental and theoretical study of anisotropic solvation dynamics. *The Journal of Chemical Physics* **2009**, *131* (5), 054501.
183. Chen, J.; Chang, B.; Oyola-Reynoso, S.; Wang, Z.; Thuo, M., Quantifying Gauche Defects and Phase Evolution in Self-Assembled Monolayers through Sessile Drops. *ACS Omega* **2017**, *2* (5), 2072-2084.
184. Don, K. G.; Miso, K.; Jin, C. S.; Jae, Y. H., Gradients of Rectification: Tuning Molecular Electronic Devices by the Controlled Use of Different-Sized Diluents in Heterogeneous Self-Assembled Monolayers. *Angewandte Chemie International Edition* **2016**, *55* (35), 10307-10311.
185. Kong, G. D.; Yoon, H. J., Influence of Air-Oxidation on Rectification in Thiol-Based Molecular Monolayers. *Journal of the Electrochemical Society* **2016**, *163* (9), G115-G121.

**CURRICULUM VITAE**

